Moore, G.F., Taira, A., and Klaus, A. (Eds.)
Proceedings of the Ocean Drilling Program, Initial Reports Volume 190

1. Leg 190 Summary[1]

Shipboard Scientific Party[2]

ABSTRACT

Six sites along two transects across the Nankai Trough accretionary prism were successfully drilled during Leg 190, satisfying most of the leg objectives. Two reference sites at the seaward ends of the Muroto Transect (Site 1173) and the Ashizuri Transect (Site 1177) define the stratigraphic framework of the accreting/subducting Shikoku Basin sedimentary section. A thick section of Miocene turbidites and smectite-rich mudstone is present within the subducting section at the Ashizuri site. The turbidites and mudstones are absent in the correlative section at the Muroto site; variations in lithology, mineralogy, and hydrologic properties of the incoming sediments probably contribute to the difference in prism wedge taper between the two transects, while possibly controlling the seismic character of the active plate boundary.

The décollement in both transects is localized along a stratigraphic unit (~5.9–7 Ma) within the lower Shikoku Basin facies. This horizon can be correlated across both transects through its magnetic susceptibility signature.

A broad low-chloride pore-water anomaly in the lower Shikoku Basin unit, first identified at Site 808, progressively decreases in magnitude from prism to basin along the Muroto Transect. It is unclear whether this landward-freshening trend is due to in situ diagenesis, lateral fluid flow, or a combination of the two.

Our ideas of the tectonic evolution of the prism in the Muroto Transect have dramatically changed. Accretion of a Miocene and Pliocene turbidite package forms a large thrust-slice zone (LTSZ). This event is associated with a shift from a transverse sediment transport system that delivered coarse material from the arc to the trench to an axial transport system that delivers sediment down the trench axis from the Izu collision zone to the east. Growth of the prism from the LTSZ to the

[1]Examples of how to reference the whole or part of this volume.
[2]Shipboard Scientific Party addresses.

Ms 190IR-101

toe of the slope (a distance of 40 km) took place rapidly within the past 2 m.y.

INTRODUCTION

Earth scientists have long recognized the complex interplay of deformational, diagenetic, and hydrologic processes in developing mature mountain belts and have sought to understand the controls on and interactions among these fundamental processes. Accretionary prisms represent unique, accessible natural laboratories for exploring initial mountain-building processes. The geometries and structures of accretionary prisms are relatively simple and have been seismically well imaged. Typically, the materials incorporated within prisms are only moderately altered from their original states, so competing active processes can often be isolated, quantified, and reproduced in the laboratory.

The Nankai Trough accretionary prism represents an "end-member" prism, accreting a thick terrigenous sediment section in a setting with structural simplicity and unparalleled resolution by seismic and other geophysical techniques. It therefore represents a superb setting for addressing ODP's Long Range Plan objectives for accretionary prism coring, in situ monitoring, and refinement of mechanical and hydrological models. Our approach for drilling at the Nankai margin includes sites for coring, in situ observation, and long-term monitoring to (1) constrain prism hydrology, mechanical properties, and deformational styles and (2) test existing models for prism evolution.

Leg 190 was the first of a two-leg program concentrating on coring and sampling a transect of sites across the prism within a three-dimensional (3-D) seismic survey (Table **T1**). We refer to this set of sites as the Muroto Transect. An additional site was drilled to the west, which along with previously drilled sites provides a second transect, referred to as the Ashizuri Transect, for comparison of along-strike variations in accretionary processes and inputs. Leg 196, planned for 2001, will use logging-while-drilling technology to collect in situ physical properties data and will also install advanced CORKs (Davis et al., 1992) for long-term in situ monitoring of prism processes including pressure, temperature, fluid geochemistry, and strain.

BACKGROUND

Geological Setting

The Japanese Island arc system is flanked to the east by deep trenches, which are subduction boundaries of the Pacific and Philippine Sea plates (Fig. **F1**). The Nankai Trough is the subducting plate boundary between the Shikoku Basin and the southwest Japan arc (Eurasian plate). The Shikoku Basin is part of the Philippine Sea plate, which is subducting to the northwest under southwest Japan at a rate of 2–4 cm/yr (Karig and Angevine, 1986; Seno, 1977), slightly oblique to the plate margin. Active sediment accretion is presently taking place at the Nankai Trough.

The record of accretion extends landward to Shikoku Island, where older accretionary prism rocks are exposed (Figs. **F2, F3**). The Cretaceous and Tertiary Shimanto Belt is characterized by imbricated thrust

T1. Site summary, p. 87.

F1. Relief map of the Nankai Trough, p. 42.

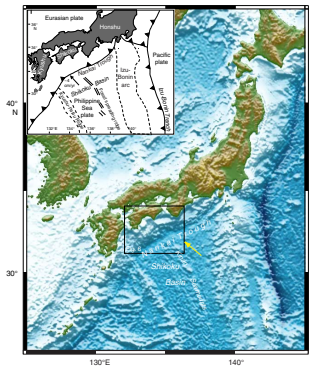

F2. Geologic map of the southwest Japan forearc region, p. 43.

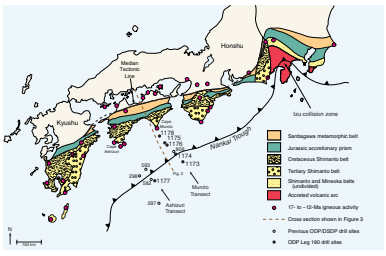

F3. Crustal cross section of the Nankai Trough forearc, p. 44.

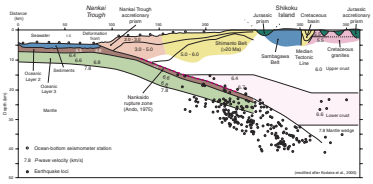

slices of trench turbidites and mélanges composed of ocean-floor basalt, pelagic limestone, radiolarian chert, and hemipelagic shale intermixed with highly sheared scaly shale (Taira et al., 1988). The youngest part of the Shimanto Belt is early Miocene in age. The Shimanto Belt is interpreted as a direct ancient analog of the Nankai accretionary prism (Ohmori et al., 1997).

The subducting oceanic lithosphere of the Shikoku Basin has a history related to the rifting of the proto–Izu-Bonin arc (Taylor, 1992). The rifting started in the Oligocene and culminated in Shikoku Basin seafloor spreading that lasted until ~15 Ma. Three phases of seafloor spreading (Okino et al., 1994) separated the remnant arc, the Kyushu-Palau Ridge, from the active Izu-Bonin arc, creating the Shikoku Basin (Fig. **F4**).

By 15 Ma, most of the Japan Sea ocean floor had formed (Jolivet et al., 1994; Otofuji, 1996). In southwest Japan, widespread igneous activity took place at 17–12 Ma within the forearc, close to the trench (Kano et al., 1991) (Fig. **F2**). This episode, including high-Mg andesite emplacement, is generally interpreted as reflecting injection of hot asthenosphere and initial subduction of the young Shikoku Basin seafloor (Takahashi, 1999). From 15 to 10 Ma, the collision of the Izu-Bonin arc against Honshu was apparently not vigorous, but was persistent enough to maintain sediment supply to the collisional trough (Aoike, 1999).

From 8 to 6 Ma, a fold belt developed on the Japan Sea side of southwest Honshu (Ito and Nagasaki, 1997). Fold axis trends are predominantly northeast-southwest, indicating northwest-southeast compression. Widely distributed volcanic activity, starting at ~8 Ma in southern Kyushu and by 6 Ma in southwest Japan, suggests the establishment of a volcanic front and a deeply penetrating subducting slab (Kamata and Kodama, 1994). In the Izu Collision Zone, the accretion of the Tanzawa massif (part of the volcanic front of the Izu-Bonin arc; Fig. **F4**) seems to have started at ~8 Ma, with the main phase of collision at ~6–5 Ma (Niitsuma, 1989). Subduction of the Shikoku Basin then generated the Nankai Trough, formed a frontal accretionary prism to the southwest Japan forearc (Nankai Trough accretionary prism; Taira et al., 1992; Le Pichon et al., 1987), and shaped forearc basins (Okamura et al., 1987; Sugiyama, 1994).

F4. Paleogeographic reconstruction of the Shimanto Belt and Nankai forearc evolution, p. 45.

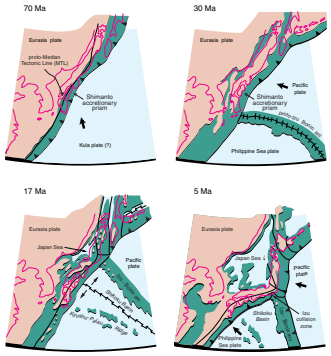

Seismicity, Geodesy, and Thermal Structure

The Nankai Trough has historically generated earthquakes larger than magnitude (M) 8 at intervals of ~180 yr (Ando, 1975, 1991) (Fig. **F5**). The most recent one occurred in 1946 and ruptured off shore of Kii Peninsula and Shikoku. Sites 1175 and 1176 are located close to the seaward limit of this rupture zone. Prior to Global Positioning System (GPS) data, Hyndman et al. (1995, 1997) inferred full coupling of the plate boundary based on leveling data. The nationwide permanent GPS network of the Geographical Survey Institute of Japan revealed that the forearc region of Nankai Trough is moving to the west-northwest at 2–5 cm/yr, confirming a full coupling of the plate boundary during the current interseismic period (Le Pichon et al., 1998; Mazzotti et al., 2000). GPS data were also analyzed to show the nature of interplate coseismic slip of the Nankai seismogenic zone (Sagiya and Thatcher, 1999).

Hyndman et al. (1995, 1997) found a correlation between the observed extent of a seismogenic zone and the thermal regime, especially in the Nankai Trough subduction zone. The updip limit of the seismogenic zone was found to coincide generally with the estimated loca-

F5. Historical recurrence time interval of class M8 earthquakes, p. 46.

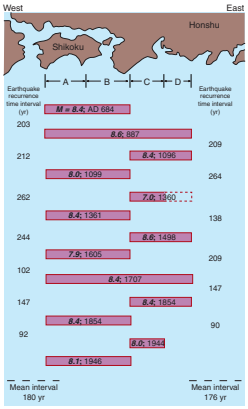

tion of the 150°C isotherm, and the downdip limit coincides with the 350°–450°C isotherm. They proposed that the updip limit coincides with the completion of the smectite-illite transition and the downdip limit coincides with the initiation of ductile deformation of quartz or serpentinization of peridotite mantle.

Geological-Geophysical Database

The geological and geophysical database for the Nankai prism is outstanding. Existing data sets include high-quality industry and academic seismic reflection/refraction data (Aoki et al., 1982; Karig, 1986; Moore et al., 1990, 1991; Stoffa et al., 1992; Park et al., 1999, 2000; Kodaira et al., 2000), complete swath bathymetry, side-scan sonar coverage (Le Pichon et al., 1987; Ashi and Taira, 1992; Taira and Ashi, 1993; Okino and Kato, 1995; Tokuyama et al., 1999), heat flow analyses (Kinoshita and Yamano, 1986; Ashi and Taira, 1993), and three Deep Sea Drilling Project (DSDP)/Ocean Drilling Program (ODP) legs (Legs 31, 87, and 131). Newly acquired 3-D seismic data (*Ewing* 9907/9908) (Bangs et al., 1999; Moore et al., 1999) were used to locate some of the proposed sites (Fig. F6).

The seismic data provide excellent images of the décollement, protothrust zone (PTZ), and various structural domains landward of the frontal thrust that guided our choice of drilling targets, and the well-constrained seismic velocities provide the basis for models of dewatering. The swath bathymetry and side-scan data reveal surficial features that further constrained drill hole locations. One of the prominent topographic features in the vicinity of the Leg 190 sites is an embayment of the trench landward slope. Yamazaki and Okamura (1989) interpreted this embayment as an indentation caused by the collision of seamounts with the prism. Recent seismic reflection work and ocean-bottom seismometer experiments on crustal structure support this interpretation (Park et al., 1999; Kodaira, 2000).

Geological Context of Leg 190 Sites

The well-resolved seismic profiles demonstrate several characteristic structural subdivisions across the accretionary prism. Based on 3-D multichannel seismic data obtained by the *Ewing* 9907/9908 cruise (Fig. F6; also see the "Data Report: Structural Setting of the Leg 190 Muroto Transect" chapter), the accretionary prism along the Muroto Transect can be divided into several tectonic domains from the trench landward (Fig. F7): Nankai Trough axis zone, protothrust zone (PTZ), imbricate thrust zone (ITZ), frontal out-of-sequence thrust (OOST) zone, large thrust-slice (LTS) zone, and landward-dipping reflector (LDR) zone.

Nankai Trough Axis Zone

Results from Legs 87 (Site 582) and 131 (Site 808) indicate that the stratigraphy of the trench is composed of the following lithologic units in descending order: trench turbidites (Holocene–Pleistocene), turbidite–hemipelagite transition (Pleistocene), hemipelagite with tephra layers (lower Pleistocene–upper Pliocene), massive hemipelagite (mid-Pliocene to middle Miocene), acidic volcaniclastics (15 Ma), and pillow basalts (16 Ma) (Fig. F8). The trench turbidite unit, supplied mostly through an axial transport system from a source region situated in the Izu collision zone mountain ranges, shows a mixture of volcanic, sedi-

F6. ODP Leg 190 and previous drill sites in the Nankai Trough, p. 47.

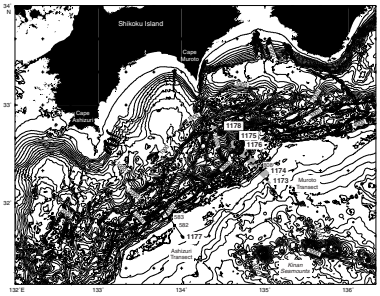

F7. Schematic interpretation of seismic line 141-2D in the Muroto Transect, p. 48.

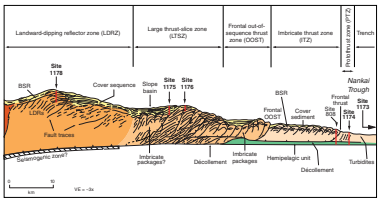

F8. Correlation of facies units, magnetic susceptibility, and major time boundaries, p. 49.

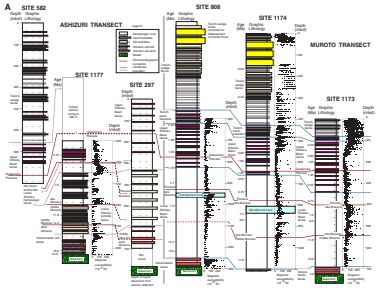

mentary, and metamorphic provenances (Taira and Niitsuma, 1986; Underwood et al., 1993). The lower part of the turbidite unit exhibits a finer-grained outer trench turbidite facies in which paleocurrent directions indicate deflected turbidity currents with a transport direction from the outer trench toward the inner trench (Pickering et al., 1993). The basal acidic volcaniclastic deposit was interpreted as recording extraordinarily large felsic igneous activity of the Outer Zone of southwest Japan during the middle Miocene (Taira, Hill, Firth, et al., 1991).

Site 1173 (ENT-01A) is a reference site drilled to basement seaward of the trench axis to provide baseline physical properties and fluid chemistry measurements (Fig. F9). An additional unit is recognized within the surrounding Shikoku Basin sequence that is not present in the local trench stratigraphy near Site 1173. This unit is stratigraphically below the drilled Shikoku Basin hemipelagic units and is characterized by a well-stratified sequence ~0.7 s thick. This section may correlate with the Miocene turbidite unit identified along the Ashizuri Transect and recovered at Site 1177 within the lower Shikoku Basin facies (hereafter called the Pliocene–Miocene Turbidite Unit) (Figs. F8, F10).

F9. Seismic reflection profile, Muroto Transect, Sites 1173, 1174, and 808, p. 52.

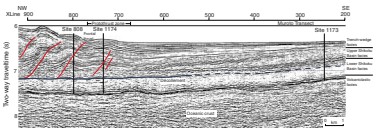

F10. Seismic reflection profile, Ashizuri Transect, Sites 1177, 582, and 583, p. 53.

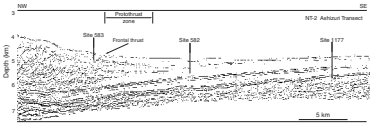

Protothrust Zone

This area represents a zone of incipient deformation and initial development of the décollement within the massive hemipelagic unit. Above the décollement, the sediment thickness increases landward, probably because of tectonic deformation with the development of small faults and ductile strain as envisaged by Morgan and Karig (1995a, 1995b).

Site 1174 (ENT-03A), located in the PTZ, sampled a zone of incipient deformation and possible fluid flow (Fig. F9). This site penetrated into the subducting sediment section all the way to basement. A high priority was to sample pore fluids in detail across the protothrust, décollement, and the underthrust sediments.

Imbricate Thrust Zone

Landward of the PTZ, a zone of well-developed seaward-vergent imbricate thrusts can be recognized. The thrusts are sigmoidal in cross section with a mean dip of ~30° and a typical thrust spacing of 0.5 km. The frontal thrust forms the seaward edge of the ITZ. At Sites 583 and 808 we cored the frontal part of the imbricate thrust zone.

Site 583 is situated on the hanging wall of the frontal thrust. Although drilling failed to penetrate the décollement zone, good quality physical properties measurements were obtained from all of the holes, providing evidence that sediments dewater under tectonic stresses as they are accreted (Bray and Karig, 1988). The pore-water concentration depth profiles from these sites are far from being detailed enough to provide insight into the nature of fluid flow at this segment of the Nankai Trough (Kastner et al., 1993). The significant geochemical findings were that organic-fueled diagenesis is intense and that methane concentrations and the C_1/C_2 ratios abruptly decrease at ~600 mbsf. Interestingly, similar abrupt decreases were observed at the décollement zone at Site 808. Fluid flow from a deep-seated source could explain these observations.

Site 808 (Figs. F8, F9), which penetrated the prism and reached oceanic basement at 1290 mbsf, was particularly successful in terms of physical properties and structural geology measurements because of rel-

atively high core recovery and also because the sediments yielded consistently high-quality paleomagnetic data (Taira et al., 1991, 1992). These data allowed individual core sections and, in some cases, individual structural samples to be oriented relative to the present geographic coordinates. Physical properties generally varied smoothly downhole, except for sharp discontinuities across the frontal thrust and décollement zones. Discrete structures were concentrated in the vicinity of the fault zones as well as in several horizons above the décollement zone.

Pore waters were recovered throughout the section at Site 808, including the frontal thrust, décollement zone, and underthrust package. Depth profiles for chemical concentrations and isotopic ratios (particularly D, O, Sr, and He) do not indicate active fluid flow along the décollement or along the frontal thrust. They may, however, indicate a component of lateral fluid flow (1) below the décollement at the approximate depth of the minimum in Cl concentration (~1100 mbsf) and (2) above the décollement along a horizon marking the lithologic boundary between the volcanic-rich and -poor members of the Shikoku Basin sediments (~820 mbsf). Pore-water freshening may also result from in situ diagenetic reactions, such as thermally driven smectite dehydration. Detailed two dimensional numerical models of fluid flow and solute transport, which incorporate fluid sources from compaction and smectite dehydration, show that measured smectite abundances at Site 808 are insufficient to account for observed freshening, and episodic, focused fluid flow is necessary to match both measured fluid expulsion rates at the seafloor and observed downhole chlorinity values at Site 808 (Saffer and Bekins, 1998). Cores recovered from Site 808 also revealed that fractures within the décollement zone have not been mineralized. This contrasts with observations at Barbados and Peru where the major tectonic structures have been mineralized, implying continuous or episodic fluid flow.

Frontal Out-of-Sequence Thrust Zone

About 20 km landward from the deformation front, the imbricate thrust packages are overthrust by a younger generation fault system. Because this fault system cuts the preexisting sequence of imbricate thrusts, it is called an OOST zone. Important and significant deformation also appears within the underthrust Shikoku Basin hemipelagite. The hemipelagic unit seems to be tectonically thickened, probably as a result of duplexing.

Large Thrust-Slice Zone

Landward of the frontal OOST is a zone characterized by the development of at least four distinctive out-of-sequence thrusts that separate tectonic slices of either previously imbricated packages or relatively coherent sedimentary sequences. The coherent slices are composed of ~0.7-s-thick (maximum) stratified layers that closely resemble the Pliocene–Miocene Turbidite Unit recognized in depressions in the Shikoku Basin. Slope sediment in this zone shows landward tilting suggesting recent active uplift. Bottom-simulating reflectors (BSRs) are weakly and patchily developed in this zone.

Site 1175 (ENT-07A) penetrated the slope sediments that cover the LTSZ. Investigation of the age and lithologic characteristics provided information on the history of accretion and deformation of the prism (Fig. F11).

F11. Seismic reflection profile, Muroto Transect, Sites 1175, 1176, and 1178, p. 54.

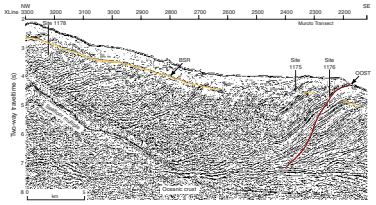

Site 1176 (ENT-06A) was designed to penetrate an OOST, to sample and investigate the lithology, deformation, physical properties, and potential fluid from the seismogenic portion of the accretionary complex (Fig. F11). Difficult drilling conditions, however, led to the site being abandoned above the OOST.

Landward-Dipping Reflectors Zone

Landward-dipping, semicontinuous strong reflectors characterize this zone. Relatively coherent slope sediments cover the sediments exhibiting landward-dipping reflectors (LDRs). This zone appears to be divided into several discrete packages by thrust faults. A BSR is well developed throughout this zone and diminishes abruptly at the boundary between this zone and the LTSZ. Site 1178 penetrated the slope sediments and the sediments characterized by the LDRs (Fig. F11).

Along-Strike Variation

The structural domains described above show variation along the strike of the prism. Along two parallel transects separated by ~100 km, marked differences in prism architecture and structure are evident. The Ashizuri Transect, which includes Leg 87 sites (Figs. F6, F8, F10), displays a well-developed PTZ, containing a series of subparallel dipping discontinuities of unknown origin. These features are not evident within the Muroto Transect PTZ (Fig. F9). Differences in prism taper and seismic character of the décollement along the two transects suggest that the mechanical behavior of the prism differs along strike and that this variability may result from significant differences in mechanical properties and/or pore pressures at the two locations.

Site 1177 is a seaward reference site in the Ashizuri Transect and was designed to establish a baseline of stratigraphic, geochemical, and physical properties for comparison to sites previously drilled during Legs 31 and 87 (Sites 297, 298, 582, and 583).

LEG 190 SCIENTIFIC OBJECTIVES

Spatial Distribution and Temporal Progression of Deformation

Although core recovery at Site 808 was exceptionally good and physical properties and structural observations were unprecedentedly complete, the results yield only a one-dimensional view of the interior of the Nankai prism. Previous drilling provides relatively little constraint on how various stratigraphic parameters, fabrics, structures, physical properties, and geochemistry vary along and across strike or how these variations translate over time. This lack of spatial and temporal control makes it difficult to determine the relations among lithology, deformation, diagenesis, and fluid flow. However, first-order predictions for the distribution of physical properties and structures in two dimensions and the role of fluid pressures in their evolution have been made based on high-quality seismic images, velocities, and the core data from previous drilling. The results of these studies have provided models to test and guided the selection of Leg 190 Nankai Trough drill sites, as well as the associated sampling and analyses. To test this distribution of structures and the role of diagenesis and fluid pressure in its development

and to obtain better constraints on physical properties from which these models are derived, four sites were drilled during Leg 190 across strike of the prism. Together with Site 808, these compose the Muroto Transect. Site 1174 (ENT-03A) represents a less-deformed analog to Site 808 and penetrates the incipient thrust fault in the PTZ as well as the thickened sediments in its footwall and the incipient basal décollement. In contrast, drilling at Sites 1175 (ENT-07A), 1176 (ENT-06A), and 1178 (ENT-09A) penetrated highly deformed and evolved portions of the prism. Site 1177 was drilled to link previous sites to the west into the Ashizuri Transect.

Structural and Hydrologic Evolution of the Décollement Zone

Although well-imaged seismically, the nature and evolution of the décollement zone remains poorly understood. In seismic profiles along the Muroto Transect, the décollement is a reverse polarity reflection that extends well seaward of the deformation front; this has been interpreted to indicate (1) the presence of fluids along a high-porosity fault zone or (2) the probable presence of high pore pressures in the fault zone itself or in underthrust sediments (Moore and Shipley, 1993). At Site 808, the décollement is a 20-m-thick zone of intensely fractured sediment, with evidence for shear-induced brecciation, pore collapse, and local phyllosilicate reorientation (Byrne et al., 1993). Sediments from within the décollement have lower porosities than samples from above and below. A subtle mottled texture in some samples led Maltman et al. (1993) to infer localized zones of elevated fluid pressure within the zone. To test these hypotheses of décollement formation and evolution, we sampled the décollement zone at critical points beneath the Nankai prism (Site 808) and PTZ (Site 1174) to document the spatial variations in structure and fluid pressure

Chemical Gradients and Fluid Flow Paths

The variation of the Cl concentration with depth is of great importance to understanding the hydrogeology and geochemistry of the Nankai Trough Muroto region. Site 808 is characterized by a broad region of Cl concentrations that are lower than seawater (~20% less than seawater) within the Shikoku Basin hemipelagic section (~560–1240 mbsf), with a minimum concentration in the underthrust section at ~1100 mbsf (Kastner et al., 1993). Based on shipboard porosity measurements and XRD estimates of smectite abundance, first-order calculations indicate that ~25% smectite in the incoming section would be required to explain observed pore-water freshening, yet residual smectite abundance is generally <10% at depths corresponding to the low Cl zone (Underwood et al., 1993). Two-dimensional models of smectite dehydration and fluid flow show that neither in situ dehydration nor steady state fluid flow can produce the observed freshening (Saffer and Bekins, 1998). However, it is important to note that these calculations are strongly dependent on porosity and mineralogical data from Site 808 and could change significantly with revised porosity values or additional information about smectite content prior to diagenesis. The chemical and isotopic signatures of the pore fluids suggest contributions from a deep-seated, elevated-temperature (>150°C) fluid source. Some combination of in situ diagenesis and steady state or episodic lateral fluid flow along one or more sediment horizons may be responsible

for this low Cl zone. The sites along the Muroto Transect are aimed at understanding the lateral variability of both fluid flow and progressive in situ diagenesis.

Contrasting Stratigraphic and Deformational Framework along Strike

Seismic profiles of the Ashizuri and Muroto Transects indicate significant differences in prism architecture, structure, and physical properties in the two locations. These differences are assumed to reflect variances in fluid pressure and/or flow regimes, but to date, the mechanisms responsible for such variability are unknown. Structural differences between the Ashizuri and Muroto regions suggest that there may be significant variation in how deformation is accommodated along the two transects; this contrast in behavior may also shed some light on the hydrologic differences. The taper of the prism toe along the Ashizuri Transect (8°–10°) is greater than that of the Muroto toe (4°–5°), a situation that may arise from a relatively stronger décollement to the west or lower internal sediment strength. A strong prism base might arise from smaller fluid overpressures within the fault zone, consistent with the normal polarity reflection. Alternatively, a difference in strength might be due to a variation in clay mineralogy in the décollement zone. Site 1177 drilled through the upper 300 m of the section previously cored at Site 582, sampled the protodécollement zone, and cored the subducting sediment section to document its lithology, physical properties, and clay mineralogy.

SITE SUMMARIES

Site 1173 Summary

We drilled Site 1173 in the trench outer margin (Fig. **F9**) in order to provide a reference for the predeformation status of geological and geochemical characteristics of the incoming sedimentary section. We recognized five lithostratigraphic units (Figs. **F8, F12**): Unit I (0 to 102 mbsf) is Quaternary in age and composed of sandy to muddy turbidites and hemipelagic mud of the outer Nankai trench–wedge facies. Unit II (102 to 344 mbsf) is Quaternary to Pliocene in age and made up of hemipelagic mud with abundant interbeds of volcanic ash that were probably derived from the Kyushu and/or Honshu volcanic arcs (upper Shikoku Basin facies; Fig. **F13**). Unit III (344 to 688 mbsf) consists of Pliocene to middle Miocene bioturbated silty claystone (lower Shikoku Basin facies). The boundary between Units II and III is controlled, in part, by diagenesis. Unequivocal ash beds are abruptly lost and are replaced downsection by siliceous claystones (Fig. **F14**). Unit IV (688 to 725 mbsf) is of probable middle Miocene age and is composed of variegated siliceous claystone and silty claystone (volcaniclastic facies); Unit V (725 mbsf) is middle Miocene basalt.

Biostratigraphic ages provided by calcareous nannofossils indicated a total of 25 biostratigraphic events. The continuous sedimentary section spans the time interval from the Pleistocene (Subzone NN21b) through the middle Miocene (Zone NN5). Magnetostratigraphy clearly identified the Bruhnes/Matuyama boundary (0.78 Ma), Matuyama/Gauss boundary (2.581 Ma), the Gauss/Gilbert boundary (3.58 Ma), and the termination of the Gilbert Chron (5.894 Ma). Paleomagnetic and bio-

F12. Summary of results, Site 1173, p. 55.

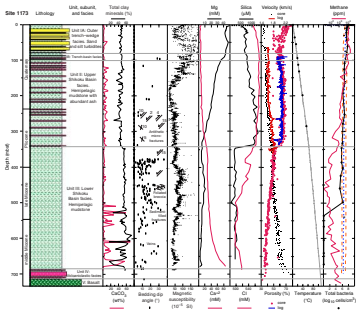

F13. Volcanic ash beds interbedded with silty clay from Unit II, p. 56.

F14. Bioturbated silty claystone and interbedded siliceous claystone from Unit III, p. 57.

stratigraphic ages indicate high sedimentation rates (450–650 m/m.y.) for the turbidite deposits, decreasing rates for the upper Shikoku Basin section (72–77 m/m.y.), and lowest rates for the lower Shikoku Basin section (27–37 m/m.y.).

Deformation structures at Site 1173 are sparse, as expected from a reference site oceanward of the prism. The section above 375 mbsf is characterized by horizontal bedding with occasional steeper dips and microfaults between 250 and 275 mbsf. Bedding dips exceeding 30°, perhaps due to lateral extension associated with normal faulting, occur abruptly at 375 mbsf and continue down to 550 mbsf, below which they occur sporadically to the bottom of the hole. A 30-cm zone of foliated breccia indicates somewhat greater deformation around 440 mbsf. Deeper cores contain rare mineralized veins; a few possible dewatering structures such as thin, sediment-filled veins reflect early compaction processes.

Variations in physical properties correlate well with the lithostratigraphic units. High variability characterizes the turbidites of the outer Nankai Trench wedge, and porosities decrease with depth. Porosity increases at the boundary between the outer Nankai Trench wedge and the upper Shikoku Basin facies and continues to increase slightly with depth. These elevated porosities deviate from a typical compaction profile. An increase in *P*-wave velocities within this interval of increasing porosity suggests that there may be slight cementation. At the boundary between the upper and lower Shikoku Basin facies (~340 mbsf), grain densities increase slightly and porosities decrease sharply. This porosity decrease is accompanied by increasing thermal conductivity, *P*-wave velocity, and resistivity. A gas-probe permeameter showed that ash bands in the upper Shikoku Basin sediments are several orders of magnitude more permeable than the hemipelagites, although the contrast disappears in the lower Shikoku Basin section.

Seven reliable determinations of downhole temperatures were made at depths of 35 to 284 mbsf in Hole 1173A, using the advanced hydraulic piston corer (APC) temperature tool, water-sampling temperature probe, and Davis-Villinger temperature probe. The measured temperatures closely define a linear gradient of 0.183°C/m in the upper 300 m, where the average measured thermal conductivity is ~1.0 W/(m·°C); this yields a conductive heat flow of ~180 mW/m^2 at Site 1173. Deeper than 300 m, thermal conductivities increase by 30%–50%, so the gradient should decrease proportionally, and in situ temperatures of ~110°C are estimated for the bottom of the hole—similar to the basement temperature estimated for Site 808. The heat flow value is somewhat higher than prior determinations of high heat flow near the site and greater than the predicted heat transfer for the 15-m.y. crustal age.

A high-resolution pore fluid concentration-depth profile shows that the pore fluid chemistry has been extensively modified from seawater by both microbially mediated reactions and by abiological, inorganic fluid-rock reactions. The chemical modifications from the microbially mediated reactions provide crucial independent information on the depth range, intensity, and nature of microbial activity in the deep subsurface. Each inorganically controlled dissolved species analyzed (i.e., Cl, Ca, Mg, SiO_2, K, and Na) shows a distinct to sharp discontinuity at 340 mbsf, which corresponds to the lithologic boundary between Units II and III. Furthermore, minima in Cl and Na concentrations and significant inflections in the Mg and Ca profiles occur at ~380–390 mbsf. These features suggest that this horizon may be hydrologically active. A broad ~350-m-thick low-Cl zone within Unit III that has ~9% dilution

relative to seawater requires a source of low-Cl fluid. The geometric similarities between this low-Cl zone and that at ODP Site 808 are striking, except that at Site 808 the dilution relative to seawater is more than twice that observed at this site.

Total organic carbon (TOC) values are low (average = 0.35 wt%) and decrease with depth (0.85 to 0.20 wt%). The C/N ratios indicate the presence of marine organic matter throughout the hole and show a slight increase in the lower ~200 m. The low sulfate and high methane concentrations in the upper section below the sulfate reduction zone are consistent with a bacterial origin. The increase in sulfate concentrations from ~400 to 700 mbsf coupled with the low concentrations of methane may indicate that sulfate is inhibiting production of hydrocarbons that were more abundant at Site 808. The presence of low concentrations of light hydrocarbons (ethane and propane) below 300 m to total depth may be due to some in situ thermal maturation of kerogen in the sediments. The low concentrations of methane at depth and the lack of evidence for any migration of hydrocarbons from above the facies transition (347.3 mbsf) support these conclusions. The microbes observed (~480 m) at temperatures above 90°C in the presence of elevated sulfate concentrations suggest that methanogenesis due to microbial activity is not completely inhibited, although at these temperatures, thermogenic hydrocarbons are likely being produced.

Samples taken for bacterial enumeration show that bacteria are present in all samples to 500 mbsf and thereafter are absent (the detection limit is 4.75×10^5). The population profile generally follows the average line obtained from other ODP sites for the upper 250 m of the hole with a rapid decrease in population size in the upper few meters as the sulfate was depleted. Between 43 and 80 mbsf, there is a significant (sevenfold) increase in bacterial numbers coincident with elevated methane concentrations. At 250 mbsf there is both a temperature boundary for bacteria (45°–50°C, the change from mesophilic to thermophilic populations) and significant differences in interstitial water (IW) chemistry, which complicates interpretation. Further changes occur in IW chemistry at a lithologic boundary at 343 mbsf. Between 250 and 460 mbsf, bacterial numbers are lower than average. Another microbiological temperature boundary (thermophilic to hyperthermophilic populations) occurs at 460 mbsf as temperatures exceed 80°C. One positive enumeration was made in this zone at 500 mbsf and ~85°C, where populations increase by a factor of 13. At this depth there were relatively high concentrations of organic carbon plus increasing concentrations of sulfate, methane, and hydrogen that could support a deep hyperthermophilic population of sulfate-reducing bacteria.

Tracer tests were successfully carried out on two APC cores and two extended core barrel (XCB) cores with both perfluorocarbon tracer (PFT) and fluorescent microspheres. PFT was detected in the center and midway between the center and the outside in some APC core sections; however, PFT was absent from the center of the XCB core sections. In contrast, microspheres were generally absent in samples taken midway between the center and the outside of the core in both APC cores and one of the XCB cores and were only present in the centers of some of the XCB core sections. These results suggest that intrusion of microspheres into the center of the cores was a result of postrecovery handling and not diffusion of drilling fluid during coring. This is the first time fluorescent microsphere tracers have been used during the collection of cores with the XCB.

Hole 1173A was logged with both the triple combination logging string (spectral gamma ray, dual-induction resistivity, lithodensity, and neutron porosity tools) and the Formation MicroScanner (FMS) and dipole sonic imager (DSI) tools. The interval from 65 to 373 mbsf was logged in two passes, and high-quality compressional and shear travel time data and FMS images were acquired. During the second pass, a new low-frequency (<1 kHz) dipole source was used on the DSI and produced excellent shear waveforms despite the very low formation velocity. Logging results are generally consistent with the homogeneous hemipelagic core lithology, with few identifiable lithologic boundaries in the logged interval. Density is low from 97 to 336 mbsf, with a slight gradual decrease with depth, then sharply higher in the 358–440 mbsf interval. Compressional and shear wave velocities are nearly constant with depth to 225 mbsf, then increase with depth. Velocities decrease sharply in the short logged interval below 348 mbsf, corresponding to the Unit II/III boundary. Numerous ash layers and other sedimentologic and diagenetic features observed in the cores were well imaged by both FMS passes, which should permit high-resolution core-log integration.

Site 1174 Summary

Site 1174 (ENT-03A) is located in the protothrust zone of the Nankai accretionary prism (Fig. **F9**) and was designed to sample a zone of incipient prism deformation. When combined with our reference Site 1173 (~11 km seaward) and Site 808 (~2 km landward at the frontal thrust), Site 1174 provides a transect of stratigraphy, structural data, physical properties, and geochemical gradients across the deformation front of the accretionary prism.

We recognized five lithostratigraphic units and three subunits at Site 1174 (Figs. **F8, F15**). Unit I (slope-apron facies) is Quaternary in age and extends from the seafloor to a sub-bottom depth of 4.00 mbsf. This facies is composed mostly of mud that was deposited on the lowermost trench slope by hemipelagic settling. Unit II (trench-wedge facies) is Quaternary in age and includes three subunits. Subunit IIA (axial trench–wedge facies) extends from 4.00 to 314.55 mbsf and is characterized by thick sand turbidites, silt turbidites, and hemipelagic mud (Fig. **F16**). The lithologies of Subunit IIB (314.55–431.55 mbsf) are limited to silt turbidites and hemipelagic mud, whereas Subunit IIC (431.55–483.23 mbsf) is composed of hemipelagic mud, volcanic ash, and silt turbidites. The gradual transformation in facies character downsection is consistent with a change in depositional environment from the outer trench wedge to abyssal floor. Unit III (upper Shikoku Basin facies) is Quaternary to Pliocene in age and extends from 483.23 to 660.99 mbsf. Lithologies within this unit include hemipelagic mudstone and volcanic ash; the lower unit boundary coincides with the deepest identifiable bed of vitric tuff. In contrast, Unit IV (lower Shikoku Basin facies) contains mostly bioturbated mudstone with sporadic interbeds and nodules of carbonate-cemented claystone and siliceous claystone. Replacement of glass shards by smectite and zeolites (clinoptilolite or heulandite) increases gradually with depth and is more extreme in finer-grained deposits. As a consequence, both ash to bentonite diagenesis and temporal changes in pyroclastic influx govern the lithologic distinction between the Upper and lower Shikoku Basin facies. The unit boundary shifts upsection as Shikoku Basin deposits migrate toward the Nankai deformation front and become increasingly affected by rapid burial and heating beneath the trench wedge. The

F15. Summary of results, Site 1174, p. 58.

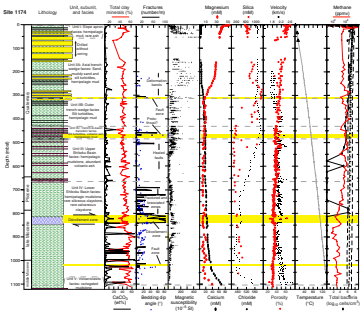

F16. Graded interval of medium- to fine-grained sand, p. 59.

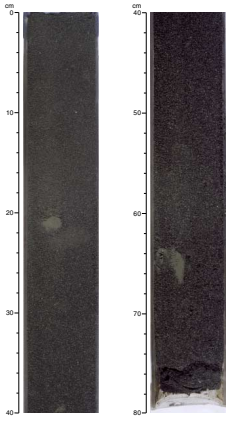

lowermost stratigraphic unit at Site 1174, Unit V, begins at a depth of 1102.45 mbsf. We drilled only 8.86 m of variegated claystone in this middle Miocene volcaniclastic facies.

Deformation bands are well developed between 218 and 306 mbsf (Fig. **F17**) and are concentrated in two oppositely inclined sets striking at 033° with the acute bisectrix inclined 10°NW from vertical (Fig. **F18**). They occur immediately above a narrow but abruptly sheared interval that, with indications of reverse movement and a paleomagnetically restored southeast dip, may be a backthrust. Between 470 and 506 mbsf, fractured and markedly steepened bedding may represent a thrust; no significant deformation was seen in the cores equivalent to the thrust apparent on the seismic profile at 550 mbsf. Narrow, widely spaced zones of fractures and brecciation characterize the interval between 688 and 807 mbsf. Between 807.6 and 840.20 mbsf an irregular downward increase in intensity of inclined fractures and fineness of brecciation defines the décollement, which is thicker and more heterogeneous than at Site 808 and more thoroughly comminuted in its lower part (Figs. **F19, F20**). The underthrust sediments show little tectonic deformation; however, zones of significant bed steepening were noted between 950 and 1000 mbsf and around 1020 mbsf, the latter accompanied by evidence for shear deformation.

Nannofossil assemblages are indicative of the Pleistocene (Subzone NN21b) to middle Miocene (Zone NN6) ages. Twenty-three biostratigraphic events are recognized. Nannofossils are common and generally moderately preserved in the Pleistocene, whereas Pliocene and Miocene nannofossils are rare and mostly poorly preserved. Sedimentation rates based on biostratigraphy are 630–770 m/m.y. for the late Quaternary and are significantly lower (11–125 m/m.y.) for deposits older than 0.8 Ma.

Paleomagnetic results indicate that the Brunhes Chron (0–0.78 Ma) ranges from 0 to 544.70 mbsf and extends through the trench-wedge turbidites. The Matuyama Chron occurs from 544.70 to 685.95 mbsf, the Gauss Chron, from 685.95 to 727.85 mbsf, and the Gilbert Chron, from 727.85 to 802.07 mbsf. High magnetic intensities occur from 0 to ~550 mbsf, below which they drop to low values to the bottom of the hole.

The main characteristics of the interstitial water concentration-depth profiles at Site 1174 are similar to those at Site 808. There is an intense, very shallow, sulfate reduction zone, and alkalinity and ammonium concentrations peak in the uppermost 200 m of the section. The solutes that are controlled by fluid-rock reactions, such as Cl, Na, and Si, have sharp changes in their gradients at a depth that corresponds to the boundary between the trench wedge and Shikoku Basin facies (lithostratigraphic Units II/III boundary). At the depth that corresponds to the thrust intersection (~470 ± 5 mbsf), there are also significant excursions, most distinctly exhibited in the Cl and Si concentrations, that may indicate hydrologic activity. The chemical changes across the major tectonic feature, the décollement, are subtler, but a high-resolution record of pore fluid chemistry was recovered across and within the Nankai Trough décollement for the first time. A local Cl maximum of 496 mM within the décollement decreases smoothly to ~485 mM ~50 m above the décollement zone, whereas it decreases very sharply (~10 mM) in the 10 m below the structure. The cause of the Cl maximum in the décollement is as yet unclear. A low-Cl zone in the 200-m interval below the décollement, with minimum concentrations that are ~17% diluted relative to seawater, occurs at an almost identical distance below

F17. Deformation bands, p. 60.

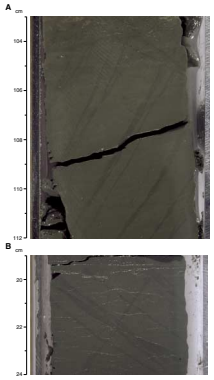

F18. Stereographic equal-area lower hemisphere projections of deformation bands, p. 61.

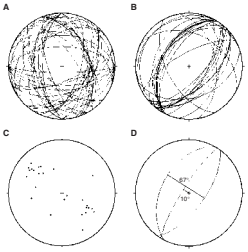

F19. Upper and lower parts of the décollement zone, p. 62.

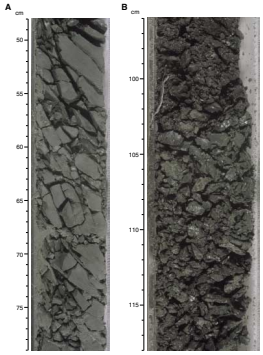

F20. Details of fracturing across the décollement zone, p. 63.

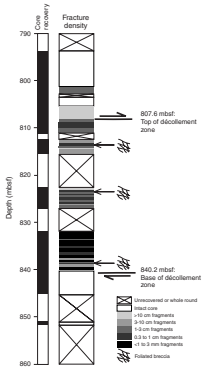

the décollement at Site 808. The dilution, however, is ~21% at Site 808, ~17% at Site 1174, and considerably less (~9%) at reference Site 1173. In the lowermost ~100 m of the underthrust section, Cl concentrations increase, approaching seawater concentration at 1110 mbsf. Hydration reactions in the lower volcaniclastic or an underlying upper basement fluid flow system may be responsible for the increase in the Cl concentrations.

Dissolved silica concentrations appear to be controlled by biogenic silica dissolution in the trench-wedge sediments, by volcanic ash diagenesis in the upper Shikoku Basin facies, and by the low-Cl source plus in situ silicate reactions at >70° to ~130° in the lower Shikoku Basin facies. Dissolved sulfate increases below the sulfate reduction zone, 1–2 mM below the upper and lower Shikoku Basin facies boundary sediments, at ~660 mbsf, reaching 8–10 mM below the depth interval of the Cl minimum and remaining constant to the bottom of the section. At Site 1173 the first sulfate increase below the sulfate reduction zone is observed at a much shallower burial depth, ~400 m shallower than at Site 1174. The sulfate distributions at these sites may reflect a dynamic relationship among sedimentation rates, temperature, and microbial sulfate reduction rates.

Organic matter decreases with depth and low TOC values are low (0.90 to 0.11 wt%; average = ~0.38 wt%) in the core. The C/N ratios indicate the presence of marine organic matter with only a slight increase in the upper trench–wedge facies (~200 mbsf) and in the lower Shikoku Basin facies below the décollement (~1000 mbsf). Discrete intervals of elevated methane concentrations are present between 225 and 700 mbsf. Minor amounts of ethane (200–800 mbsf) and propane (400–650 and 950–1110 mbsf) are probably attributable to some in situ thermal maturation of organic matter.

Microorganisms were enumerated in 40 samples collected from the surface to 1100 mbsf at Site 1174. With the exception of two samples with low abundances (~1.8×10^6 cells/cm^3) in the sandy layers at 26 and 66 mbsf, abundances from the surface to 400 mbsf were close to values predicted based on data from previous ODP sites. Abundances were lower than predicted below 400 mbsf. The decrease may relate to the relatively high temperature gradient at Site 1174. Cell counts dropped below the detection limit at 528 mbsf and remained so until just above the décollement. Abundances at 778 and 789 mbsf were 4.8 and 4.2×10^6 cells/cm^3, respectively; no cells were detected below these depths. Nineteen whole-round samples were used to inoculate anaerobic growth media and were maintained at the estimated in situ temperature. Samples were chosen from the surface through the known hypothermophilic region (113°C) (Blöchl et al., 1997), and subsamples at five depths were targeted for incubation at in situ pressure and temperature.

Porosities within the axial and outer trench–wedge facies (Subunits IIA and IIB) are characterized by high variability and generally decrease with depth. Porosity decreases across the boundary between the outer trench wedge and trench to basin transition facies (Subunit IIB/IIC boundary). Within the transitional facies, porosities are less scattered and decrease slightly with depth. The upper Shikoku Basin facies (Unit III) is characterized by nearly constant porosities, which is a deviation from normal compaction trends. Surprisingly, a high velocity interval between 510 and 520 mbsf is associated with an interval of elevated porosity. At the top of the lower Shikoku basin facies (Unit IV; ~660 mbsf), another high-velocity interval occurs. Porosities within the lower

Shikoku Basin facies resume a compaction trend of decreasing porosity with depth. Porosities increase sharply by 2%–4% at the top of the underthrust sequence. This porosity increase is accompanied by a decrease in velocity and increase of electrical conductivity. However, the anisotropy of electrical conductivity is higher in the underthrust sediments than above the décollement zone. Porosities and velocities increase with depth within the underthrust sediments, whereas electrical conductivities decrease. In contrast to Site 808, porosities within the décollement are not significantly lower than above and below it, although values are somewhat scattered.

Uncalibrated gas permeameter measurements were made throughout the section. Shallower than 600 mbsf, silt-rich and ash horizons showed higher values than the silty clays. The axial trench–wedge sands gave the highest values, and the lowermost silty clays recovered gave the lowest.

In situ temperature measurements to a depth of 65.5 mbsf and laboratory thermal conductivity measurements indicate a near-surface heat flow of 180 mW/m². If heat flow is purely conductive and steady state, a temperature of ~140°C is projected for the bottom of the hole.

Site 1175 Summary

Site 1175 (ENT-07A) was designed to penetrate the slope sediments that cover the large thrust-slice zone just landward of a major OOST (Fig. F11). Investigation of the age and lithologic characteristics would provide information on (1) the history of accretion, uplift, and deformation of the prism and (2) sedimentation within a trench-slope basin.

We cored three lithostratigraphic units at Site 1175 (Figs. F8B, F21). Unit I (upper slope–basin facies) begins at the seafloor and ends at a sub-bottom depth of 224.75 mbsf. Lithologies include nannofossil-rich hemipelagic mud, volcanic ash, and thin turbidites that range in texture from sand to silty sand, clayey sand, and silt. The most characteristic feature of Unit I is the common occurrence of contorted stratification (Fig. F22). There are eight discrete zones of soft-sediment deformation. Typical manifestations include variably inclined bedding, small-scale folding, and, in extreme cases, stratal fragmentation. The disruption was probably caused by submarine slumps and debris flows. Unit II (middle slope–basin facies) extends from 224.75 to 301.64 mbsf. Lithologies include hemipelagic mud, poorly sorted muddy sand to sandy mud, sporadic interbeds of volcanic ash, and rare occurrences of thin sand or silt turbidites. The unusual lithology of muddy sand is diagnostic of Unit II and probably was transported downslope by sandy debris flows or mudflows. Unit III (slope to prism transition) begins at 301.64 mbsf and ends at 435.40 mbsf. This unit is typified by carbonate-poor hemipelagic mud with numerous interbeds of silt and silty sand turbidites. The most striking lithology, however, is gravel to pebbly mudstone (Fig. F23). Its characteristics include disorganized and poorly sorted clast fabric, lack of internal stratification, partial to complete support of clasts by a matrix of clayey silt, and subrounded to rounded clasts up to 5.5 cm in size. A polymictic clast population was transported downslope by debris flows. The boundary between the lowermost slope sediment and the top of the accretionary prism cannot be defined with certainty using lithologic criteria, but it probably occurs within the upper 25–30 m of Unit III.

Site 1175 exhibits little evidence for tectonic deformation. However, the upper 205 m shows intervals of recumbent, isoclinal slump folding

F21. Summary of results, Site 1175, p. 64.

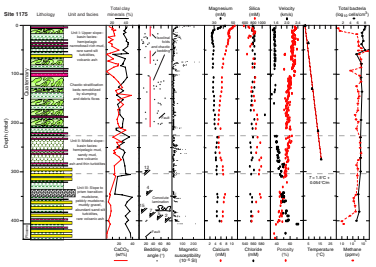

F22. Chaotic bedding of Unit I, p. 65.

F23. Pebbly mudstone of Unit III, p. 66.

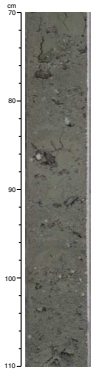

and disaggregated sediment interlayered with subhorizontal intact bedding. Fold orientations suggest the slumping was northward directed. Below 220 mbsf, bedding is subhorizontal, except for localized chaotic zones between 350 and 388 mbsf and dips up to 21° at 400 mbsf. Core-scale faults, probably compaction related, occur from 298 to 302 mbsf and sporadically from 340 to 435 mbsf. Possible web structure occurs in sands at 406.9 and 425.8 mbsf; near the bottom of the hole, an indurated sand contains several low-angle small faults.

Biostratigraphic age control was provided by calcareous nannofossils that are well preserved and abundant throughout the section. A total of ten biostratigraphic events were identified within the nannofossil assemblages. The continuous sedimentary record spans the time interval from the Pliocene (Zone NN18) through the Pleistocene (Subzone NN21b). Based on the biostratigraphic ages, sedimentation rates for the upper sedimentary units show high sedimentation rates (0.52 m/k.y.) for the upper to middle slope–basin deposits, with decreasing rates for the slope to prism transition (0.13 m/k.y.).

Hole 1175A inclination data after alternating-field (AF) demagnetization at 30 mT allowed interpretation of geomagnetic polarity changes from late Pliocene to Pleistocene. The 0.78 Ma Brunhes/Matuyama boundary is interpreted to occur at 298.80 mbsf (interval 32X-5, 80 cm). Seven short reversal events were observed in the Brunhes Chron and may represent geomagnetic excursions.

In Hole 1175A, pore fluids are less intensively modified from seawater than the pore fluids in Holes 1173A and 1174A. The main characteristics of the pore fluid concentration-depth profiles indicate that the intense microbially mediated reactions occur in the top <200 mbsf of the section. Microbial sulfate reduction is complete at ~15 mbsf. The alkalinity maximum also occurs at this depth. Only relatively small changes in the chemical gradients occur throughout the section and across the major lithologic boundaries in the abiogenic components. Volcanic ash alteration is insignificant because of the rather low geothermal gradient of 54°C/km. Instead of ash alteration, as indicated by the Ca, Mg, and alkalinity concentration-depth profiles, carbonate, particularly dolomite, diagenesis is the dominant diagenetic reaction. Dolomite forms both by direct precipitation of authigenic dolomite and by replacement of precursor biogenic calcite, which is abundant in this section. Carbonate diagenesis should influence some of the index physical properties such as porosity and density. An unidentified silicate reaction occurring below the drilled section controls the concentration profiles of K, Na, Si, and alkalinity below ~300 mbsf, corresponding to lithostratigraphic Unit III. The inferred diffusion of lower chlorinity interglacial water into the pore fluids at Sites 1173 and 1174 is absent at this site. One possible explanation is that the signal has been erased by widespread slumping in Unit I.

The sediments at Site 1175 contain low inorganic carbon (~0.11–4.59 wt%), and carbonate contents range up to 40 wt%, resulting in very immature organic matter and low hydrocarbon abundances. The low sulfate and high methane concentrations in sediments below the sulfate reduction zone and throughout Hole 1175A are consistent with a bacterial origin.

Bacterial abundance was enumerated in 18 samples obtained at Site 1175. The abundance near the surface is 6.97×10^7 cells/cm^3 and declines rapidly, which is consistent with the decrease in sulfate concentrations. Abundances increase below 14.6 mbsf and are consistent with increases in methane concentrations. The sample at 50.8 mbsf is nota-

ble in that it contains 7.28 × 10^7 cells/cm^3 (i.e., slightly more bacteria than the near-surface sample). This is followed immediately with almost the lowest population enumerated of 3.71 × 10^5 cells/cm^3 at 59 mbsf. The deepest sample is 400 mbsf with 3.59 × 105 cells/cm^3, equivalent to 0.5% of the near-surface population. Estimates of drilling fluid intrusion into the interior of the cores examined at this site range from below detection to 0.02 µL/g. In addition to the onboard assays, 17 whole-round cores were taken for shipboard enrichment cultures, cell viability, and shore-based microbiological analysis to measure potential bacterial activities, culture microorganisms, characterize nucleic acids, and investigate fatty acid biomarkers.

Porosities within the upper slope–basin facies (Unit I) are characterized by high variability and decrease slightly with depth from values of 62%–70% at the mudline to 61%–68% at ~100 mbsf. Porosities decrease abruptly at ~100 mbsf to values of 57%–61% and then decrease gradually to the transition between the upper and middle slope–basin facies (220 mbsf). Below 220 mbsf (within the middle and lower slope–basin facies), porosity decreases more rapidly with depth than in the upper slope–basin facies, reaching values of 38%–47% at 400 mbsf. The rapid decrease in porosity below 220 mbsf coincides with increasing *P*-wave velocity. There is no clear change in porosity, bulk density, or grain density at the depth of the middle slope–basin/lower slope–basin facies boundary (301 mbsf; Units II and III). A spike of high velocity and impedance 20 m above this transition may correspond to a seismic reflector. The depth of this spike coincides with the depth of the upper unconformity on the depth converted seismic profile. Four successful in situ temperature measurements at Site 1175 indicated a thermal gradient of 0.054°C/m.

Gas-probe permeameter measurements illustrate the huge influence of lithology. Uniformly low values are given by the hemipelagic clays that dominate the section, whereas a coarse, friable black ash at 23 mbsf gave a measurement six orders of magnitude higher. Turbiditic sands between 60 and 90 mbsf also yielded exceptionally high values. Thin bands of white-gray ashes also give relatively high values, in agreement with shallow, unaltered ashes at the other sites.

This site revealed that the age of accretion of the large thrust-slice zone is very young (<2 Ma). The young age of the accretion indicates rapid growth of the frontal part of the Nankai accretionary prism, ~40 km oceanward growth in 2 m.y. This rate of growth provides a significant revision to first order constraints for kinematic, structural, and hydrogeologic modeling of the prism.

Site 1176 Summary

The objective of Site 1176 was to determine the nature of accreted sediments of the large thrust-slice zone as well as to understand deformation and potential fluid flow related to a major out-of-sequence thrust (Fig. **F11**). The OOST itself, however, was not penetrated.

We recognized three lithostratigraphic units at Site 1176 (Figs. **F8B, F24**). Unit I (upper slope–basin facies) extends from the seafloor to 195.79 mbsf. Its lithologies include nannofossil-rich mud, volcanic ash, and sand to silt turbidites. The principal processes of sedimentation for Unit I were hemipelagic settling and turbidity currents, with occasional volcanic ash falls and remobilization by slumping. Unit II (middle slope–basin facies) extends from 195.97 to 223.54 mbsf. In addition to typical hemipelagic mud, Unit II contains sandy mudstone and rare

F24. Summary of results, Site 1176, p. 67.

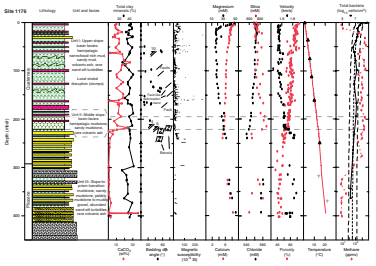

beds of volcanic ash. Deposition of this facies occurred from muddy debris flows, routine settling of suspended sediment, and occasional ash falls. Unit III was cored to a depth of 440.36 mbsf and contains abundant interbeds of sand to silt turbidites, carbonate-poor hemipelagic mudstone, pebbly mudstone, gravel (Fig. F25), and rare volcanic ash. The primary depositional environment for this unit was probably a trench-fan system fed by a transverse submarine canyon, and depletion of carbonate supports the idea of deposition below the carbonate compensation depth (CCD). The petrographic compositions of sands and gravels, rich in sedimentary lithic fragments and quartz, show that their provenance is southwest Japan as typically represented by the Shimanto Belt. The junction between the lowermost slope sediment and the top of the accretionary prism probably coincides with the boundary between Units II and III.

F25. Pebbles and gravel of quartz and lithic clasts, p. 68.

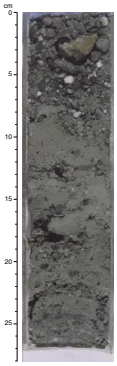

Site 1176 can be divided into two structural domains: slope basin and accretionary prism. Deformation of the slope-basin sediments (0–224 mbsf) is characterized by inclined bedding intervals in which slump folds together with contorted and chaotically mixed bedding are locally developed. These features are interpreted to record the effects of active tilting and uplifting of the slope basin. Small faults are thought to result from extensional response to this tilting and uplift of the basin and/or burial compactional strains. In contrast, deformation structures are almost absent in the accreted sediments (below 224 mbsf), although core recovery was very poor. However, the apparently consistent near-horizontal bedding may reflect the flat part of a hanging-wall anticline formed in association with an underlying thrust.

Biostratigraphic age control was provided by calcareous nannofossils. Nannofossil assemblages are of Pliocene (Zone NN16) to Pleistocene age (Subzone NN21b) according to nine recognized biostratigraphic events. Although nannofossils are common and generally moderately preserved in the upper Pleistocene, nannofossils from sediments older than 1 Ma are rare and poorly preserved. Age models based on biostratigraphy indicate sedimentation rates of ~0.07–0.26 m/k.y.

Inclination data of Hole 1176A after AF demagnetization at 30 mT provided useful information for interpretation of geomagnetic polarity changes from the late Pliocene to the Pleistocene. The Brunhes/Matuyama boundary (0.78 Ma) is interpreted to occur at 199.55 mbsf. Seven short reversal events were observed in the Brunhes Chron and may represent geomagnetic excursions in this chron.

The most intense microbially mediated reactions occur in the top <100 mbsf of the section. Microbial sulfate reduction is complete at ~20 mbsf. In the top half of this zone, the sulfate reduction rate decreases linearly with depth, whereas in the lower half, maximum sulfate reduction occurs at the base of the zone; the alkalinity produced is involved in carbonate reactions, and the ammonium produced is involved in clay ion exchange reactions.

The alkalinity maximum and Ca and Mg minima coincide with the depth of the base of the sulfate reduction zone; thus, this depth interval is also characterized by intense carbonate diagenesis. The Ca and Mg concentration profiles indicate that in the sulfate reduction zone both authigenic dolomite precipitation and replacement of a precursor biogenic calcite occur. Deeper, however, through the upper and middle slope–basin section, replacement of a precursor calcite is the only dolomitization reaction.

Volcanic ash or other silicate diagenetic reactions are minimal because of the low geothermal gradient of 56°C/km. Diatom dissolution

may control the pore fluid silica concentration. At the base of the section, pore fluids have a composition close to seawater, as indicated by the return to seawater concentrations of all abiogenic components, except for K. The Cl concentration profile is consistent with diffusion between a low-Cl zone at greater depth and the seafloor. Because of poor recovery, the location of the low-Cl zone is poorly defined but is constrained to be between 240 and 320 mbsf. The low-Cl fluid is enriched in Ca and depleted in Na, K, and Mg. A chemically similar fluid was identified at Site 1174.

Diffusion of low-chlorinity interglacial seawater into the sediment section is not observed at this site. As at Site 1175, this may be the result of repeated slope-failure events and sediment reworking. At greater depths, the residual signal from the glacial ocean seawater may have been overprinted by diffusion.

The total carbon content for the sediments examined between 200 and 401.6 mbsf at Site 1176 ranged from 0.05 to 2.25 wt%. The highest carbon value (2.25 wt% at 340 m) was dominated by a terrestrial component likely derived from fan debris flow to the trench sediments. The sulfur content showed a trend similar to TOC, with the highest values of sulfur (1.05 and 2.07 wt%) coincident with the highest TOC values (0.86 and 2.25 wt%). The inorganic carbon (~0.05–2.6 wt%) and high carbonate content (up to ~35 wt%) are similar to values observed at Site 1175. Methane concentrations in sediments below the sulfate reduction zone (~9.5 m) are consistent with a bacterial origin. Methane dominates the composition of the hydrocarbons measured throughout Hole 1176A.

Bacterial abundance was enumerated in 18 samples obtained at Site 1176. Abundance at the surface was 6.67×10^8 cells/cm^3. The deepest sample is 363.49 mbsf with 1.71×10^6 cells/cm^3, representing 0.25% of the surface population. The rapid decline of bacterial populations from the surface is consistent with the decrease in sulfate concentrations to near zero at 14.6 mbsf. The decline in bacterial abundance with depth follows the predicted depth/population size relationship very closely. In addition to the onboard assays, 11 whole-round cores were taken for shipboard enrichment cultures, cell viability, and shore-based microbiological analysis to measure potential bacterial activities, culture microorganisms, characterize nucleic acids, and investigate fatty acid biomarkers.

Porosities decrease gradually with depth in the upper slope–basin facies (Unit I), from values of ~65%–73% at the mudline to 55%–60% at 200 mbsf. Within the upper slope–basin facies, there is considerable scatter in porosity, with values ranging from 51% to 73%. This scatter may be related to the inferred deposition of this unit by slope failure processes. No clear changes in index properties occur at the boundary between the upper and middle slope–basin facies (Units I and II). Within the middle slope–basin facies (Unit II), porosity continues to decrease gradually with depth, following the same trend as observed for the upper slope–basin facies. Changes in index properties correlate with the boundary between the middle slope–basin and accretionary prism facies (Units II and III) at 225 mbsf. Porosity decreases from 53%–57% to 48%–54% across this boundary. Velocity and formation factor also increase at the top of Unit III. Within Unit III, porosities decrease with depth, reaching ~40%–47% by ~310 mbsf. From this depth to 405 mbsf, porosities remain constant, with values ranging from ~40%–47%.

Five successful in situ temperature measurements indicate a thermal gradient of 0.056°C/m.

Results from the gas permeameter at Site 1176 are slightly different from those from other sites in that the range is even greater and there is no general decrease with depth. Throughout the hole the hemipelagic clays show low values with greater scatter than elsewhere, and in the upper half of the section (above 200 mbsf), sands, gravels, and especially ashes gave much higher values. In the lower half of the hole, sands and gravels give high measurements, even at the bottom of the hole.

This site provided information regarding the nature of accreted sediments that compose the large thrust-slice zone including the slope-basin transition. Coarse clastic sediments of Outer Zone origin, perhaps transported through a transverse canyon, are the dominant lithology of the accreted sediments. The accreted section of this zone is, thus, very different from the axially transported, volcaniclastic-rich trench sediments at Sites 1173, 1174, and 808. The age of the prism is probably younger than 2 Ma, and slope-basin development initiated <1 Ma, suggesting extraordinarily rapid growth of the prism.

Site 1177 Summary

The science objective of Site 1177 was to study the stratigraphic, geochemical, and physical properties framework of a reference site along the Ashizuri Transect (Fig. **F10**). This transect includes DSDP Sites 297, 298, 582, and 583.

We recognized five lithostratigraphic units at Site 1177 (Figs. **F8A, F26**). Unit I (upper Shikoku Basin facies) is Pliocene in age (300.20 to 401.76 mbsf) and consists mainly of weakly indurated hemipelagic mud interbedded with fresh volcanic ash. Unit II (lower Shikoku hemipelagic facies) is late Miocene in age (401.76 to 449.30 mbsf) and is composed almost entirely of a more strongly indurated hemipelagic mudstone. Unit III (lower Shikoku turbidite facies) is early to late Miocene in age (449.30 to 748.35 mbsf) and consists of turbidite sand, silty sand, gravel, mudstone-clast conglomerate, and hemipelagic mudstone, plus a few thin layers of carbonate-cemented claystone and siliceous claystone. There are four sand-rich packets within this facies, and most of the siliciclastic sands contain abundant woody plant fragments (Fig. **F27**). Mudstones display vivid color contrasts due to variations in clay mineralogy. Sediment dispersal evidently occurred through a broad system of coalescing submarine fans. Unit IV (volcaniclastic-rich facies) is early Miocene in age (748.35 to 831.08 mbsf). This unit consists of variegated mudstone to claystone, volcanic ash (Fig. **F28**), and silt turbidites with both volcaniclastic and siliciclastic compositions. Many of the mudstone beds are enriched in expandable clay minerals. Unit V is basaltic basement (831.08 to 832.13 mbsf) and is probably early Miocene in age. The basalt contains one pillow structure, and an intrusive contact with overlying sediment is highly altered (Fig. **F29**).

Deformation structures at this site, oceanward of the prism, are very sparse, more so than at the reference site at the Muroto Transect. This near absence at Site 1177 of structures and bedding dips >10° may result from slower rates of sedimentation, slight differences in lithology, or differences in topography of the substrate. Early soft-sediment compaction-related structures are present between 748 and 831 mbsf; the main tectonic structure is a faulted and diagenetically altered interval between 579.45 and 581.10 mbsf. The basalt at the bottom of Hole 1177A, at 831 mbsf, exhibits glassy rinds at its contact with the overlying sedi-

F26. Summary of results, Site 1177, p. 69.

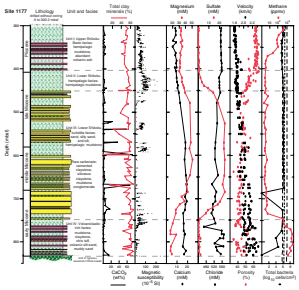

F27. Wood-rich sandy turbidite interbedded with silty claystone, p. 70.

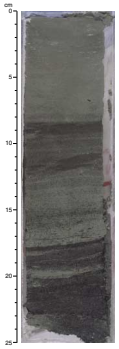

F28. Laminated and bioturbated volcanic ash, p. 71.

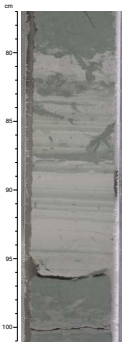

F29. Contact between green basal mudstone and basalt, p. 72.

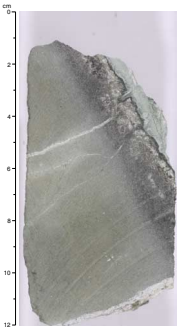

ment and networks of veins bearing calcite and/or chlorite in complex interrelationships.

Biostratigraphic age control was provided by calcareous nannofossils, although their abundance and states of preservation were generally poor throughout the sequence; major intervals are barren of nannofossils. A total of 11 biostratigraphic events were identified. The continuous sedimentary section spans the time interval from the Pliocene (Zone NN18) through the early Miocene (Zones NN4–NN2). The biostratigraphic age estimates indicate an average sedimentation rate for the late Pliocene of 87 m/m.y. and a lower sedimentation rate of 28.7 m/m.y. for the lower Miocene to Pliocene sediments.

Magnetic inclination data of Hole 1177A after AF demagnetization at 30 mT were useful for interpretation of geomagnetic polarity changes from the early Miocene to Pliocene. The Brunhes/Matuyama boundary is expected to occur above the initial coring depth of 300 mbsf. The Reunion Event (2.14 Ma) during the Matuyama Chron is interpreted to occur at 301.85 mbsf. The Matuyama/Gauss (2.581 Ma) and Gauss/Gilbert (3.58 Ma) boundaries are interpreted to occur at 328.55 and 384.25 mbsf, respectively. The beginning of Chron C3A (5.894 Ma) is identified to occur at 427.45 mbsf.

Sharp chemical discontinuities between and within lithostratigraphic units, particularly intense in the Cl, Na, K, sulfate, and alkalinity concentrations, and a high-sulfate turbidite unit in the middle half of the section are outstanding characteristics of Site 1177 pore fluid concentration-depth profiles. Discontinuities within lithostratigraphic units are unique for this site and were not observed at Sites 1173, 1174, or 808. The chemical discontinuities correspond to discontinuities in physical properties, suggesting that solute and fluid transport out of specific sediment intervals may be retarded. Alternatively, these zones may reflect the recent onset of diagenetic reactions in compositionally distinct layers, such as ashes. The sharpest discontinuity occurs at ~410 mbsf, at the boundary between lithostratigraphic Units I and II. The concentration-depth profiles are therefore only continuous in Units I and II but show unusual variance in Units III and IV. The most conspicuous interval of this character was identified close to the bottom of the sediment section (775–805 mbsf).

Within Unit III there is a general decrease in Cl concentration; the minimum value is ~7% fresher than modern seawater concentration. This freshening is most plausibly produced by in situ smectite dehydration in combination with Cl uptake by an authigenic hydrous silicate. Na and K profiles show similar trends, but to a lesser extent. Sulfate reduction is complete in Units I and IV, driven by microbial activity. In Unit III, sulfate concentration is high, ~86% of the modern seawater value, indicating that since burial little microbial activity has occurred. This is probably the result of the very low content of nonwoody, labile organic matter available for microbial activity in the turbidites. Most of the labile organic matter was microbially oxidized when the turbidites were at or close to the seafloor and sulfate diffused into this section.

The important diagenetic reactions are ash alteration, particularly reflected in the Ca, Na, and K profiles, carbonate formation as reflected in the Ca and alkalinity profiles, and opal-A dissolution as reflected in the Si profile.

The TOC contents ranged from 0.03 to 1.62 wt%, with an average value of 0.45 wt%. The highest carbon values were measured in the Shikoku turbidite facies sediments (Unit III), which contained a terrestrial component characterized by plant detritus and pieces of wood.

The sulfur content ranged from 0 to 0.81 wt%, with the highest concentrations occurring between 400–520 mbsf and 650–770 mbsf. The C/N ratios indicated that a mixture of both marine and terrigenous sources were contributing to the overall sediment composition. Unlike Sites 1175 and 1176, the inorganic carbon (~0.78 wt%) and carbonate contents (~2.7 wt%) were low with the exception of some thin-bedded carbonate-cemented layers (up to 65 wt%) in the Shikoku turbidite facies (Unit III).

Methane concentrations in sediments below the sulfate reduction zone (~4.5 m down to 734 mbsf) are consistent with a bacterial origin. The $C_1/(C_1+C_2)$ ratio for hydrocarbons in sediments below 750 mbsf plot within the mixing zone, suggesting that more than one source of hydrocarbons may be present.

Microorganisms were enumerated in 23 samples collected from 300 to 830 mbsf. Bacteria are present in all but two samples (687 and 830 mbsf) at abundances that are generally lower than expected based on results from previous ODP sites. A small, but statistically significant increase in bacterial populations occurs from 380 to ~740 mbsf that correlates with elevated sulfate concentrations in the interstitial water between these depths. The continued presence of sulfate, unexpected when bacteria are present at ~10^6 cells/cm^3, may be related to very low organic carbon concentrations in the sediment preventing significant amounts of bacterial sulfate reduction. A total of 21 whole-round cores were taken for shipboard enrichment cultures, cell viability, and shore-based microbiological analysis to measure potential bacterial activities, culture microorganisms, characterize nucleic acids, and investigate fatty acid biomarkers.

Variations in physical properties at Site 1177 correlate well with the lithostratigraphic units. Units I and II are both characterized by low scatter in porosity. Unit I maintains a nearly constant porosity of 60%–65%. At the top of Unit II (402 mbsf), porosities begin to decrease rapidly with depth, decreasing to 45%–53% by 450 mbsf. Unit III is characterized by a gradual decrease in porosity with depth and by increased scatter that may be due to lithologic variations in this turbidite-rich sequence. Unit IV exhibits significant scatter and shows no clear trend with depth. An excursion to lower porosity (~40%) at 475–510 mbsf within Unit III occurs in a sandy section. Anomalously high porosity (~8%–15% higher than in surrounding sediments) within Unit IV occurs in a 30-m-thick zone between 765 and 795 mbsf. Low vertical *P*-wave velocities and formation factors also characterize this zone.

Most gas permeameter determinations at Site 1177 range around the values given by the background hemipelagites. Carbonate-cemented claystones at 540 and 591 mbsf give slightly higher values, as do the altered ashes of Unit IV, but the increase is small. The upper sands in Unit III account for all of the high measurements at the site. Numerous wood-bearing silty sands were measured in the lower part of Unit III, but most give identical results to the background hemipelagites, suggesting blockage of the pore connections, perhaps by smectite.

In addition to serving as the reference site for the Ashizuri Transect, Site 1177 provides a comparison to the Muroto reference site (Site 1173). Comparison of the two sites will aid our understanding of the evolution of the Nankai Trough accretionary prism in two different geologic settings characterized by differing angles of prism taper.

Site 1178 Summary

The science objective of Site 1178 included sampling of slope sediments and underlying LDRZ (Fig. F11) in order to clarify the structural evolution of the prism.

We recognized two fundamental lithostratigraphic units at Site 1178 (Figs. F8B, F30). Both are divided into three subunits. Interpretations of the lithostratigraphy are hampered by complexities in biostratigraphy and structural deformation. Subunit IA (upper slope–apron facies) is Quaternary to Pliocene in age and extends from the seafloor to a depth of 94.40 mbsf. Lithologies consist of hemipelagic mud, sandy mud, and volcanic ash. Subunit IB is Pliocene in age and extends from 94.40 to 127.00 mbsf. In addition to the normal hemipelagic mud, this subunit also contains abundant silt-sand turbidites, and minor mud-supported gravel. Subunit IC is Pliocene to late Miocene in age and extends from 127.00 to 199.20 mbsf. Lithologies in Subunit IC consist of hemipelagic mud with variable amounts of intermixed sand, rare volcanic ash beds, and rare mixed volcanic lapilli and gravel-sized mud clasts. Strata within Unit I have been subjected to significant amounts of displacement along a submarine slide surface. Below the dislocation surface, more highly deformed strata of Unit II are late Miocene in age and almost certainly part of the Nankai accretionary prism. Subunit IIA (411.00–199.20 mbsf) contains abundant sand and silt turbidites with interbeds of carbonate-poor mudstone. Similarities are striking between their lithofacies associations and those of the axial trench–wedge environment. Subunit IIB (411.00–563.95 mbsf) contains sporadic silt to sandy silt turbidites and a greater proportion of carbonate-poor mudstone, similar in all respects to the outer trench–wedge facies at Sites 1173 and 1174. The axial trench–wedge facies is repeated below 563.95 mbsf (Subunit IIC) and extends to the bottom of Hole 1178B. This repetition of facies confirms the occurrence of one of the imbricate thrust faults within the accretionary prism. The low carbonate content throughout Unit II indicates deposition below the CCD.

Structurally, Site 1178 consists of four domains. Domain I, from 0 to 200 mbsf, comprises the slope sediments, with discrete slump-folded packages and east-west–striking bedding. Domain II, from 200 to 400 mbsf, consists of accreted sediments but with only small-scale deformation features and gentle to moderate bedding dips. In contrast, Domain III extends from 400 to 506 mbsf and is characterized by marked deformation throughout (Figs. F31, F32, F33). The deformation has four chief elements: bedding dips ranging up to 55°, bedding-oblique foliation, bedding-parallel fissility (Fig. F31), and fracture sets that brecciate the sediment into roughly trapezoidal fragments and postdate the foliation/fissility. Toward the base of this 106-m zone of shearing, scaly surfaces with downdip slickenlines probably indicate a major prism thrust fault. Domain IV, from 506 mbsf to the base of the hole, is characterized by generally weaker deformation, although moderate bedding dips are common. Steeper dips and increased deformation around 550 mbsf and between 633 mbsf and the hole bottom presumably represent additional minor thrust faults. Thus Domain IV contains several thrust slices, each internally deformed much less than the sheet overlying the major thrust at the base of Domain III but probably contributing to biostratigraphic repetitions and thickening of the section.

Biostratigraphic age control was provided by calcareous nannofossils although their abundance and states of preservation varied throughout the sequence. The interval from 199.05 to 673.17 mbsf yields assem-

F30. Summary of results, Site 1178, p. 73.

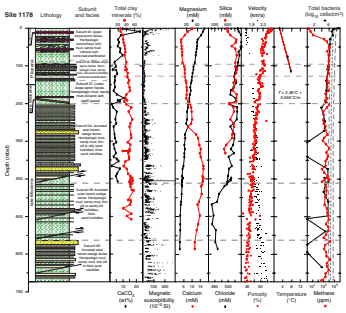

F31. Bedding oblique foliation, p. 74.

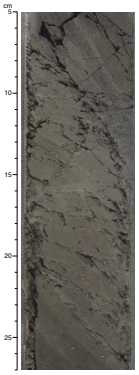

F32. Incipient weblike structure in fine sand, p. 75.

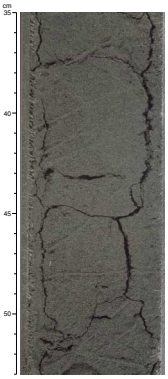

F33. Incipient scaly and foliated clays, p. 76.

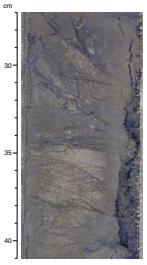

blages especially poor in preservation and low in abundance, making zonal identification problematic. Deformation of the sediments leads to a repetition of biostratigraphic events, resulting in a disturbed biostratigraphic secession. The sedimentary section spans the time interval from the late Miocene (Zones NN11–NN10) through the Pleistocene (Subzone NN21a).

Paleomagnetic measurements of magnetic inclination and intensity in Holes 1178A and 1178B show two hiatuses at 8.5 mbsf and ~400 mbsf. Based on the results of biostratigraphy, inclination changes from the top to the bottom of Holes 1178A and 1178B are identified as two different geomagnetic polarity intervals. Normal polarity is identified from 0 to 8.5 mbsf in Hole 1178A within the Brunhes Chron (0–0.78 Ma). Inclination changes from 8.5 to ~400 mbsf are considered to be geomagnetic polarity changes from Pliocene to late Miocene, including the Gauss (2.581–3.580 Ma), Gilbert (3.580–5.894 Ma), and C3A (5.894–6.935 Ma) Chrons. Continuous steep inclinations below 400 mbsf may be considered to be a repeat of the C4r Subchron (8.072–8.699 Ma).

The Cl concentration-depth profile exhibits a steep, continuous trend of freshening of up to 3%–4% relative to seawater Cl concentration. Superimposed on this background dilution profile are numerous smaller Cl minima. The largest ones occur at ~200 mbsf, corresponding to >6% dilution, and above the BSR at ~400 mbsf, corresponding to ~7% dilution. Based on measured core temperatures on the catwalk (a minimum of –0.5°C at 200 mbsf), the associated elevated methane concentration, and the observation that other dissolved components such as Si and Ca have similar dilution minima, we suggest that disseminated methane hydrate is widespread at this site, increasing in abundance from ~90 mbsf to the depth of the BSR. Hydrate is probably not evenly distributed within the sediment and seems more abundant in coarser-grained horizons.

The Ca, Mg, alkalinity, and sulfate concentration profiles are intimately coupled in the top 35 mbsf, with primary dolomite formation and dolomitization of biogenic calcite the most active reactions. The inverse relation between Ca and Mg below this depth suggests that they are involved in distinct reactions—Mg in silicate reactions below the depth drilled and Ca in ash dissolution and alteration plus probably carbonate reactions linked or associated with microbially mediated reactions at the BSR.

Similar to the deep-water Sites 1173 and 1174 but unlike the shallow water Sites 1175 and 1176, an increase in Cl concentration with depth in the top 35 mbsf is a trend consistent with diffusion of lower chlorinity interglacial water into the sediment.

The TOC content for the sediment samples examined at Site 1178 ranges from 0.57 to 1.03 wt% over the first 383.6 mbsf, with an average value of 0.73 wt%, the highest TOC values measured for Nankai sediments during Leg 190. Sulfur concentrations track the TOC values in this interval and range from 0.24 to 1.45 wt%, with the highest values occurring at 200 and 350 mbsf coincident with the highest TOC values. The moderate to low concentrations of methane throughout Holes 1178A and 1178B are attributed to the high concentrations of light hydrocarbons from ethane to hexane, indicative of older, more mature organic matter within the sediments (diagenesis) or migration (thermogenesis) of hydrocarbons from deeper depths. Overall, the concentrations of light hydrocarbon ethane to hexane reflect the thermal evolution and maturity of the sedimentary organic matter at Site 1178. The Bernard ratio ($C_1/[C_2+C_3]$) for the hydrocarbons at Site 1178 also in-

dicates that some contribution of the lighter hydrocarbons (ethane to hexane) in these sediments were produced from more mature organic matter present in situ mixed with thermogenic hydrocarbons that have migrated in from a more mature source at depth. Significant faulting has occurred over the lower 300 m of Hole 1178B that could facilitate fluid migration of more mature hydrocarbons buried at deeper depths to shallower sediments.

Microorganisms were enumerated in 30 samples collected from the surface to 633 mbsf at Site 1178. Bacteria are present in near-surface sediments at low, but close to expected abundances. This was probably related to high IW sulfate concentrations to at least 18.3 mbsf. However, bacterial populations decline rapidly to barely detectable at 272 mbsf. This is a much greater rate of decrease than was observed at other sites during this leg. A small but statistically significant decrease from the general trend that is associated with the presence of a small amount of gas hydrate occurs at 210 mbsf. Below 272 mbsf, population sizes generally vary between not detectable and barely detectable, except for a zone between 374 and 497 mbsf, where populations increased up to a maximum of 6×10^5 cells/cm^3. These populations were not only locally statistically significant but were larger than those encountered at some of the more shallow depths at this site. No relationship was observed between bacterial populations and either the IW sulfate concentration or the methane concentration; therefore, the reasons for such a rapid rate of decrease in numbers remains unclear. Seventeen whole-round cores were taken for shipboard enrichment cultures, cell viability, and shore-based microbiological analysis to measure potential bacterial activities, culture microorganisms, characterize nucleic acids, and investigate fatty acid biomarkers.

There are no obvious differences in physical properties between the slope-apron deposits of Unit I and the underlying accreted sediments of Unit II. In general, porosities at Site 1178 decrease with depth, following a typical compaction profile. Deviations from the compaction trend occur at 70–100 mbsf, 140–160 mbsf, and ~200 mbsf. In addition, porosity values within lithostratigraphic Subunits IB and IC are more scattered than in Subunit IA and Unit II, and they probably reflect lithologic variation in this sandier part of the stratigraphic section or deposition by slope-failure processes. Velocities and formation factors increase with depth and are highly variable. Uncalibrated gas permeability measurements show a range of values similar to other Leg 190 sites, again due to differences in lithology. High values are given by volcanic ashes high in the section and by beds of silt and sand, including those down to 600 mbsf. The background hemipelagites gave uniformly low measurements.

Two in situ temperature measurements indicate a thermal gradient of 0.046°C/m.

Site 1178 drilling revealed that the LDRZ is composed of steeply dipping, pervasively foliated, and partly brecciated upper Miocene accreted sediments. This result will contribute significantly to our understanding of the tectonic evolution of the Nankai accretionary prism.

SUMMARY OF SCIENTIFIC RESULTS

Stratigraphic Framework of Incoming Sediments

Results from Leg 190 help define several important spatial and temporal differences in the stratigraphy of the Shikoku Basin. In turn, these stratigraphic variations influence patterns of deformation within the Nankai Subduction System. Beginning at the stratigraphic base, a volcaniclastic-rich facies overlies basalt basement at Site 1177 (Ashizuri Transect) (Figs. **F8A, F10**). This facies differs from basal strata at Sites 808 and 1173 (Muroto Transect) in three important ways. First, the oldest strata at Site 1177 are early Miocene in age, rather than middle Miocene. Second, they contain considerable amounts of siliciclastic silt and sand in addition to volcanic sand and ash. Third, the hemipelagic mudstones contain higher percentages of smectite. The lower Miocene siliciclastic and volcaniclastic beds probably were eroded from the Japan Island arc and the Kyushu-Palau remnant arc. The age variation in basal sediment from west to east can be explained by proximity to the axis of the spreading ridge of Shikoku Basin. The ridge was active between 26 and 15 Ma, and seamount eruptions along the Kinan chain may have continued to 13–12 Ma. Temporal correlation of the Miocene ash beds remains uncertain. Given the existing biostratigraphic resolution, volcaniclastic beds along the Ashizuri Transect appear to be older than the thick rhyolitic tuff deposits that were cored at Site 808, so they may have been erupted from a different source.

Cores from Site 1177 include a package of lower(?) to upper Miocene siliciclastic turbidites with abundant woody organic matter. Hemipelagic mudstone interbeds are enriched locally in expandable clay minerals. Deposition of correlative turbidites at DSDP Site 297 also began during the Miocene but continued into the Pliocene. The Miocene turbidites at Site 1177 were derived from a relatively large land mass, most likely southern Japan, and the dispersal system spread terrigenous sediment over a broad area of Shikoku Basin. During that same time interval, the seaward part of the Muroto Transect area sat above the basement high formed by the Kinan Seamounts. Higher seafloor relief evidently prevented the upslope deposition of turbidites.

Fine-grained hemipelagic deposits of Shikoku Basin display an unexpected characteristic of unusually high magnetic susceptibility. Magnetic susceptibility increases even within mudstone intervals between the Miocene turbidite packets at Site 1177. The mineralogic cause of this magnetic response in Shikoku Basin strata remains unknown.

A facies change from the lower to upper Shikoku Basin is defined at all sites by the absence to presence of ash beds containing recognizable volcanic glass shards. Most of the Pliocene volcanic ash beds probably were derived from the Honshu-Kyushu arc. Particle size, chemical composition, temperature, depth of burial, and time affect ash alteration and preservation. Thus, this unit boundary is time transgressive and sensitive to regional and temporal changes in the margin's thermal structure.

Shikoku Basin strata experienced diachronous burial during the Pliocene and Quaternary beneath an upward-coarsening and upward-thickening wedge of trench turbidites. The Nankai Trench wedge is thinner in the Muroto Transect area (above the basement high), but individual turbidites tend to be thinner and finer grained toward the southwest (DSDP Site 582). Quaternary sedimentation rates at Sites 1173 and 1174 were 600 and 760 m/m.y., respectively, more than one

order of magnitude higher than the rate for Miocene turbidites at Site 1177 (35.5 m/m.y.). The main reasons for the higher rates of trench sedimentation include erosion from rapidly uplifting volcanic and metasedimentary terranes in the Honshu-Izu collision zone of central Japan and confinement of most sediment gravity flows to an axial dispersal system.

Evolution of the Accretionary Prism

Sites 1175, 1176 and 1178 are among a handful of DSDP and ODP sites to have penetrated completely through slope sediments into an underlying accretionary prism (Figs. **F8B, F11**). They are, therefore, important for refining models of trench-slope evolution. The upper facies unit at all three sites fits into conceptual models of a trench-slope basin or slope apron, at least for locations in isolation from influx of coarse terrigenous sediment. Resedimentation of muddy material by submarine slumps and mudflows, perhaps triggered by seismogenic activity, contributed to high rates of sedimentation (200–3000 m/m.y.).

One of the unexpected discoveries of Leg 190 is the lack of change in lithofacies across the interpreted contact between trench-slope basin and accretionary prism, as deduced from seismic reflection data. Carbonate content within the inferred accretionary prism is depleted relative to slope sediments, which is consistent with deposition of trench sediment below the CCD. Strata throughout the slope to prism transition at Sites 1175 and 1176 include abundant sand turbidites and muddy gravel. One way to explain this paradox would be through frontal offscraping of a trench fan that had been fed by a transverse sediment conduit (e.g., throughgoing submarine canyon). Evidently, coarse siliciclastic material was diverted away from the slope basin relatively early in its development, as canyons were rerouted upslope by uplift and tilting of the prism. This change in the sediment-dispersal network resulted in an overall upward-thinning and upward-fining megasequence within the slope basin. Regardless of the ambiguity in the exact position of its basal unconformity, the slope basin at Sites 1175 and 1176 must have developed within the last 2 m.y. This is a major revision to previous estimates of the accretionary wedge growth and shows that the outer 40 km of the accretionary prism has been added to the Nankai margin over only 2 m.y. This finding has important ramifications for structural and hydrologic models of this margin.

Interpretations of results from Site 1178 are also complicated by biostratigraphy and structural deformation. A fundamental lithotectonic boundary exists between a mud-dominated slope apron and sandy accretionary prism at a major facies break (~200 mbsf). This contact is probably a slump surface. The underlying prism strata probably were accreted starting in the late Miocene, prior to the frontal accretion at Sites 1175 and 1176. It is clear that strata below 200 mbsf display many effects of intense deformation (e.g., fractures, incipient cleavage, and steeply dipping beds). Their facies character also matches that of the axial trench wedge and the outer trench wedge, and there is good sedimentologic evidence for thrust repetition of the axial trench-wedge facies, with slices at 199–411 mbsf and below 564 mbsf. These distinguishing features of both sedimentology and structural geology have important implications for interpretation of kindred rock units in such ancient subduction complexes as the Shimanto Belt of southwest Japan.

Chronostratigraphic Synthesis

Detailed bio- and magnetostratigraphic records were obtained at all sites to aid in correlation between sites. Paleomagnetic results for Site 1173 and 1174 show clear geomagnetic changes from the middle Miocene to Pleistocene (Fig. F34) and can be correlated with the polarity changes at Site 808. The basal age of the trench-wedge turbidites including the transition zone to the upper Shikoku Basin facies is estimated to be ~0.8 Ma. The boundary between the upper and lower Shikoku Basin at Sites 1173 and 1174 is interpreted to be 3–5 Ma. The age of the décollement zone at Site 1174 is estimated to be from 5.894 Ma (beginning of C3A Chron) to 6.935 Ma (termination of C3B Chron, which corresponds to the age of décollement zone at Site 808). At Site 1177 located in the Ashizuri Transect, the lower Shikoku Basin facies extends from the Pliocene to early Miocene, although it is difficult to identify the geomagnetic records because of poor core recovery (Fig. F34). Because Site 1177 was drilled without coring to 300.2 mbsf, correlations could not be made between Site 1177 and Site 582.

Pleistocene to Pliocene paleomagnetic data are similar at Sites 1175 and 1176 and document a few geomagnetic excursions within the Brunhes Chron.

At Sites 1173, 1174, 1177, and 808, the trench-wedge turbidites and the Shikoku Basin show contrasting sedimentation rates in the age-depth plots (Fig. F35). The sedimentation rates of the trench turbidites within the transition zone of each site shows high values, with the highest at Site 808 (204 m/m.y. at Site 1173, 698 m/m.y. at Site 1174, and 842 m/m.y. at Site 808). In contrast, sedimentation rates are slower in the upper and lower Shikoku Basin facies. Rates for the upper Shikoku Basin facies are 77.82 m/m.y. at Site 1173, 78.46 m/m.y. at Site 1174, and 81.62 m/m.y. at Site 808. The sedimentation rate of the upper Shikoku Basin facies at Site 1177, however, is lower (40.37 m/m.y.). Sedimentation rates for the lower Shikoku Basin facies are lower than those of the upper Shikoku Basin facies. The lower Shikoku Basin facies rates are 27.40 m/m.y. at Site 1173, 35.22 m/m.y. at Site 1174, 28.27 m/m.y. at Site 1177, and 31.67 m/m.y. at Site 808.

Magnetic susceptibilities proved a valuable tool for correlation among sites (Fig. F8A) and helped constrain the correlation of the décollement and incipient décollement horizons at Sites 1173, 1174, 808, and 1177.

Development of the Décollement Zone, Muroto Transect

Leg 190 completed a transect of the basal décollement of the Nankai accretionary prism from an undeformed state at Site 1173 to the well-developed fault zone landward of the deformation front documented at Sites 1174 and 808 (Fig. F36).

At Site 1173, there is little evidence from the structural geology or physical properties for a protodécollement zone (i.e., incipient deformation indicative of a major fault). The stratigraphic equivalent to the Site 1174 décollement interval indicated in Figure F36 is based on correlation of core magnetic susceptibility (Fig. F8). This interval is part of a thicker domain of increased bedding dip but shows no localized increase in observed deformation. However, a marked downhole decrease in *P*-wave velocity and a slight porosity increase at the top of the interval (~389 mbsf) suggest that a subtle mechanical strength discontinuity

F34. Biostratigraphic and magnetostratigraphic correlation, p. 77.

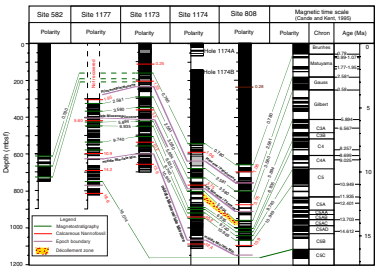

F35. Age-depth plots based on biostratigraphic and paleomagnetic data, p. 78.

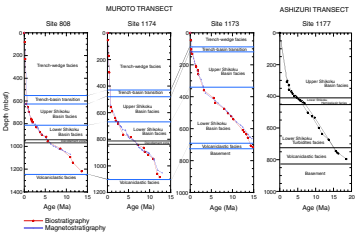

F36. Comparison of the structurally identified décollement interval, p. 79.

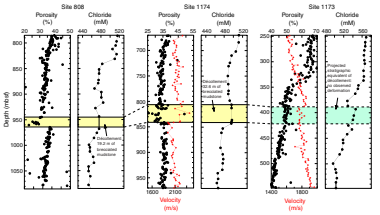

could contribute to the localization of the décollement in this interval. Pore fluid chlorinity also shows a small low-chloride excursion above this interval and an abrupt transition to higher values at ~390 mbsf; however, there is no corresponding feature in the Sites 1174 or 808 chlorinity data. It is unknown, of course, whether in the future the décollement actually will propagate along this particular stratigraphic horizon to the position of Site 1173.

The hallmark of the décollement zone at Sites 808 and 1174 is intense brittle deformation, manifested as finely spaced fracturing that breaks the mudstone into millimeter- to centimeter-scale fragments (Fig. F19). The fragments have polished and slickenlined surfaces, showing complex and heterogeneous slip directions, but they do not exhibit obvious internal deformational structures at the core scale. At Site 1174, the upper limit of the décollement zone is marked by a sharp downward increase in the intensity of brecciation, although the lowermost prism section above exhibits distributed fracturing as well. Within the décollement zone, there is a downward increase in intensity of the brecciation, peaking in a 7-m-thick zone of fine comminution of the mudstone just above the very sharp base of the décollement zone (Fig. F20). Within the fault zone are several intervals up to tens of centimeters thick of unbroken mudstone, which are interpreted as intact blocks in a multistranded shear zone.

It is remarkable that the décollement zone at Site 1174 appears to be at least as well developed as it is at Site 808. It is thicker at Site 1174 than it is at Site 808 (32.6 vs. 19.2 m thick, respectively). It is also brecciated to a finer scale, despite the more landward—thus presumably more structurally evolved—position of Site 808. Differences in the observed structures could be explained by differences in core recovery; however, the greater thickness at Site 1174 could not. Notable at both sites is the complete absence of veins, alteration zones, or other evidence of past fluid-rock interaction specific to the décollement.

The development of the décollement and the strain discontinuity across it are clearly exhibited in the core physical properties data. At Site 1174, there is a sharp porosity increase and *P*-wave velocity decrease immediately below the structurally defined décollement. These same features are even more pronounced at Site 808. Site 808 exhibits evidence of a porosity minimum within the décollement, whereas no clear evidence for such a minimum exists at Site 1174. However, the most prominent feature at both sites is the discontinuity across the base of the zone crossing into the underthrust section. This discontinuity is likely due to a combination of undercompaction of the rapidly loaded underthrust section (e.g., Saffer et al., 2000) and enhanced tectonic compaction of the prism and décollement caused by the imposition of lateral tectonic stress (Morgan and Karig, 1995a).

In summary, the décollement beneath the toe of the Nankai accretionary prism develops from an unremarkable and homogeneous interval of hemipelagic mudstone into a 20- to 32-m-thick zone of intense brittle deformation, the base of which marks a boundary between the distinct physical/mechanical regimes of the prism and the underthrust section. The two drilling penetrations of the fault zone suggest an anastomosing system of discrete brittle shears similar to faults observed in mudrocks on land. Despite a major effort to detect localized fluid flow along the fault, there is no unambiguous evidence for flow of a chemically distinct fluid in the décollement zone along the transect defined by these three sites.

Correlation of the décollement horizon between Muroto and Ashizuri Transects imposes an intriguing question on the localization of the décollement in the lower Shikoku Basin mudstone. Although DSDP/ODP drilling has not penetrated the décollement at the Ashizuri Transect, a clear and continuous seismic reflector allows us to correlate the décollement horizon at the toe region with Site 1177 (Fig. F37). At Site 1177 this reflector is at 420 mbsf and coincides with the identical horizon of the décollement of the Muroto Transect based on chronological and magnetic susceptibility correlations. This raises the important question of why the décollement stays at the same stratigraphic horizon despite a major difference in the thickness of turbidites and the lithology and diagenesis of the Shikoku Basin sediments between the two transects. This question should be addressed by further shore-based study.

F37. Structural and stratigraphic interpretation of seismic profile, p. 80.

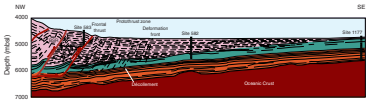

Geochemical Gradients, Muroto Transect

The shipboard geochemical data provide insight on the origin of fluids and the depth intervals and paths of possible recent fluid flow. In addition, abiogenic and microbially mediated diagenetic reactions that have modified fluid composition have been characterized and quantified.

The most interesting and pronounced feature of the pore fluid concentration-depth profiles in the Muroto Transect from Site 1173 through Site 1174 to Site 808 is the ~350-m-thick low-Cl zone within the lower Shikoku Basin unit (Fig. F38). It has a clear concentration minimum ~140 m below the décollement (or its equivalent at Site 1173). At Sites 1173 and 1174, this low-Cl zone decreases in intensity gradually upsection to the sediments overlying the upper Shikoku Basin facies. Additionally, the extent of Cl dilution relative to seawater Cl concentration systematically differs among the sites; it has evolved from 8%–9% at reference Site 1173 to 16%–17% at intermediate Site 1174 to 20%–21% at adjacent (<2 km) Site 808. Based on the residual smectite content of the sediment section at Site 808, some of the freshening may not be due to local smectite dehydration but could result from transport of freshened fluids from greater depth. It is important to note, however, that the original smectite concentration and clay-sized fraction are not known. The low-Cl concentrations most likely reflect some combination of (1) in situ clay dehydration and other reactions, (2) the transport of freshened water from dehydration reactions at greater depth, and (3) the uptake of Cl by deep-seated hydrous silicate reactions; for example, serpentine, chlorite, talc, or amphibole incorporate considerable amounts of Cl in their structure. These reactions occur at temperatures of >250° up to ~450°C. Thus, the broad low-Cl zone possibly carries a signal from Cl uptake by high-temperature reactions in the seismogenic zone. The relative contributions of these processes can be resolved by rigorous mass-balance calculations, modeling of the physical and chemical hydrology, shore-based measurements of Cl, Br, and F concentration, and Cl and Br isotope analyses.

F38. Chloride concentrations in interstitial water samples, p. 81.

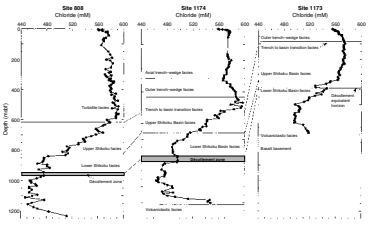

The most interesting and pronounced feature of the pore fluid concentration-depth profiles in the Muroto Transect from Site 1173 through Site 1174 to Site 808 is the ~350-m-thick low-Cl zone within the lower Shikoku Basin unit (Fig. F38). It has a clear concentration minimum ~140 m below the décollement (or its equivalent at Site 1173). At Sites 1173 and 1174, this low-Cl zone decreases in intensity gradually upsection to the sediments overlying the upper Shikoku Basin facies. Additionally, the extent of Cl dilution relative to seawater Cl concentration systematically differs among the sites; it has evolved from 8%–9% at reference Site 1173 to 16%–17% at intermediate Site 1174 to 20%–21% at adjacent (<2 km) Site 808. Based on the residual smectite content of the sediment section at Site 808, some of the freshening may not be due to local smectite dehydration but could result from transport of freshened fluids from greater depth. It is important to note, however, that the original smectite concentration and clay-sized fraction are not known. The low-Cl concentrations most likely reflect some combination of (1) in situ clay dehydration and other reactions, (2) the transport of freshened water from dehydration reactions at greater depth, and (3) the uptake of Cl by deep-seated hydrous silicate reactions; for example, serpentine, chlorite, talc, or amphibole incorporate considerable amounts of Cl in their structure. These reactions occur at temperatures of >250° up to ~450°C. Thus, the broad low-Cl zone possibly carries a signal from Cl uptake by high-temperature reactions in the seismogenic zone. The relative contributions of these processes can be resolved by rigorous mass-balance calculations, modeling of the physical and chemical hydrology, shore-based measurements of Cl, Br, and F concentration, and Cl and Br isotope analyses.

The origin of slightly higher Cl concentration within the décollement zone observed at Sites 1174 and 808 is unclear.

Other potential fluid flow horizons characterized by sharp changes in downnhole geochemical profiles are

1. At Sites 1173, 1174, and 808, the boundary between the trench-wedge and upper Shikoku Basin sediments. The sharp reversal of

the Cl gradient at this boundary may be maintained by flow of a slightly more saline fluid than seawater or by in situ hydration reactions that outpace diffusion.
2. Along the protothrust (~470 mbsf) at Site 1174, as particularly indicated by the Cl, Na, Ca, and K concentration profiles.
3. At Site 1176, as indicated by the Cl, Na, Ca, and K concentration profiles, which suggest communication with a deep fluid source, possibly associated with the OOST.

It is interesting to note that the chemical characteristics of fluids from the protothrust at Site 1174 and the source potentially associated with the OOST fault at Site 1176 are similar to the characteristics of the fluid in the low-Cl zone centered below the décollement. The composition of the fluid along the trench wedge/Shikoku Basin boundary is, however, distinct.

Another distinct characteristic of the Muroto Nankai Transect, not observed at any of the other drilled DSDP and ODP subduction zone sites, is the elevated (up to 10 mM) dissolved sulfate zone found at depth. It is beneath the near-surface sulfate reduction zone, and prevails from the boundary between the upper and lower Shikoku Basin facies to the oceanic basement and probably deeper. The fact that microbial activity has not reduced the dissloved sulfate zone over the past 0.5 m.y. indicates that the amount of labile organic matter available for microbial activity (for sulfate reducers and/or methane oxidizers) above the proto-décollement and décollement zones, where temperatures do not limit bacterial activity, is extremely low. Dissolved sulfate can only be reduced inorganically at temperatures of 250°–300°C, and thus may persist into the seismogenic zone. The presence of dissolved sulfate in an anaerobic environment affects the oxidation state of the system and should influence sediment magnetic properties as well as inorganic reactions with transition metals, such as Fe and Mn.

The dominant diagenetic processes are ash alteration to clays and zeolites and silicate (mostly clay) reactions at the deep water sites and carbonate reactions at the shallow water sites; carbonate diagenesis, however, also occurs at the deep water sites. Opal-A dissolution controls the Si concentration profiles at each of the sites in the top few hundreds of meters, and other silicate reactions control it deeper in the sections.

Gas Hydrates

Although no solid gas hydrate was recovered during Leg 190, their presence was documented indirectly. Both temperature measurements of cores on the catwalk and pore fluid Cl concentrations indicate the existence of gas hydrates at two slope sites, Site 1176 and Site 1178. Gas hydrate dissociates upon recovery because it is unstable at ambient temperature and pressure. Recovery of solid hydrate is unlikely unless it is extremely abundant.

Sites 1176 and 1178 are within the stability field of seawater-methane hydrate from the seafloor to the BSR. Because methane is the dominant gas in the sediments at these sites, any gas hydrate present should be primarily methane hydrate, as it is found at nonthermogenic oceanic sites. Formation of methane hydrate is a highly exothermic reaction; its decomposition consumes much heat and cools the cores. At Site 1176, temperatures 4°–5°C colder than background temperatures between ~220 and 240 mbsf were measured in two cores (190-1176A-25X and 26X). Because of poor core recovery no data exist between 240

and 320 mbsf. Pore fluid Cl concentrations suggest minor dilution of Cl by ~1% beyond dilution by other processes.

At Site 1178, gas hydrate appears to be considerably more abundant. Based on pore fluid Cl concentrations, methane hydrate (inferred from gas composition) is present between ~120 and 400 mbsf, with the highest concentrations between 150 and 200 mbsf. The lowest catwalk core temperature of –0.5°C was measured at ~200 mbsf in Core 190-1178A-23X. Temperatures colder than background by 4°–6°C were measured in several cores, mostly between 150 and 200 mbsf.

At Site 1178, the Cl concentration-depth profile has a steep, continuous trend of freshening between 90 and 200 mbsf with two intense Cl minima. The first is between 170 and 185 mbsf. The second minimum with the lowest Cl value of 524 mM compared with that of bottom-water value of 557 mM was measured in Core 190-1178A-23X, which also had the –0.5°C catwalk temperature. This corresponds to >6% dilution by methane hydrate decomposition. The background dilution throughout the 150–200 mbsf interval is 3%. Between 200 and 400 mbsf, Cl concentrations continue to gradually decrease with depth from 545 mM to a minimum of 517 mM at the BSR depth (~420 mbsf), which corresponds with >7% dilution. Superimposed on the background Cl dilution profile are numerous smaller Cl minima. This suggests that throughout the section, from 90 to 400 mbsf, disseminated gas hydrate is present and is responsible for the background 3%–4% Cl dilution and that specific sediment horizons, probably the coarsest grained ones, have higher hydrate concentration, equivalent to 6%–7% Cl dilution.

Cl concentrations sharply decrease below the BSR depth and reach a minimum of 470 mM, almost a 6% dilution, centered around 500 mbsf. The origin of this low-Cl zone is as yet unclear. It may represent a more hydrate-rich young paleo-BSR, which has not had enough time to diffuse. Higher concentrations of methane at this depth are consistent with this hypothesis.

Changes in Physical Properties

Trench-Wedge Facies

The trench-wedge facies thickens substantially from the basin to the trench. This rapid sedimentation may affect the pore pressures and the compaction state of the underlying sediment. Within the trench-wedge facies, porosities exhibit high scatter, probably because of lithologic variability. In general, porosities decrease with depth within this section at Sites 1173 and 1174 but show no distinct trend at Site 808. Some of the difference in the porosity trend may be attributed to offset along the frontal thrust at Site 808, which would disturb the pre-existing porosity profile.

Upper Shikoku Basin Facies

At Site 1177, the lowermost ~100 m of the upper Shikoku Basin facies exhibits nearly constant porosities of 60%–65%, whereas the *P*-wave velocities increase slightly with depth (Fig. F39). At Site 1173, porosities increase slightly with depth from 57%–65% at ~102 mbsf to 62%–69% at ~340 mbsf. These values are surprisingly high for a burial depth of 300–400 m, and the porosity within the upper Shikoku Basin facies at both reference sites deviates significantly from normal compaction

F39. Porosities and velocities across Sites 1173, 1174, 808, and 1177, p. 82.

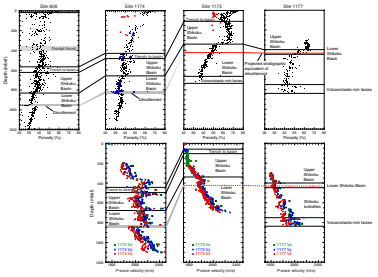

trends for silty clays. Velocities at Site 1173 remain relatively constant to ~240 mbsf and increase below this, despite the increasing porosity. This behavior suggests cementation. At Sites 808 and 1174, a slight porosity increase with depth is observed in this unit but is less distinct than at Site 1173. Porosities within the upper Shikoku Basin facies at Sites 1174 and 808 range from ~35% to 45%. The difference in porosity values between the reference sites and those in the deformed wedge imply that either compaction, collapse, and dewatering of the sediments has occurred during accretion or the sites within the accretionary wedge have a different diagenetic, cementation, and burial history than the current reference sites. High-velocity layers occur near the top and bottom of the upper Shikoku Basin facies, which is otherwise characterized by gradually increasing velocities with depth.

Lower Shikoku Basin Facies

Along the Muroto Transect (Sites 1173, 1174, and 808), porosities within the lower Shikoku Basin facies decrease with depth and follow a compaction trend typical of fine-grained marine sediments. At Site 1173, porosities within this unit decrease from ~50% at the top to ~36% at its base. At Sites 1174 and 808, porosities decrease from 34%–40% to 30%–35%, with a sharp offset to greater porosity across the décollement. At Site 1177, the lower Shikoku Basin facies includes a thick turbidite sequence that does not correlate with the stratigraphy observed along the Muroto Transect. Porosities within the upper hemipelagic portion of the lower Shikoku Basin facies at Site 1177 (400–449 mbsf) decrease with depth from 60%–65% to 46%–54%. The porosity decrease within the lower Shikoku Basin sequence from Site 1173 to Sites 1174 and 808 may be explained by compaction and dewatering of these sediments with progressive burial. Alternatively, the lower Shikoku Basin sediments at Sites 1174 and 808 may have initially had lower porosities than Site 1173 because of factors such as greater overburden or lithologic differences.

At Sites 808 and 1174, porosities increase sharply across the décollement zone, whereas velocities decrease. This probably reflects a combination of (1) rapid, partially undrained burial of the underthrust sequence resulting in underconsolidation and (2) higher mean stress and tectonic compaction of the accreted sediments. At Site 1174, porosities directly below the décollement zone are slightly lower than at Site 808. This observation suggests that simple progressive compaction of underthrust sediments may not adequately explain the porosity-depth trends and that other factors (such as initial sediment thickness and heterogeneity in mechanical strength) are also important. At Site 1173 the stratigraphic equivalent interval of the décollement zone (~390–420 mbsf) corresponds to the base of an anomalous zone in which velocities decrease with depth. A similar, considerably smaller amplitude velocity excursion correlates with the stratigraphic equivalent of the décollement at Site 1177 (~430 mbsf).

In accordance with the steadily decreasing porosities below the décollement zone, velocities generally increase with depth at Sites 808 and 1174. Horizontal velocities (V_x and V_y) increase more rapidly with depth below the décollement than vertical velocities (V_z). Increasing velocity anisotropy with depth suggests vertical compaction of the sediments.

Mass Accumulation Rates

Comparison of the thickness of lithostratigraphic units between sites appeared problematic because of the apparent diachronism of the lithostratigraphic boundaries and the lateral changes in porosity. To address this problem, we computed solid thicknesses for each unit. The solid thickness is computed by integrating the solid volume fraction (1-porosity) upward from the base of the sedimentary column using the moisture and density data. By comparing solid thickness of stratigraphic units between sites, we can account for differences in consolidation history. The solid thickness is preserved during vertical compaction but is increased by horizontal tectonic shortening, regardless of whether it occurs by ductile strain or by thrusting. Figure **F40** shows the biostratigraphic and paleomagnetic ages at Sites 808, 1174, 1173, and 1177 as a function of the solid thickness. The derivative of these curves represents the solid mass accumulation rate.

The diachronism of the lithostratigraphic boundaries appears clearly on Figure **F40.** The upper/lower Shikoku Basin facies boundary occurs at ~2.25 Ma at Site 1174, ~3 Ma at Site 1173, and >4 Ma at Site 1177. The base of the trench wedge is younger at Site 1173 than at Sites 808 and 1174.

The solid thickness of the sequence below the stratigraphic level of the décollement displays some lateral variability, which could be attributed to lateral variations in mass accumulation rates during sedimentation. This variability is most important in the part of the basin older than 11 Ma. Accumulation rates obtained by linear regression on all age data between 7 and 11 Ma are comparable at all sites: 14.9 m/m.y. at Site 1173, 16 m/m.y. at Site 1174, 13.7 m/m.y. at Site 808, and 16.3 m/m.y. at Site 1177. The same is true of accumulation rates between 1.8 Ma (Pliocene/Pleistocene boundary) and 4 Ma: 29.7 m/m.y. at Site 808, 29.9 m/m.y. at Site 1174, 28 m/m.y. at Site 1173, and 22 m/m.y. (based on paleomagnetism) at Site 1177. In contrast to these two sequences, the interval immediately surrounding the décollement varies considerably in thickness. The solid thickness of the 4- to 7-Ma interval increases from ~15 m at Site 1173 to ~30 m at Site 1174, and to 35 m at Site 808. Note that the décollement varies in stratigraphic age by ~1 m.y. between Site 808 and Site 1174 but stays within the lower part of this thickened interval. Note that the décollement on the Ashizuri Transect also lies within the same age interval. It appears that throw on the frontal thrust (150 m, corresponding to 80 m of solid thickness where it was drilled) accounts for the change of thickness of the trench wedge between Site 808 and Site 1174.

F40. Biostratigraphic and paleomagnetic ages as a function of solid thickness, p. 84.

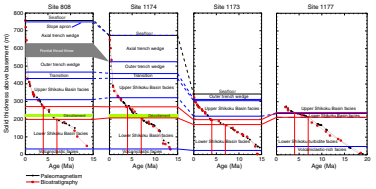

ORGANIC GEOCHEMISTRY AND HYDROCARBON SOURCES

Multiple sources (biogenic, thermogenic, and catagenic) and production mechanisms for the hydrocarbons encountered during Leg 190 were identified by plotting the methane, Bernard ratios ($C_1/[C_2+C_3]$), and sulfate profiles for each Site (Fig. **F41**). At Reference Site 1173, the hydrocarbon profile is dominated by biogenic methane down to 260 mbsf, followed by a shift to a mixture of thermally produced methane and lighter hydrocarbons around 300 mbsf that dominates the composition of gases down to 724 mbsf. The marked shift in hydrocarbon type is likely due to an increase in sulfate concentration below ~400 mbsf

F41. Interpretation of hydrocarbon sources encountered, p. 85.

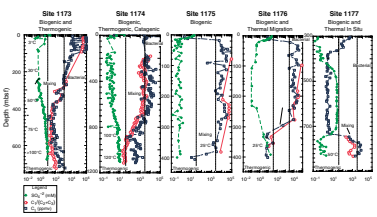

that inhibits biogenic production of methane. The hydrocarbons detected in sediments at Site 1174 are indicative of mixing between biogenic and thermogenic sources down to ~850 mbsf, with the thermogenic component increasing in concentration with temperature and depth. Like Site 1173, as sulfate increases with depth, methane production decreases (low parts per million). The hydrocarbons below ~850 mbsf are the products of both rapid thermal maturation of immature organic matter present in the sediments (thermogenic) and the thermal cracking of more mature organic matter or "kerogen" (catagenic).

Site 1175 is characterized by very young sediments and immature organic matter as observed by the production of biogenic methane throughout the hole. As at Site 1175, biogenic methane dominates the first 300 mbsf of Hole 1176A; however, over the last 100 m there is an abrupt shift into the thermogenic zone. Interestingly, the $C_1/(C_2+C_3)$ ratio indicates that no mixing has occurred; therefore, the hydrocarbons detected below 300 mbsf are a separate component. The very low thermal gradient at Site 1176 (~25°C at total depth; 401.6 mbsf) coupled with high sulfate concentrations and the predominance of C_2 over C_1 indicate that thermogenic hydrocarbons migrated into the lower 100 m of Hole 1176 from a deeper source rather than forming in situ by diagenesis at low temperature. The hydrocarbon profile for Site 1177, drilled on the Ashizuri Transect, differs significantly from those sites drilled on the Muroto Transect, with low concentrations of methane between 304 and 363 mbsf followed by an abrupt drop in methane concentration (a few parts per million) over the next 270 m of hole. The low abundance of methane below 400 mbsf is the result of an unusually high sulfate content that is controlling methanogenesis or microbial mediation of methane production. The relatively low concentrations of organic matter available in these sediments may be preventing sulfate reducers from consuming the excess sulfate, keeping concentrations at high levels. A sharp increase from the low parts per million level to ~1600 ppm was measured in the last 90 m to total depth at 830.3 m, coincident with the transition from the Shikoku turbidite facies (Unit III) to the volcaniclastic facies (Unit IV). As at Site 1176, there is an abrupt shift of the $C_1/(C_2+C_3)$ ratio to the mixing zone with both ethane and biogenic methane occurring between 750 and 830 mbsf. The temperatures within the mixing zone at Site 1177 are in the range of thermogenic in situ production of the C_2 lighter hydrocarbons.

Microbial Activity and Biogeochemistry

Through their metabolic activity, bacteria are responsible for shaping many of the chemical profiles within deep marine sediments. The distribution of the microbial community was characterized and their impact on deep marine sediments was investigated in cores from the Nankai Trough (Fig. **F42**). The apparent environmental controls on bacterial distribution varied among sites from physical (temperature) to geochemical. Overall, the total numbers of bacteria at these sites was either at the low end or below the range predicted by a general model constructed from bacterial distributions in deep marine sediments at previous ODP sites (Parkes et al., 1994). This is consistent with observations made at a previous accretionary prism site—Cascadia margin.

The abundance of bacteria at Site 1173 appears to be primarily controlled by a steep thermal gradient. The profile agrees with the model

F42. Biogeochemical profiles in sediments, p. 86.

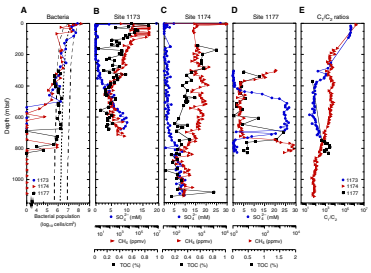

for the upper 250 m, with a significant increase in numbers between 43 and 80 mbsf associated with high concentrations of methane and TOC. At 250 and 460 mbsf the temperature boundaries for mesophiles/thermophiles and thermophiles/hyperthermophiles, respectively, were crossed. At the upper boundary populations decreased overall, and at the second boundary there was a single significant increase at ~85°C. Bacteria were not observed in the five deeper, and warmer, samples at this site (536–673 mbsf). Overprinting this temperature control is a significant correlation between bacterial numbers and in situ methane concentration between the near surface below the sulfate reduction zone and ~400 mbsf. At 400 mbsf (~76°C), rising concentrations of both methane and sulfate suggest that bacteria are no longer controlling sediment geochemistry and that temperature effects dominate.

Bacterial abundance at Site 1174 falls within predicted values from the surface to ~370 mbsf, apart from two significant excursions in the upper layers associated with sandy cores. This site is also characterized by a steep temperature gradient, and at 370 mbsf estimated temperature is ~50°C. From this depth, bacterial populations rapidly decline to not detectable at 575 mbsf. Bacteria were not observed in the 15 samples collected from 623 to 1091 mbsf with the exception of two samples (779 and 796 mbsf) located just above the décollement zone. At these depths, with an estimated temperature of 90°C, bacterial abundance reappears within the envelope predicted by the model. Bacterial populations were not correlated with any of the in situ chemistry investigated and appear to be regulated solely by temperature at this site.

At Site 1177 bacterial abundance appears to be determined by sulfate. Coring began at 300 mbsf, where bacterial abundance was relatively low and remained so until 380 mbsf. Abundance in deeper samples (380–675 mbsf) steadily increased and was within predicted values from below 400 mbsf. This increase in bacterial numbers strongly correlated with increases in IW sulfate concentration that were unexpectedly present at near-seawater concentrations between 400 and 700 mbsf. Bacteria were also present at lower and decreasing concentrations between 725 and 811 mbsf despite methane concentrations increasing significantly below 740 mbsf. Overall low bacterial populations and high sulfate concentrations are probably attributable to very low TOC concentrations restricting bacterial sulfate reduction. Why populations do not react to increasing concentrations of methane below 740 mbsf remains unclear as the temperature gradient at this site was shallow with the hole estimated at <40°C throughout.

CONCLUSIONS

During Leg 190, we successfully cored six sites, meeting most of the leg objectives and also revealing some surprising new findings. Lithostratigraphy and sediment diagenesis vary markedly in three dimensions throughout the Nankai-Shikoku Basin system. These variations in turn exert considerable influence on physical properties, hydrology, fluid-sediment geochemistry, and microbial activity. Discontinuities in porosity, *P*-wave velocity, electrical conductivity, and grain density generally correspond to lithologic and diagenetic boundaries.

We demonstrated that there is a large contrast among many key properties, including the diagenetic, lithologic, and geochemical (including microbial activity) character of the incoming sequences, between the Muroto and Ashizuri Transects. Such contrasts may be tied to

variations in mechanical, structural, and hydrologic behavior along the strike of this margin. In spite of these contrasts, we found that the décollement at both transects occurs at the level of an almost coeval horizon (6–7 Ma). As at Site 808, the décollement marks an abrupt increase in porosity (and a corresponding decrease in *P*-wave velocity), suggesting some combination of undercompaction below and overcompaction above.

A broad low-chloride pore-water anomaly was found in the lower section of the incoming, as well as accreted, sediments along the Muroto Transect, as first identified at Site 808. The progressive decrease in the magnitude of the low-chloride anomaly from prism to basin indicates an important role of in situ diagenetic dehydration reaction and possible fluid migration process.

We also documented the accretionary history of the Nankai Trough prism for the first time and revealed a phenomenally rapid rate of growth of the prism during the Pleistocene. Our results will provide a basic framework for further mechanical, hydrogeological, and geochemical studies of this accretionary prism. Leg 190 results will also be useful for understanding the tectonics of accretionary prism evolution, thus providing a link between prism-toe processes and highly deformed accretionary complexes, the dominant components of orogenic belts.

REFERENCES

Aoike, K., 1999. Tectonic evolution of the Izu collision zone. *Res. Rep. Kanagawa Prefectural Mus. Nat. Hist.,* 9:113–151. (in Japanese)

Aoki, Y., Tamano, T., and Kato, S., 1982. Detailed structure of the Nankai Trough from migrated seismic sections. *In* Watkins, J.S., and Drake, C.L. (Eds.), *Studies in Continental Margin Geology.* AAPG Mem., 34:309–322.

Ando, M., 1975. Source mechanisms and tectonic significance of historical earthquakes along the Nankai Trough, Japan. *Tectonophysics,* 27:119–140.

————, 1991. A fault model of the 1946 Nankaido earthquake derived from tsunami data. *Phys. Earth Planet. Inter.,* 28:320–336.

Ashi, J., and Taira, A., 1992. Structure of the Nankai accretionary prism as revealed from IZANAGI sidescan imagery and multichannel seismic reflection profiling. *Isl. Arc,* 1:104–115.

————, 1993. Thermal structure of the Nankai accretionary prism as inferred from the distribution of gas hydrate BSRs. *In* Underwood, M.B. (Ed.), *Thermal Evolution of the Tertiary Shimanto Belt, Southwest Japan: An Example of Ridge-trench Interaction.* Spec. Pap.—Geol. Soc. Am., 273:137–149.

Bangs, N.L., Taira, A., Kuramoto, S., Shipley, T.H., Moore, G.F., Mochizuki, K., Gulick, S.S., Zhao, Z., Nakamura, Y., Park, J.-O., Taylor, B.L., Morita, S., Ito, S., Hills, D.J., Leslie, S.C., Alex, C.M., McCutcheon, A.J., Ike, T., Yagi, H., and Toyama, G., 1999. U.S.-Japan Collaborative 3-D seismic investigation of the Nankai Trough plate-boundary interface and shallowmost seismogenic zone. *Eos,* 80:F569.

Blöchl, E., Rachel, R., Burggraf, S., Hafenbradl, D., Jannasch, H.W., and Stetter, K.O., 1997. *Pyrolobus fumarii,* gen. and sp. nov., represents a novel group of archaea, extending the upper temperature limit for life to 113°C. *Extremophiles,* 1:14–21.

Bray, C.J., and Karig, D.E., 1985. Porosity of sediments in accretionary prisms and some implications for dewatering processes. *J. Geophys. Res.,* 90:768–778.

Byrne, T., Maltman, A., Stephenson, E., Soh, W., and Knipe, R., 1993. Deformation structures and fluid flow in the toe region of the Nankai accretionary prism. *In* Hill, I.A., Taira, A., Firth, J.V., et al., *Proc. ODP, Sci. Results,* 131: College Station, TX (Ocean Drilling Program), 83–101.

Davis, E.E., Becker, K., Pettigrew, T., Carson, B., and MacDonald, R., 1992. CORK: a hydrologic seal and downhole observatory for deep-ocean boreholes. *In* Davis, E.E., Mottl, M.J., Fisher, A.T., et al., *Proc. ODP, Init. Repts.,* 139: College Station, TX (Ocean Drilling Program), 43–53.

Hyndman, R.D., Wang, K., and Yamano, M., 1995. Thermal constraints on the seismogenic portion of the southwestern Japan subduction thrust. *J. Geophys. Res.,* 100:15373–15392.

Hyndman, R.D., Yamano, M., and Oleskevich, D.A., 1997. The seismogenic zone of subduction thrust faults. *Isl. Arc,* 6:244–260.

Ito,Y., and Nagasaki, Y., 1997. Crustal shortening of southwest Japan in the late Miocene. *Isl. Arc,* 5:337–353.

Jolivet, L.K., Tamaki, K., and Frounier, M., 1994. Japan Sea, opening history and mechanism: a synthesis. *J. Geophys. Res.,* 99:22237–22259.

Kamata, H., and Kodama, K., 1994. Tectonics of an arc-arc junction: an example from Kyushu Island at the junction of the Southwest Japan Arc and the Ryukyu Arc. *Tectonophysics,* 233:69–81.

Kano, K., Kato, H., Yanagisawa, Y., and Yoshida, F., 1991. Stratigraphy and geologic history of the Cenozoic of Japan. *Geol. Surv. Jpn.,* 274:114.

Karig, D.E., 1986. The framework of deformation in the Nankai Trough. *In* Kagami, H., Karig, D.E., and Coulbourn, W.T., et al., *Init. Repts. DSDP,* 87: Washington (U.S. Govt. Printing Office), 927–940.

Karig, D.E., and Angevine, C.L., 1986. Geologic constraints on subduction rates in the Nankai Trough. *In* Kagami, H., Karig, D.E., and Coulbourn, W.T., et al., *Init. Repts. DSDP,* 87: Washington (U.S. Govt. Printing Office), 789–796.

Kastner, M., Elderfield, H., Jenkins, W.J., Gieskes, J.M., and Gamo, T., 1993. Geochemical and isotopic evidence for fluid flow in the western Nankai subduction zone, Japan. *In* Hill, I.A., Taira, A., Firth, J.V., et al., *Proc. ODP, Sci. Results,* 131: College Station, TX (Ocean Drilling Program), 397–413.

Kinoshita, H., and Yamano, M., 1986. The heat flow anomaly in the Nankai Trough area. *In* Kagami, H., Karig, D.E., Coulbourn, W.T., et al., *Init. Repts DSDP,* 87: Washington (U.S. Govt. Printing Office), 737–743.

Kodaira, S., 2000. High resolution imaging of seismogenic plate boundary. *Ann. Rep. Frontier Res. Progr. Subduct. Dyn.,* 39–44.

Kodaira, S., Takahashi, N., Park, J., Mochizuki, K., Shinohara, M., and Kimura, S., 2000. Western Nankai Trough seismogenic zone: results from a wide-angle ocean bottom seismic survey. *J. Geophys. Res.,* 105:5887–5905.

Le Pichon, X., Iiyama, T., Chamley, H., Charvet, J., Faure, M., Fujimoto, H., Furuta, T., Ida, Y., Kagami, H., Lallemant, S., Leggett, J., Murata, A., Okada, H., Rangin, C., Renard, V., Taira, A., and Tokuyama, H., 1987. Nankai Trough and fossil Shikoku Ridge: results of Box 6 Kaiko Survey. *Earth Planet. Sci. Lett.,* 83:186–198.

Le Pichon, X., Mazzotti, M., Henry, P., and Hashimoto, M., 1998. Deformation of the Japanese Islands and seismic coupling: an interpretation based on GSI permanent GPS observations. *Geophys. J. Int.,* 134:501–514.

Maltman, A.J., Byrne, T., Karig, D.E., Lallemant, S., Knipe, R., and Prior, D., 1993. Deformation structures at Site 808, Nankai accretionary prism, Japan. *In* Hill, I.A., Taira, A., Firth, J.V., et al., *Proc. ODP, Sci. Results,* 131: College Station, TX (Ocean Drilling Program), 123–133.

Mazzotti, S., LePichon, X., Henry, P., and Miyazaki, S., 2000. Full interseismic locking of the Nankai and Japan-West Kuril Subduction Zones: an analysis of uniform elastic strain accumulation in Japan constrained by permanent GPS. *J. Geophys. Res.,* 105:13159–13177.

Moore, G.F., Karig, D.E., Shipley, T.H., Taira, A., Stoffa, P.L., and Wood, W.T., 1991. Structural framework of the ODP Leg 131 area, Nankai Trough. *In* Taira, A., Hill, I., Firth, J.V., et al., *Proc. ODP, Init. Repts.,* 131: College Station, TX (Ocean Drilling Program), 15–20.

Moore, G.F., and Shipley, T.H., 1993. Character of the décollement in the Leg 131 area, Nankai Trough. *In* Hill, I.A., Taira, A., Firth, J.V., et al., *Proc. ODP, Sci. Results,* 131: College Station, TX (Ocean Drilling Program), 73–82.

Moore, G.F., Shipley, T.H., Stoffa, P.L., Karig, D.E., Taira, A., Kuramoto, S., Tokuyama, H., and Suyehiro, K., 1990. Structure of the Nankai Trough accretionary zone from multichannel seismic reflection data. *J. Geophys. Res.,* 95:8753–8765.

Moore, G.F., Taira, A., Kuramoto, S., Shipley, T.H., and Bangs, N.L., 1999. Structural setting of the 1999 U.S.-Japan Nankai Trough 3-D seismic reflection survey. *Eos,* 80:F569.

Morgan, J.K., and Karig, D.E., 1995a. Décollement processes at the Nankai accretionary margin, Southeast Japan. *J. Geophys. Res.,* 100:15221–15231.

————, 1995b. Kinematics and a balanced and restored cross-section across the toe of the eastern Nankai accretionary prism. *J. Struct. Geol.,* 17:31–45.

Niitsuma, N., 1989. Collision tectonics in the southern Fossa Magna, central Japan. *Mod. Geol.,* 14:3–18.

Ohmori, K., Taira, A., Tokuyama, H., Sagaguch, A., Okamura, M., and Aihara., A., 1997. Paleothermal structure of the Shimanto accretionary prism, Shikoku, Japan: role of an out-of-sequence thrust. *Geology,* 25:327–330.

Okamura, Y., Kisimoto, K., Murakami, F., and Joshima, M., 1987. Geological map of Tosa Bay. *Geol. Surv. Jpn., Mar. Geol. Map Ser.,* 29 (scale 1:200,000).

Okino, K., and Kato, Y., 1995. Geomorphological study on a clastic accretionary prism: the Nankai Trough. *Isl. Arc,* 4:182–198.

Okino, K., Shimakawa, Y., and Nagaoka, S., 1994. Evolution of the Shikoku basin. *J. Geomagn. Geoelectr.,* 46:463–479.

Otofuji, Y., 1996. Large tectonic movement of the Japan Arc in late Cenozoic times inferred from paleomagnetism: review and synthesis. *Isl. Arc,* 5:229–249.

Park, J.-O., Tsuru, T., Kaneda, Y., Kono, Y., Kodaira, S., Takahashi, N., and Kinoshita, H., 1999. A subducting seamount beneath the Nankai accretionary prism off Shikoku, southwestern Japan. *Geophys. Res. Lett.,* 26:931–934.

Park, J.-O., Tsuru, T., Kodaira, S., Nakanisi, A., Miura, S., Kaneda, Y., and Kono, Y., 2000. Out-of-sequence thrust faults developed in the coseismic slip zone of the 1946 Nankai earthquake (Mw = 8.2) off Shikoku, southwest Japan. *Geophys. Res. Lett.,* 27:1033–1036.

Parkes, R.J., Cragg, B.A., Bale, S.J., Getliff, J.M., Goodman, K., Rochelle, P.A., Fry, J.C., Weightman, A.J., and Harvey, S.M., 1994. A deep bacterial biosphere in Pacific Ocean sediments. *Nature,* 371:410–413.

Pickering, K.T., Underwood, M.B., and Taira, A., 1993. Open-ocean to trench turbidity-current flow in the Nankai Trough: flow collapse and flow reflection. *In* Hill, I.A., Taira, A., Firth, J.V., et al., *Proc. ODP, Sci. Results,* 131: College Station, TX (Ocean Drilling Program), 35–43.

Saffer, D.M., and Bekins, B.A., 1998. Episodic fluid flow in the Nankai Accretionary Complex: timescale, geochemistry, flow rates, and fluid budget. *J. Geophys. Res.,* 103:30351–30371.

Saffer, D.M., Silver, E.A., Fisher, A.T., Tobin, H., and Moran, K., 2000. Inferred pore pressures at the Costa Rica subduction zone: implications for dewatering processes. *Earth Planet. Sci. Lett.,* 177:193–207.

Sagiya, T., and Thatcher, W., 1999. Coseismic slip resolution along a plate boundary megathrust: the Nankai Trough, Southwest Japan. *J. Geophys. Res.,* 104:1111–1129.

Seno, T., 1977. The instantaneous rotation vector of the Philippine Sea Plate relative to the Eurasian Plate. *Tectonophysics,* 42:209–226.

Shipboard Scientific Party, 1975. Site 297. *In* Karig, D.E., Ingle, J.C., Jr., et al., *Init. Repts. DSDP,* 31: Washington (U.S. Govt. Printing Office), 275–316.

————, 1986. Site 582. *In* Kagami, H., Karig, D.E., Coulbourn, W.T., et al., *Init. Repts. DSDP,* 87: Washington (U.S. Govt. Printing Office), 35–122.

————, 1991. Site 808. *In* Taira, A., Hill, I., Firth, J.V., et al., *Proc. ODP, Init. Repts.,* 131: College Station, TX (Ocean Drilling Program), 71–269.

Stoffa, P.L., Wood, W.T., Shipley, T.H., Moore, G.F., Nishiyama, E., Bothelo, M.A.B., Taira, A., Tokuyama, H., and Suyehiro, K., 1992. Deepwater high-resolution expanding spread and split spread marine seismic profiles in the Nankai Trough. *J. Geophys. Res.,* 97:1687–1713.

Sugiyama, Y., 1994. Neotectonics of Southwest Japan due to the right oblique subduction of the Philippine sea plate. *Geofis. Inter.,* 33:53–76.

Taira, A., and Ashi, J., 1993. Sedimentary facies evolution of the Nankai forearc and its implications for the growth of the Shimanto accretionary prism. *In* Hill, I.A., Taira, A., Firth, J.V., et al., *Proc. ODP, Sci. Results,* 131: College Station, TX (Ocean Drilling Program), 331–341.

Taira, A., Hill, I., Firth, J., Berner, U., Brückmann, W., Byrne, T., Chabernaud, T., Fisher, A., Foucher, J.-P., Gamo, T., Gieskes, J., Hyndman, R., Karig, D., Kastner, M., Kato, Y., Lallement, S., Lu, R., Maltman, A., Moore, G., Moran, K., Olaffson, G., Owens, W., Pickering, K., Siena, F., Taylor, E., Underwood, M., Wilkinson, C., Yamano, M., and Zhang, J., 1992. Sediment deformation and hydrogeology of the Nankai Trough accretionary prism: synthesis of shipboard results of ODP Leg 131. *Earth Planet. Sci. Lett.,* 109:431–450.

Taira, A., Hill, I., Firth, J.V., et al., 1991. *Proc. ODP, Init. Repts.,* 131: College Station, TX (Ocean Drilling Program).

Taira, A., Katto, J., Tashiro, M., Okamura, M., and Kodama, K., 1988. The Shimanto Belt in Shikoku, Japan—evolution of Cretaceous to Miocene accretionary prism. *Mod. Geol.,* 12:5–46.

Taira, A., and Niitsuma, N., 1986. Turbidite sedimentation in the Nankai Trough as interpreted from magnetic fabric, grain size, and detrital modal analyses. *In* Kagami, H., Karig, D.E., Coulbourn, W.T., et al., *Init. Repts. DSDP,* 87: Washington (U.S. Govt. Printing Office), 611–632.

Taira, A., Tokuyama, H., and Soh, W., 1989. Accretion tectonics and evolution of Japan. *In* Ben-Avraham, Z. (Ed.), *The Evolution of Pacific Ocean Margins:* Oxford (Oxford Univ. Press), 100–123.

Takahashi, M., 1999. Large felsic magmatism of the Miocene outerzone of southwest Japan. *Earth Monthly [Gekkan Chikyu],* Spec. Vol. 23:160–168. (in Japanese)

Taylor, B., 1992. Rifting and the volcanic-tectonic evolution of the Izu-Bonin-Mariana Arc. *In* Taylor, B., Fujioka, K., et al., *Proc. ODP, Sci. Results,* 126: College Station, TX (Ocean Drilling Program), 627–651.

Tokuyama, H., Ashi, J., Soh, W., Kuramoto, S., and Ikeda, Y., 1999. *Submarine Active Faults off Tokai:* Tokyo (Univ. of Tokyo Press). (in Japanese)

Underwood, M.B., Orr, R., Pickering, K., and Taira, A., 1993. Provenance and dispersal patterns of sediments in the turbidite wedge of Nankai Trough. *In* Hill, I.A., Taira, A., Firth, J.V., et al., *Proc. ODP, Sci. Results,* 131: College Station, TX (Ocean Drilling Program), 15–34.

Yamazaki, T., and Okamura, Y., 1989. Subducting seamounts and deformation of overriding forearc wedges around Japan. *Tectonophysics,* 160:207–229.

Figure F1. Shaded relief map of the Nankai Trough produced from the Hydrographic Department of Japan's topographic data set (500-m grid interval). The inset shows a tectonic map of the Philippine Sea region that includes the Nankai Trough. The black box outlines the Leg 190 Nankai drilling area shown in Figure F6, p. 47. The arrow shows the convergence direction of the Shikoku Basin beneath Japan.

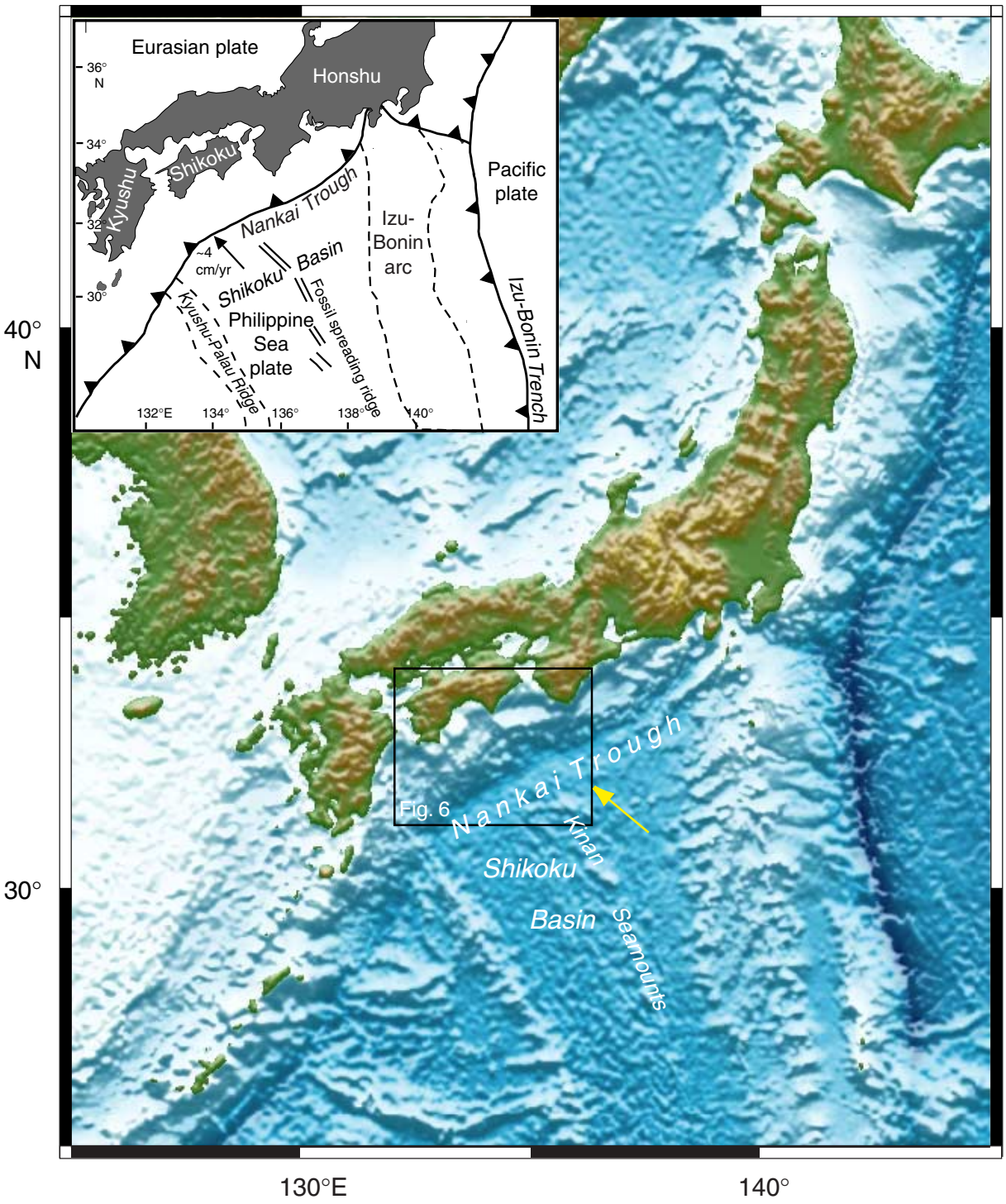

Figure F2. Geologic map of the southwest Japan forearc region and the Leg 190 Muroto and Ashizuri drilling transects. The Shimanto accretionary prism provides a landward analog of the Nankai accretionary prism. Note the widespread 17- to 12-Ma igneous activity, probably due to the initial subduction of the young Shikoku Basin oceanic lithosphere. Previous ODP/DSDP drill sites are shown by open circles. The dashed line shows the location of the cross section shown in Figure F3, p. 44.

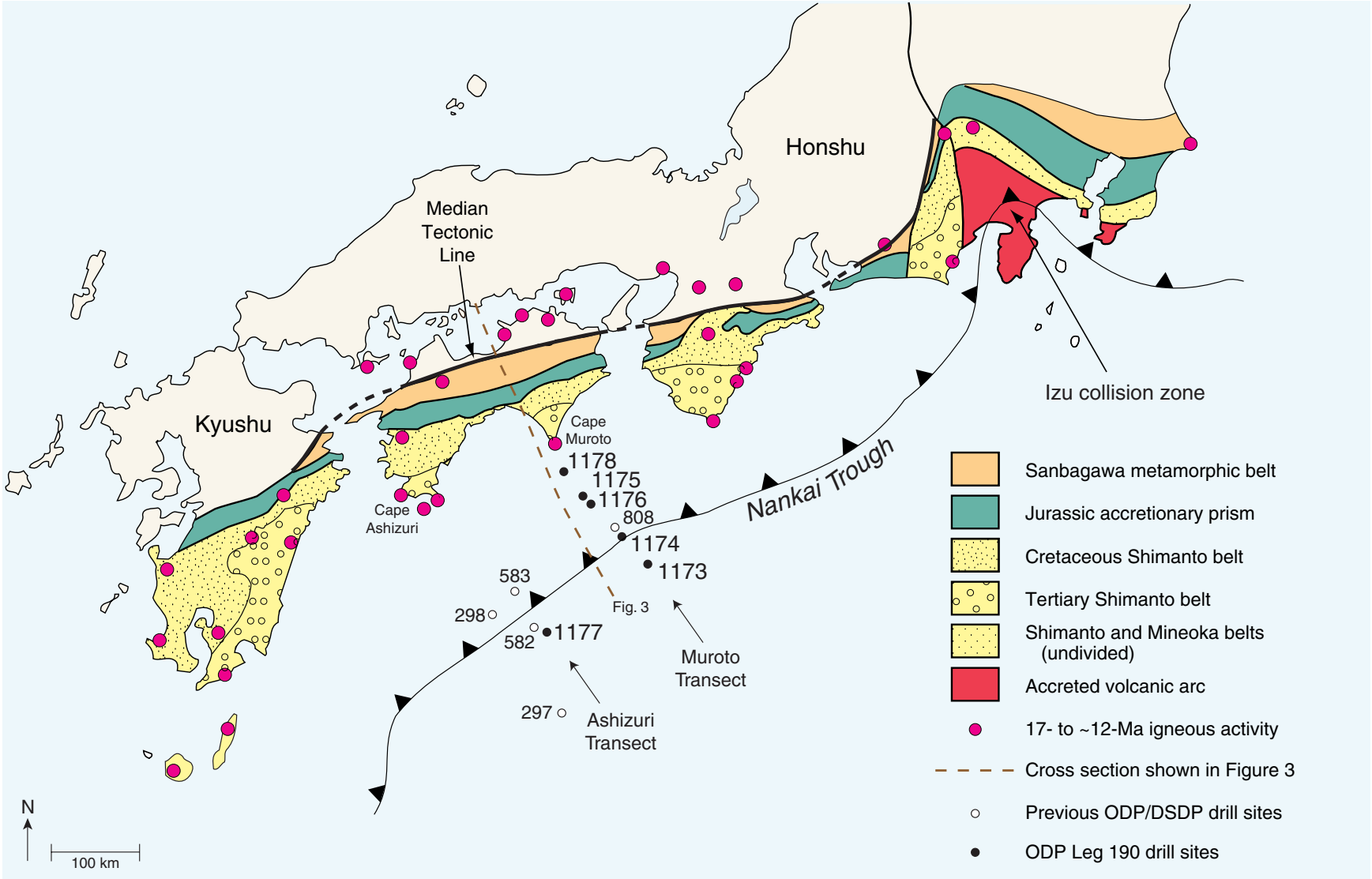

Figure F3. Crustal cross section of the Nankai Trough forearc (modified after Kodaira et al., 2000). Crustal structure, crustal velocities, and subducting plate earthquakes are shown. Note that the updip limit of 1946 Nankaido earthquake rupture zone possibly reaches to the Nankai Trough accretionary prism.

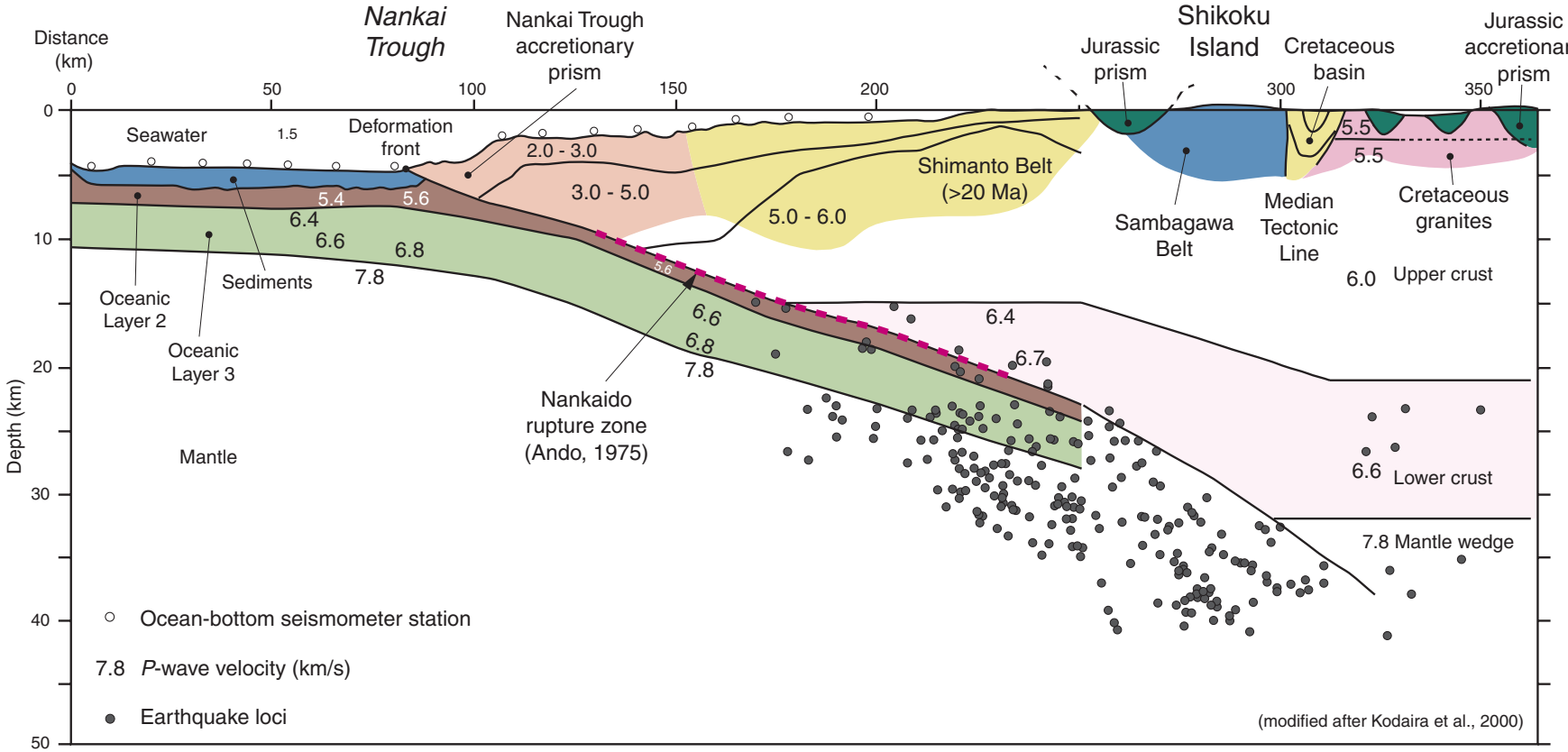

Figure F4. Paleogeographic reconstruction of the Shimanto Belt and Nankai forearc evolution (modified after Taira et al., 1989). Arrows show the direction of convergence.

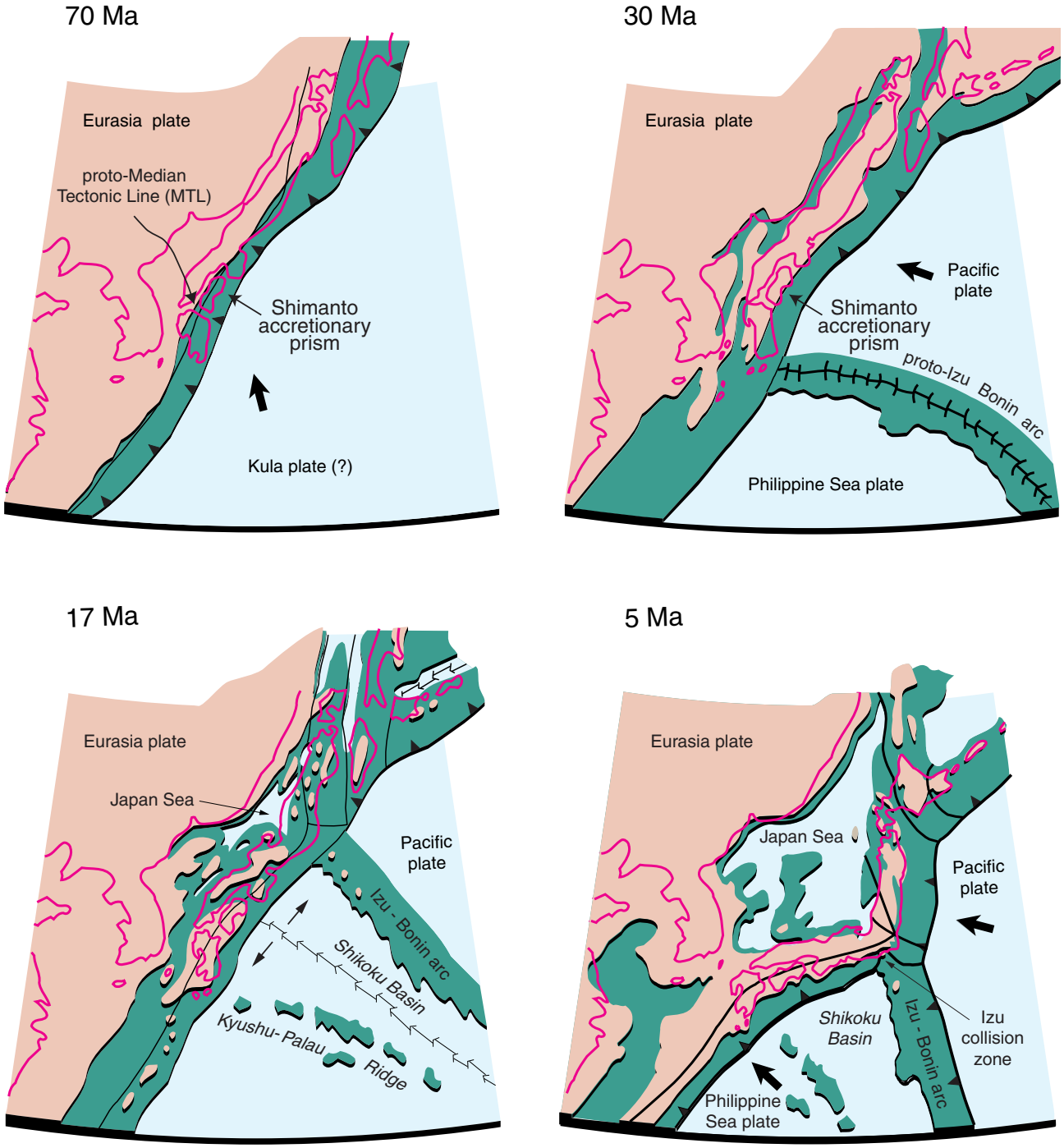

Figure F5. Historical recurrence time interval of class M8 earthquakes along the Nankai Trough. Zones A to D represent rupture area segments.

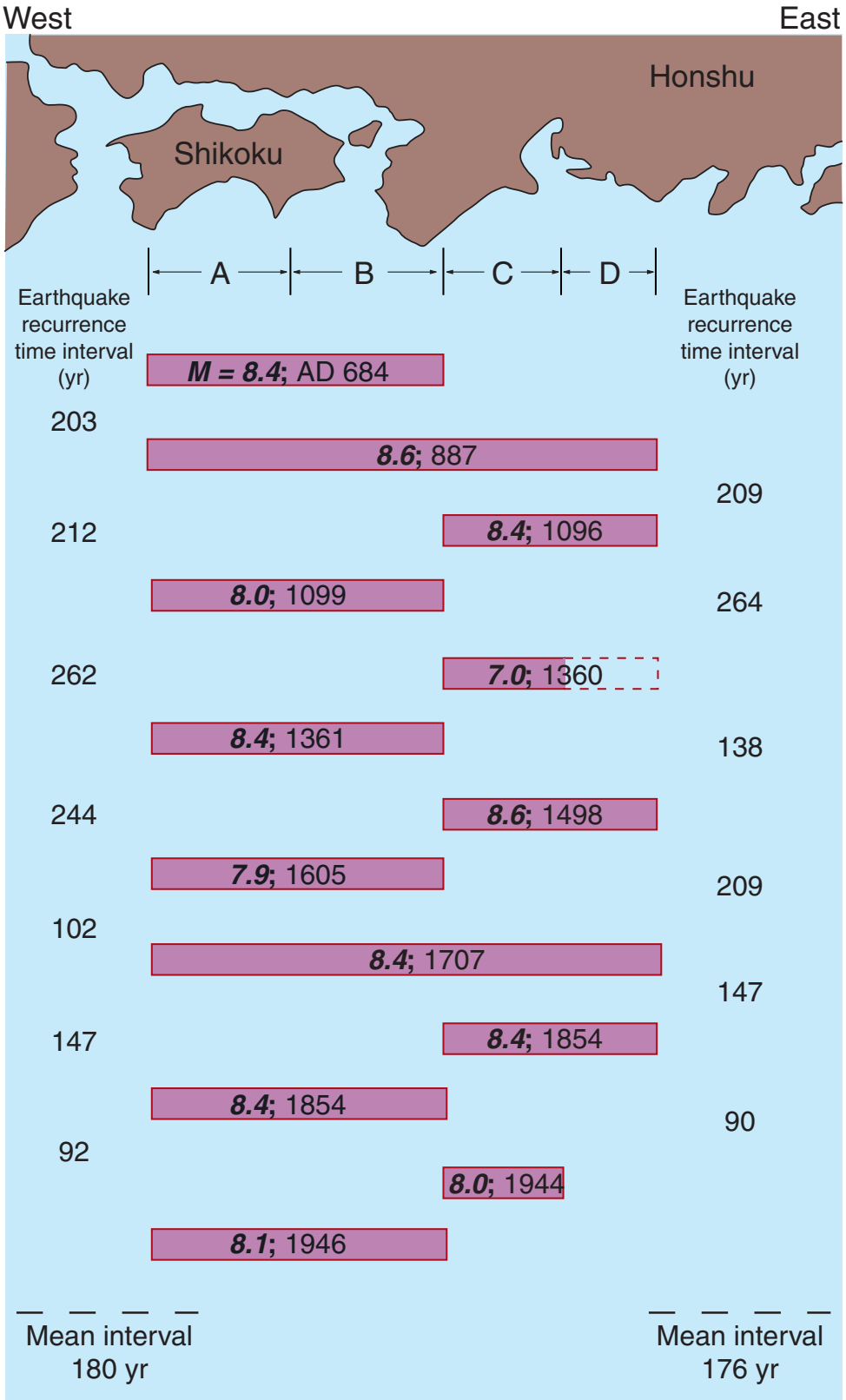

Figure F6. ODP Leg 190 (solid circles) and previous ODP/DSDP drill sites (solid squares) in the Nankai Trough. The shaded outline shows the 3-D seismic survey of Bangs et al. (1999) and Moore et al. (1999). Contour interval = 100 m.

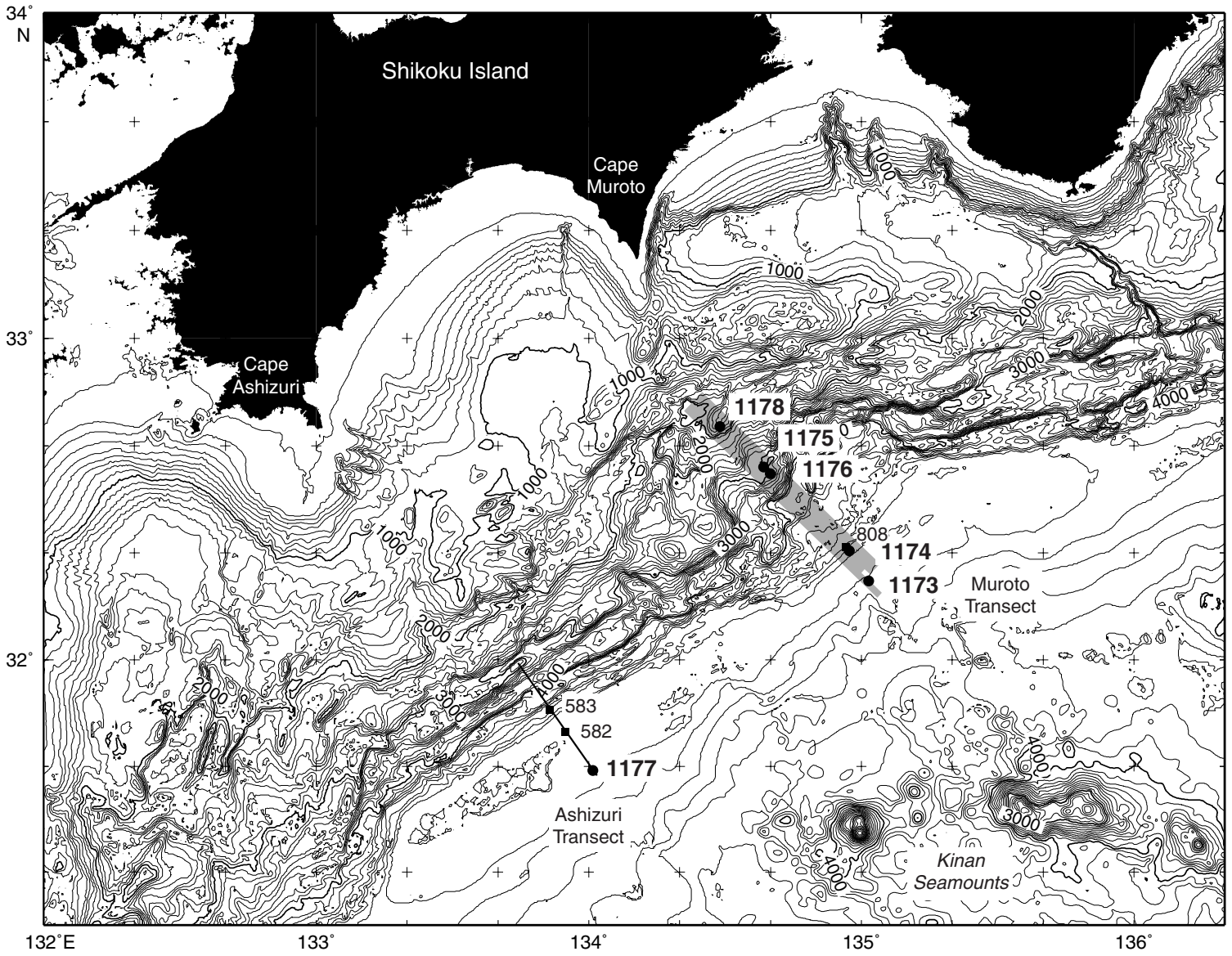

Figure F7. Schematic interpretation of seismic line 141-2D in the Muroto Transect showing tectonic domains and location of Leg 190 drill sites.

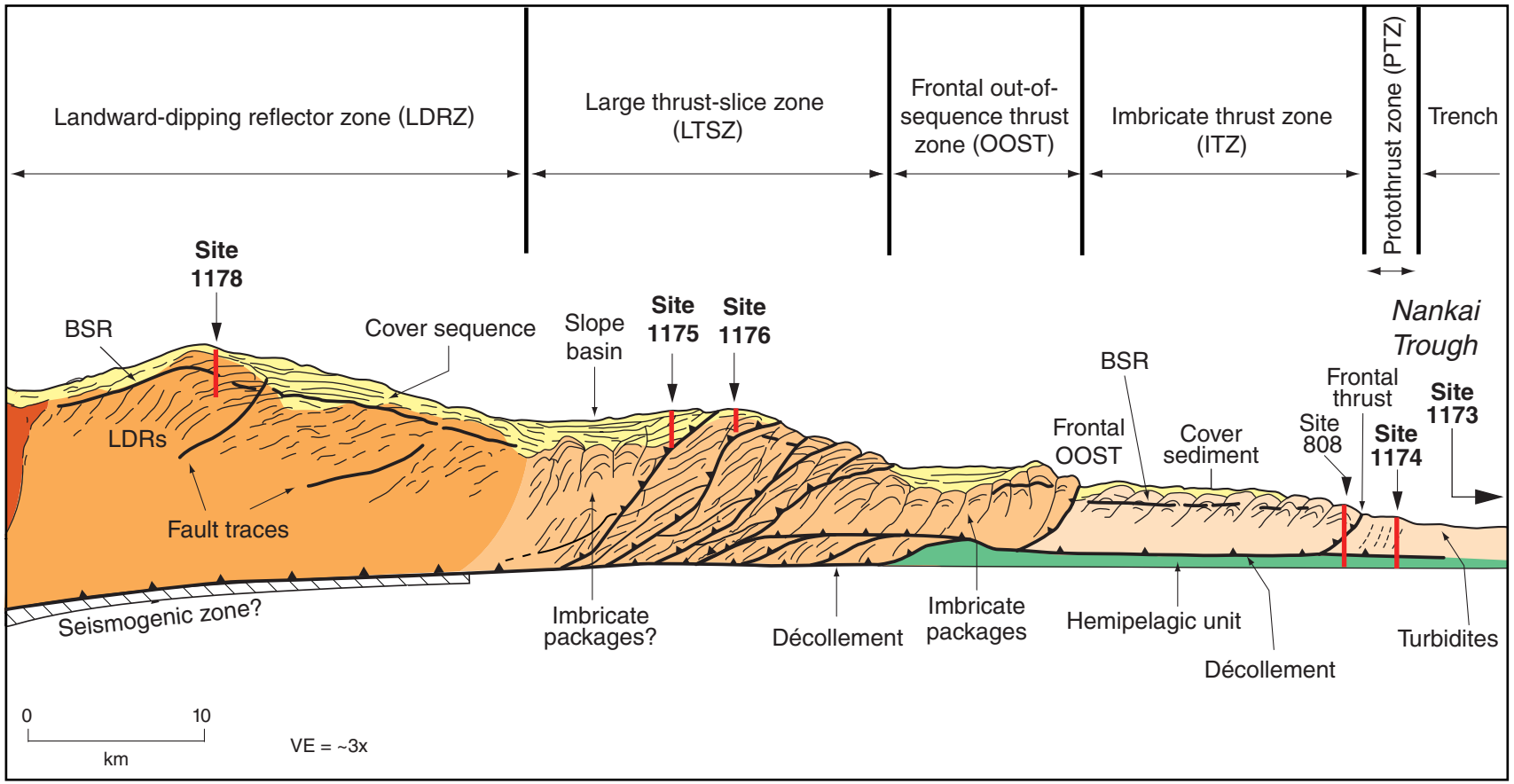

Figure F8. A. Correlation of facies units, magnetic susceptibility, and major time boundaries within stratigraphic successions of the reference and prism toe sites at the Muroto and Ashizuri Transects at Nankai margin. Time boundaries are in red (solid line). Facies boundaries are in blue (Muroto Transect) and purple (Ashizuri Transect) (patterned lines). Data for DSDP Site 297 are from Shipboard Scientific Party (1975). Data for DSDP Site 582 are from Shipboard Scientific Party (1986). Data for ODP Site 808 are from Shipboard Scientific Party (1991). Note that the effects of facies imbrication along the frontal thrust of Site 808 have been removed and that the position of the Pliocene/Miocene boundary has been shifted in response to reinterpretation of paleomagnetic data. (**Figure shown on next two pages.**) (This figure is also available in an **oversized format.**)

Figure F8 (continued). (Caption shown on previous page.)

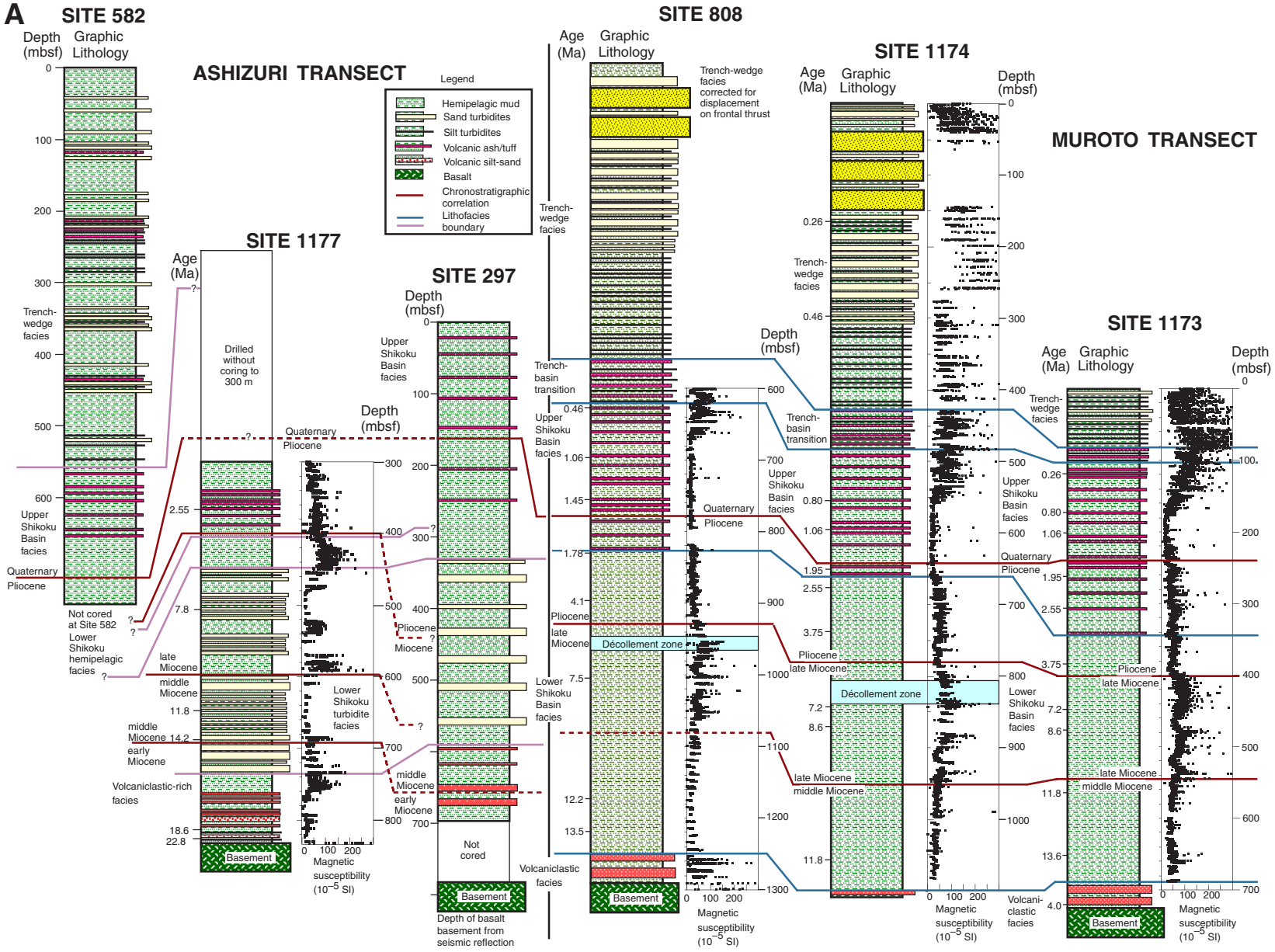

Figure F8 (continued). B. Correlation of facies units, magnetic susceptibility, and major time boundaries within stratigraphic successions cored at upslope sites of the Muroto Transect, Nankai margin. Time boundaries are in red (solid line). Facies boundaries are in blue (patterned line). (This figure is also available in an **oversized format.**)

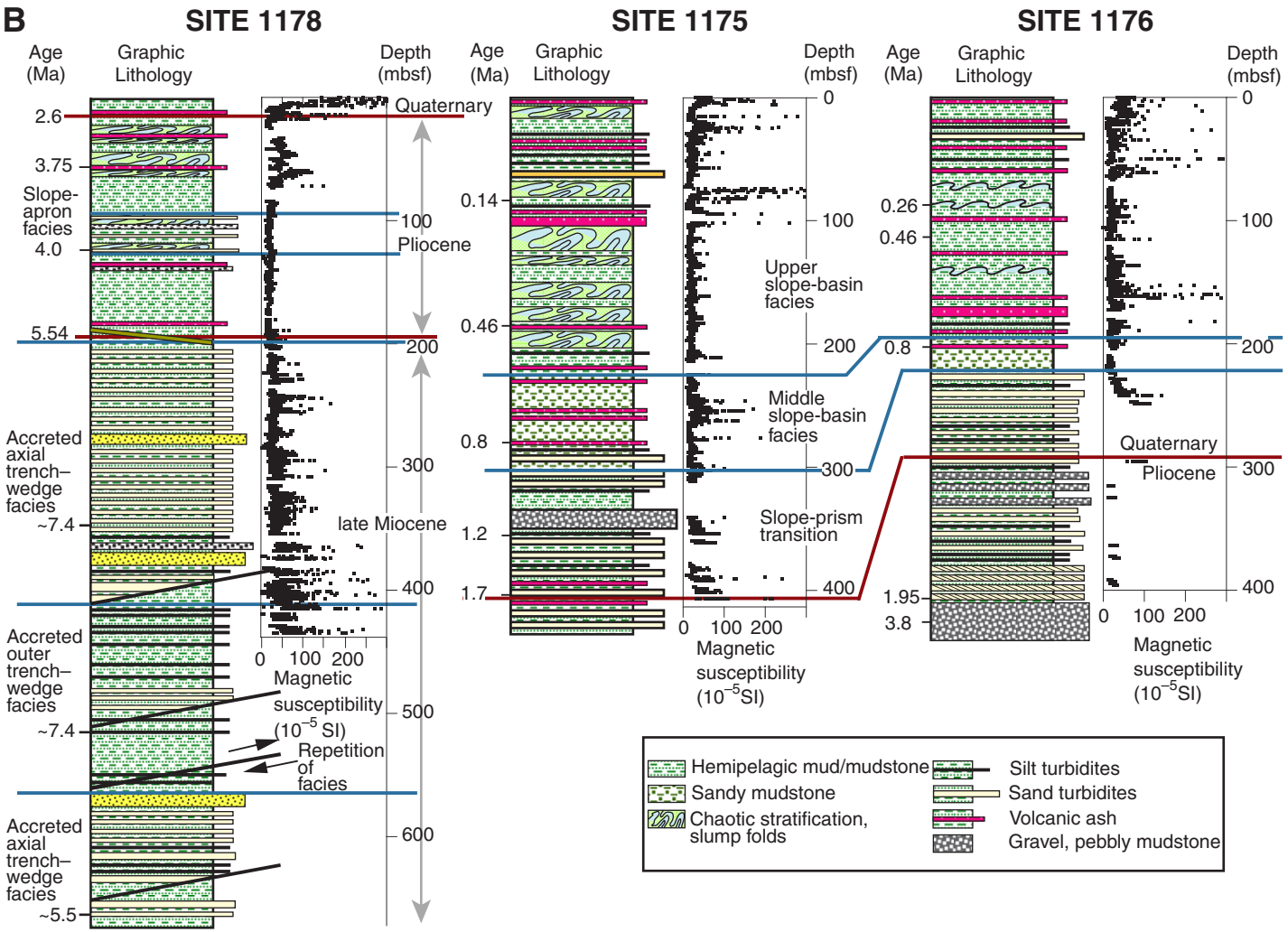

Figure F9. Seismic reflection profile through the Muroto Transect reference (Site 1173) and prism toe sites (Sites 1174 and 808). Correlation of sedimentary facies to the seismic data is shown on the right. Seismic data are from the 3-D seismic survey of Bangs et al. (1999) and Moore et al. (1999). Xline identifies the crossing line number in the 3-D seismic volume. The location of the profile is shown in Figure F2, p. 10, in the "Data Report: Structural Setting of the Leg 190 Muroto Transect" chapter.

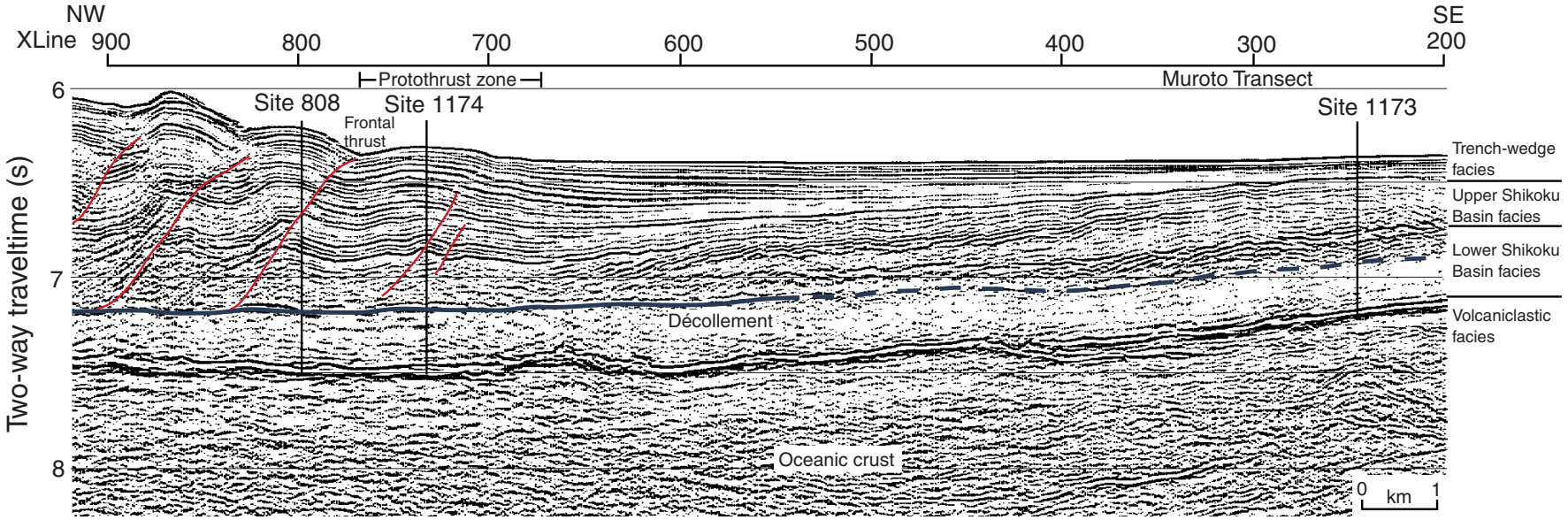

Figure F10. Seismic reflection profile (NT-2) through Ashizuri Transect reference site (Site 1177), trench site (Site 582), and prism toe site (Site 583).

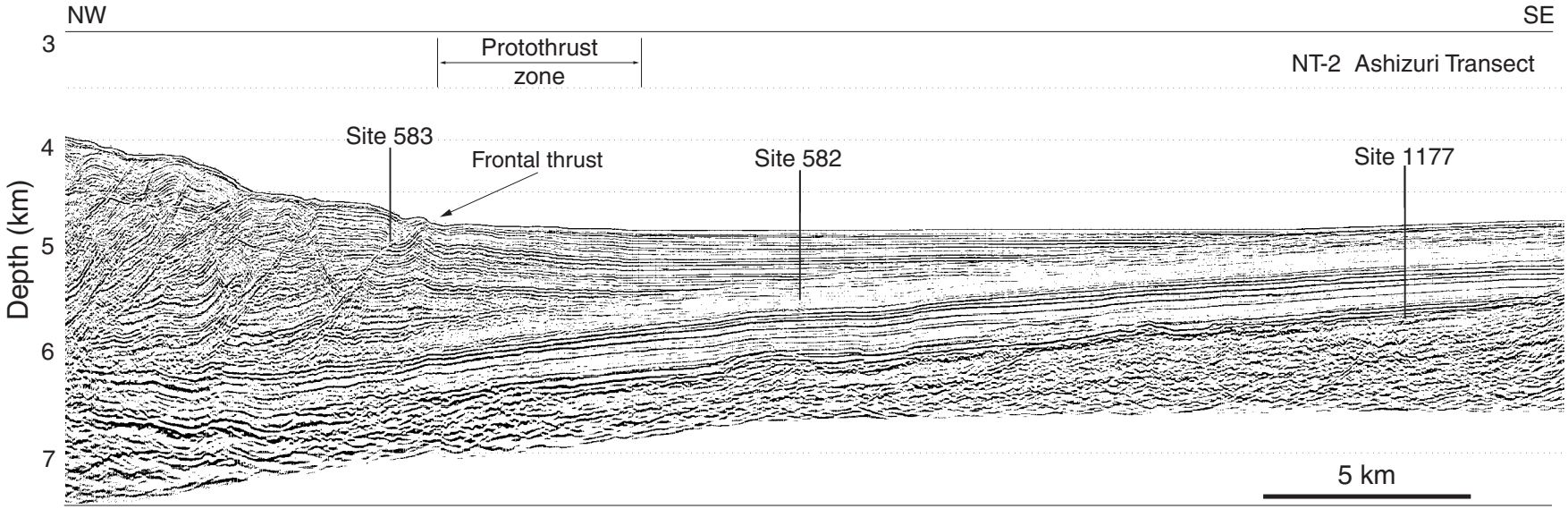

Figure F11. Seismic reflection profile through the Muroto Transect slope Sites 1175, 1176, and 1178. Seismic data are from the 3-D seismic survey of Bangs et al. (1999) and Moore et al. (1999). Xline identifies the crossing line number in the 3-D seismic volume. The location of the profile is shown in Figure F2, p. 10, in the "Data Report: Structural Setting of the Leg 190 Muroto Transect" chapter.

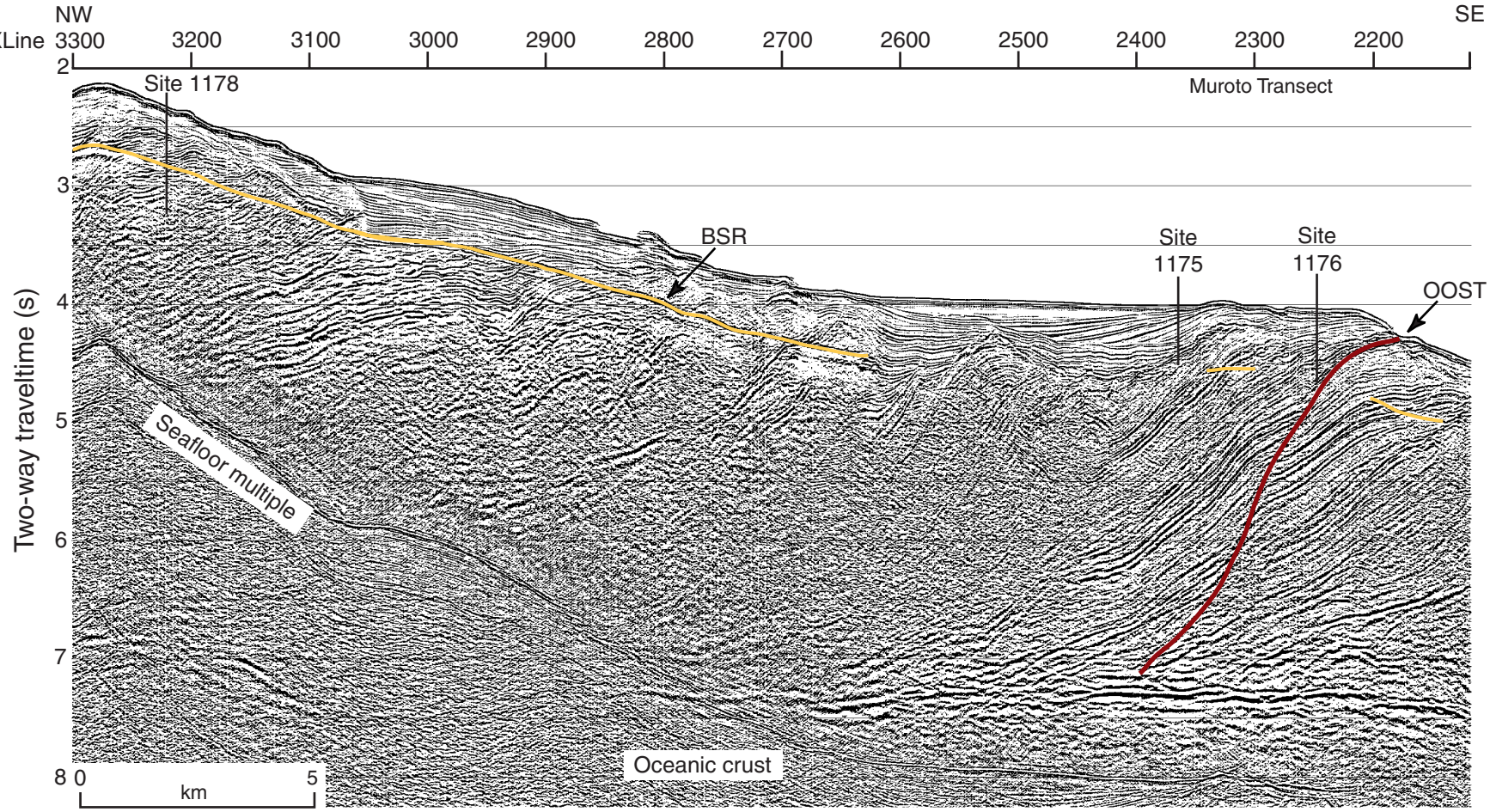

Figure F12. Summary of results at Site 1173.

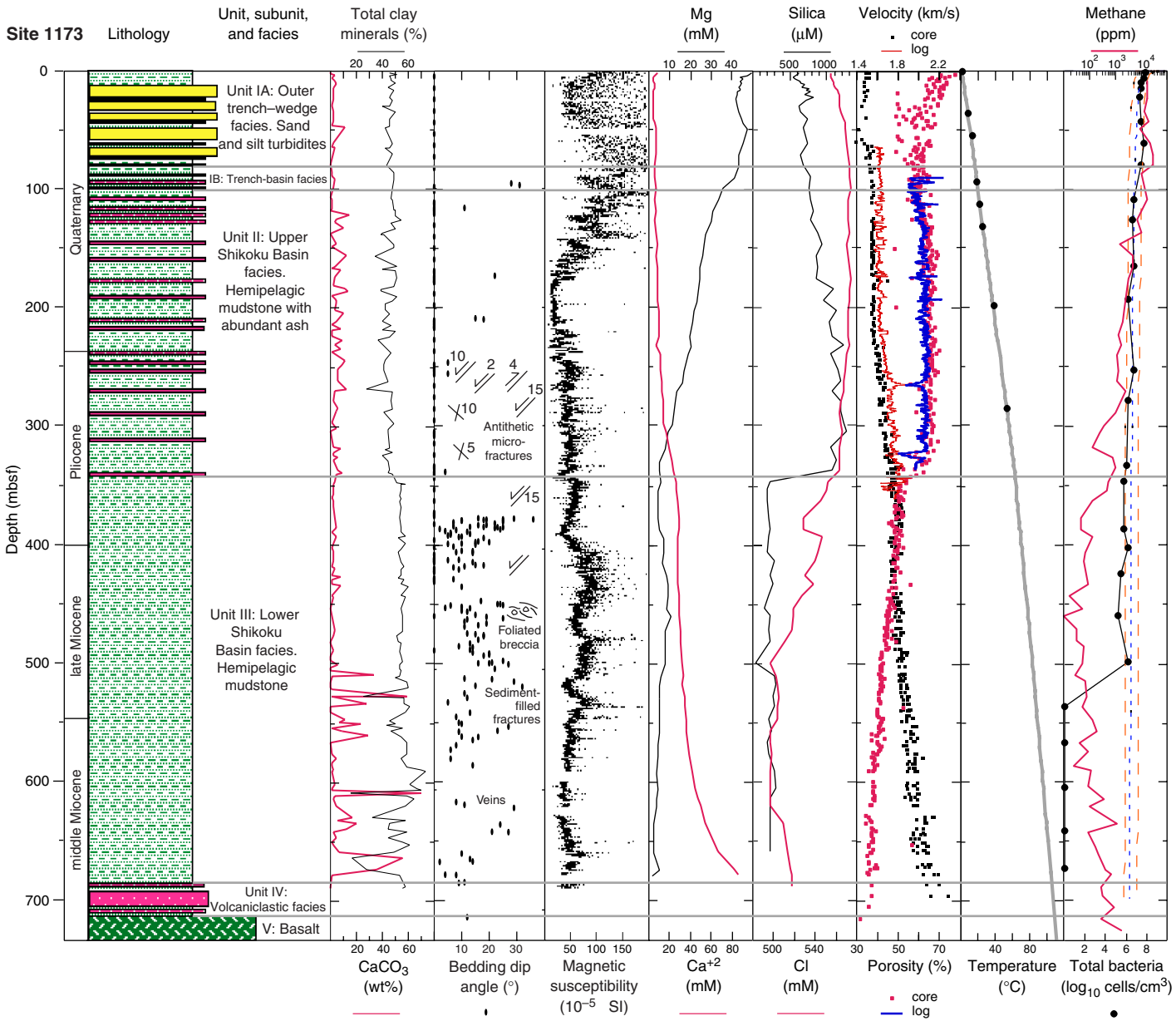

Figure F13. Volcanic ash beds interbedded with silty clay from Unit II (interval 190-1173A-13H-6, 100–124 cm).

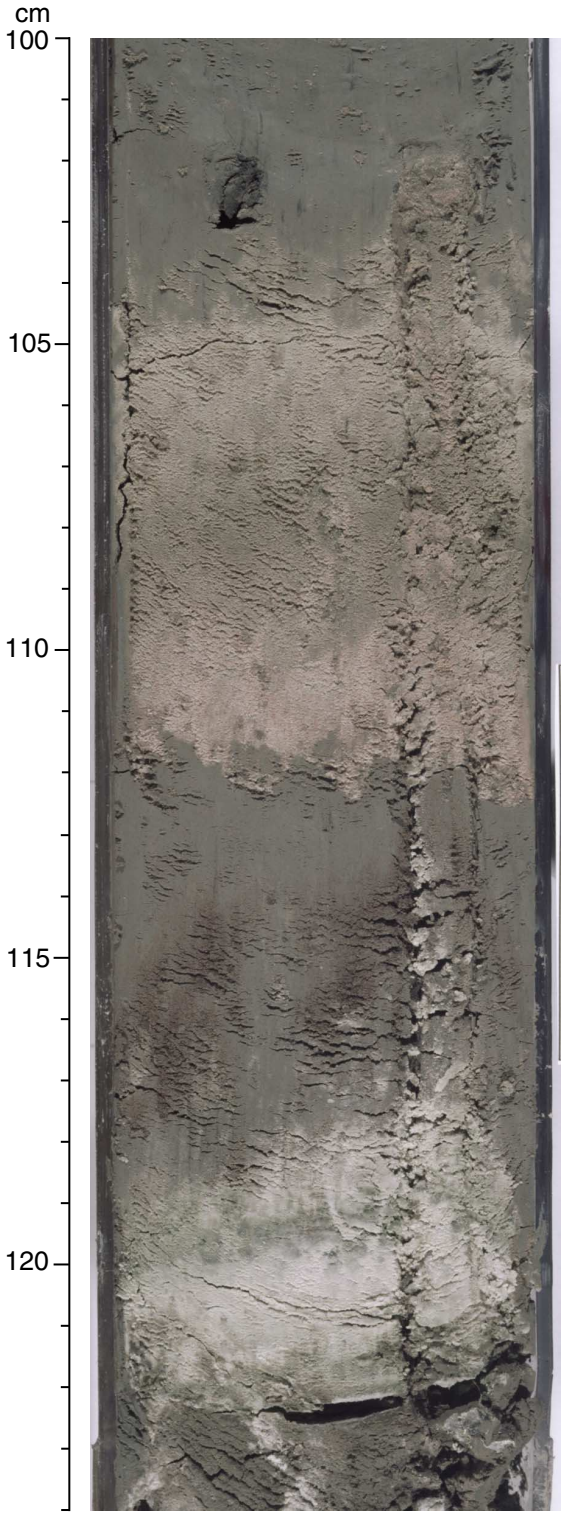

Figure F14. Bioturbated silty claystone and interbedded siliceous claystone from Unit III (interval 190-1173A-57X-4, 66–71 cm).

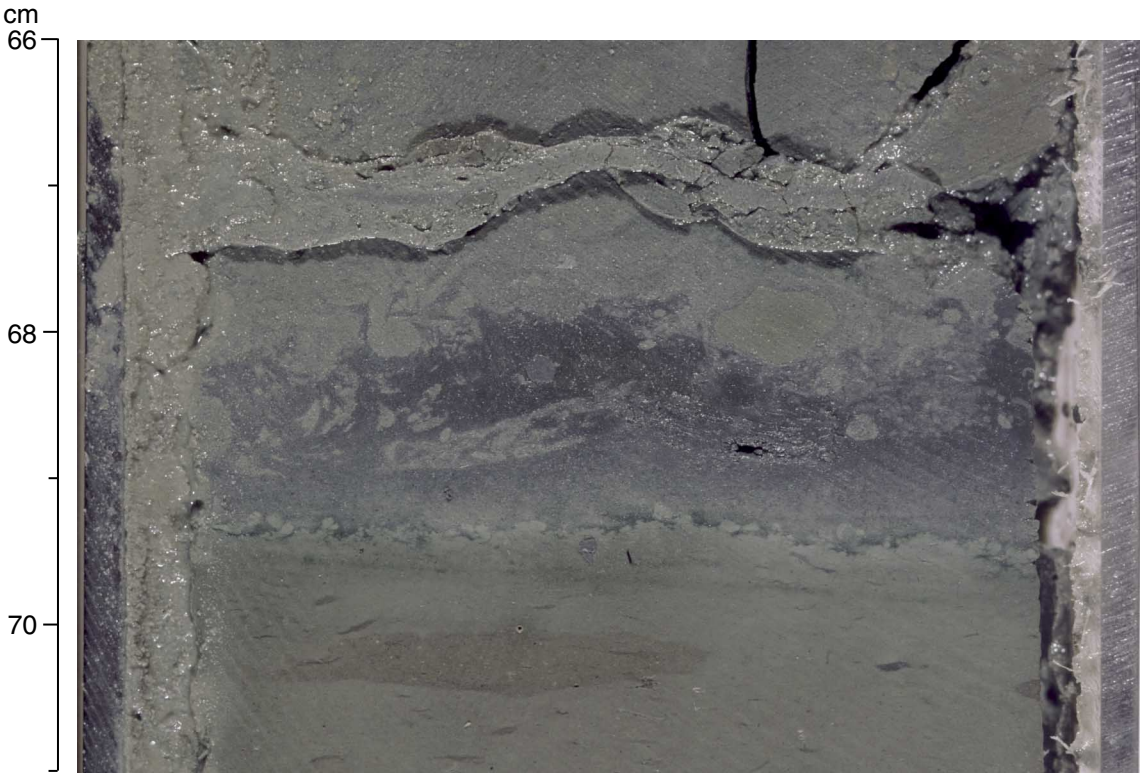

Figure F15. Summary of results at Site 1174.

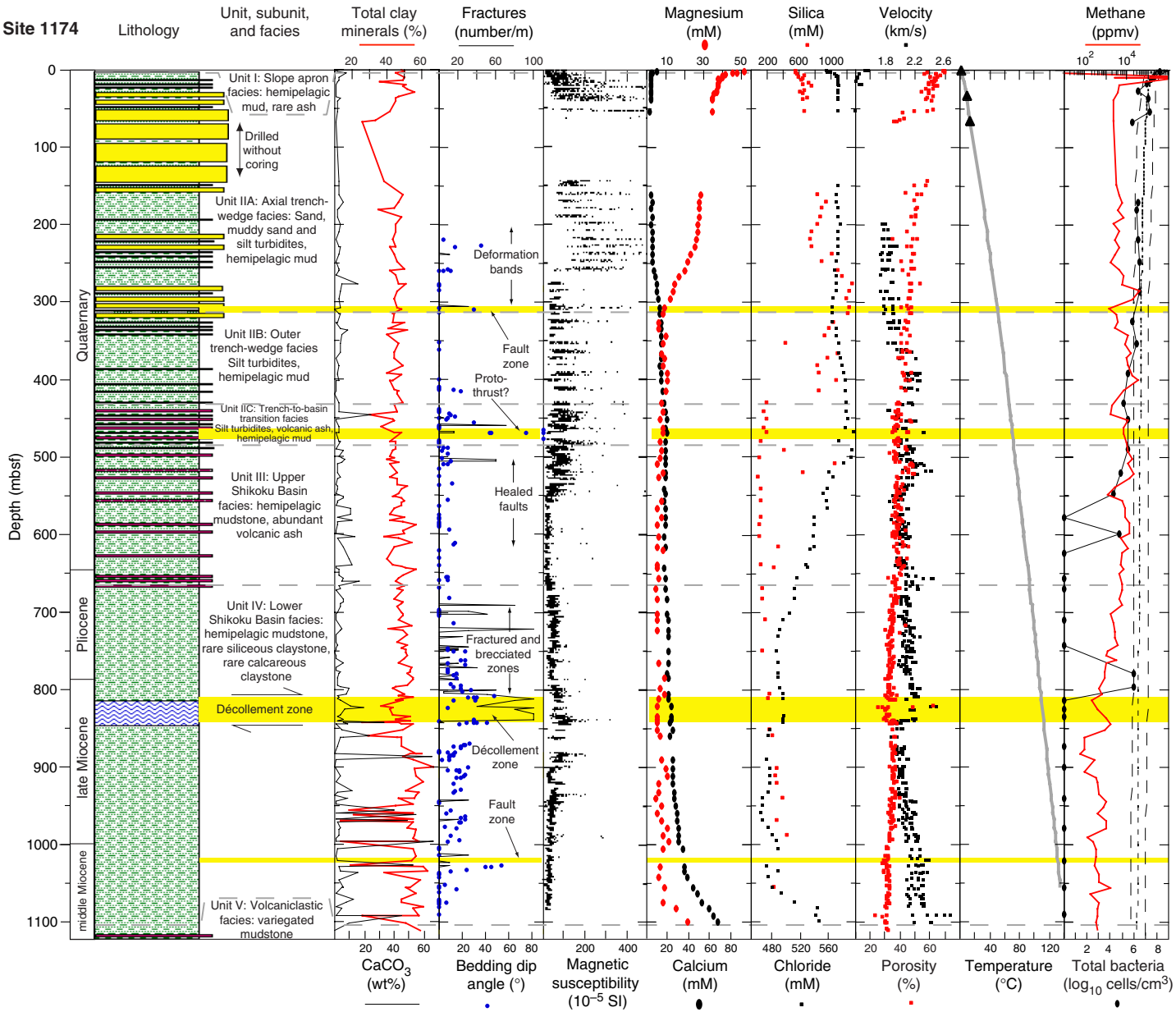

Figure F16. Graded interval of medium- to fine-grained sand with some mudchips in the upper part of Subunit IIA (Sample 190-1174A-8H-5, 0–80 cm.)

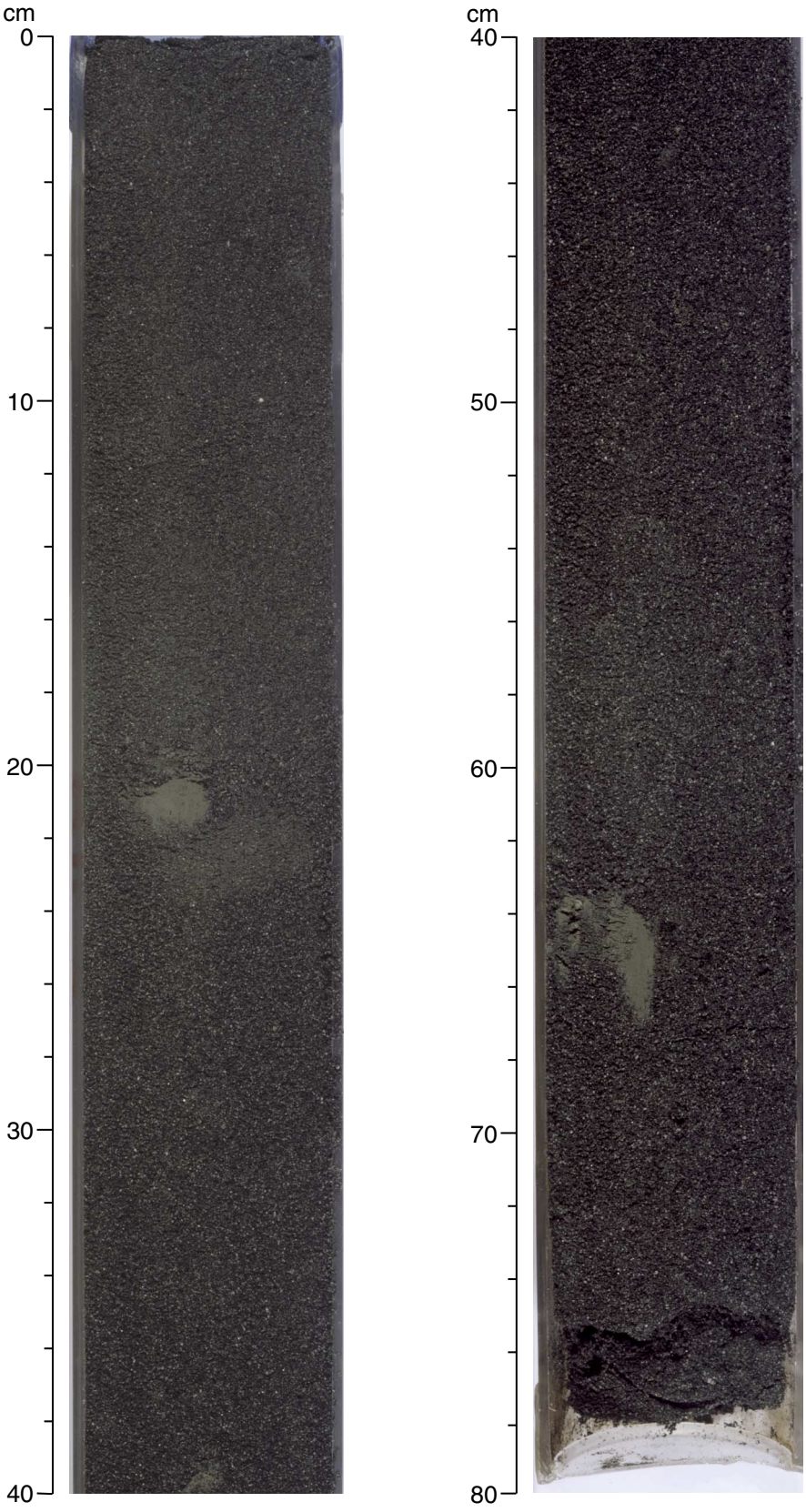

Figure F17. Deformation bands. **A.** Note the varying width and the tendency of the bands to bifurcate (interval 190-1174B-17R-2, 103–112 cm). **B.** Note the variation in the width of the more shallowly inclined set (interval 190-1174B-15R-2, 19–24 cm).

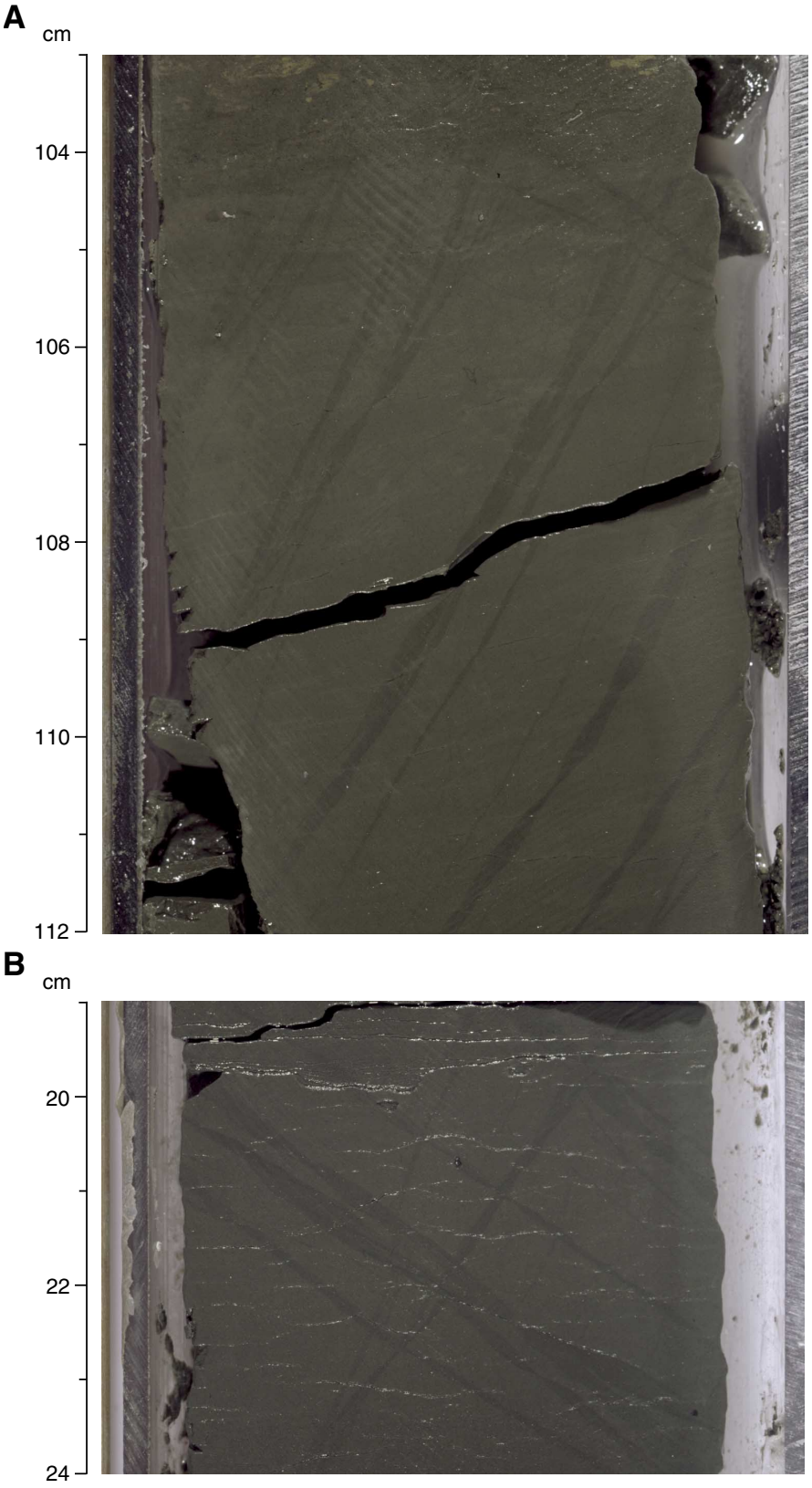

Figure F18. Stereographic equal-area lower hemisphere projections of deformation bands, illustrating the effectiveness of paleomagnetic reorientation. **A.** Deformation bands in the core liner reference frame, before paleomagnetic reorientation. **B.** Data in A after paleomagnetic correction to real geographic coordinates (excluding some planes for which the paleomagnetic information was not available). Note the concentration into two oppositely dipping sets. **C.** Poles to the planes shown in B. **D.** Average of the two sets of deformation bands showing the dihedral angle and the inclination of the acute bisectrix from vertical.

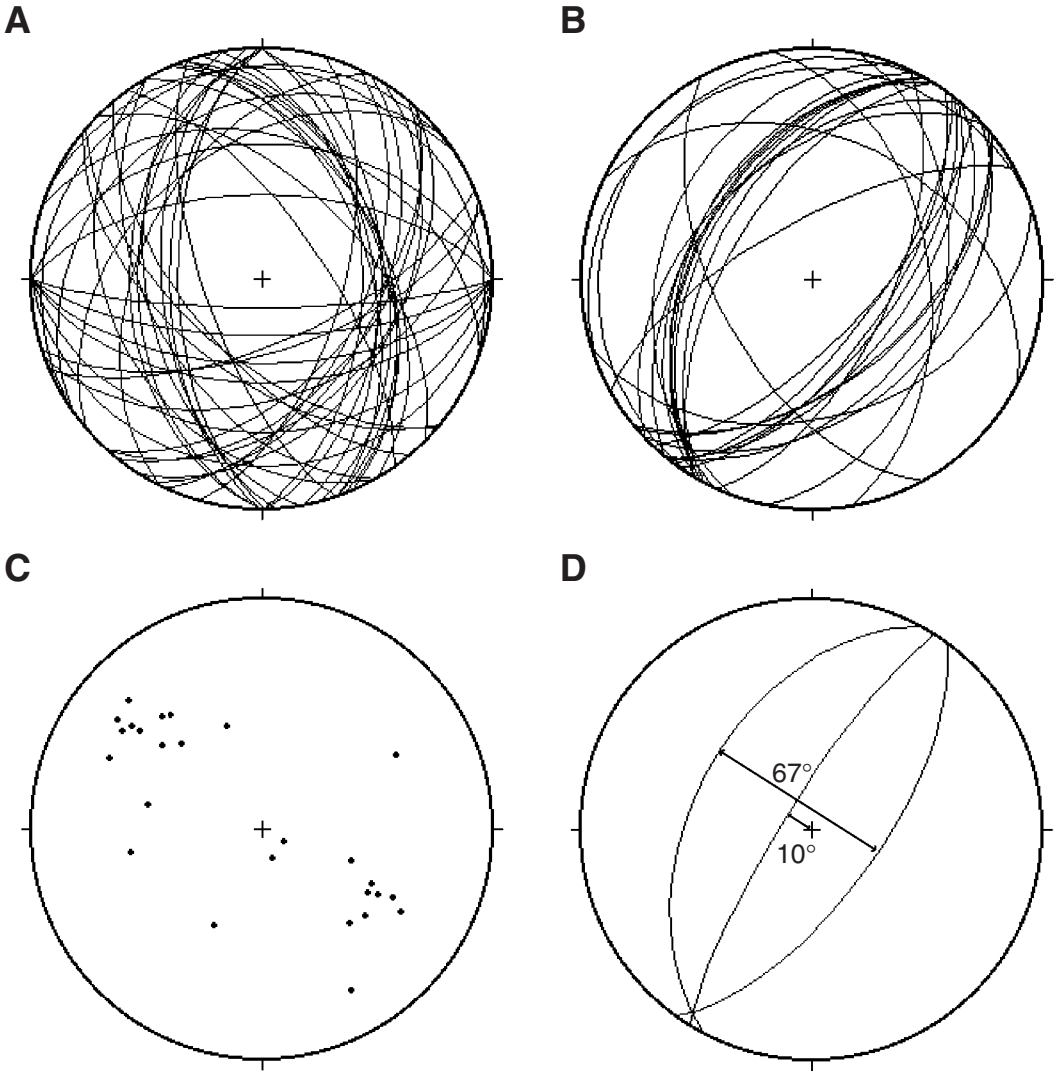

Figure F19. A. Upper part of décollement zone, showing breakage into angular blocks along inclined fractures (interval 190-1174B-71R-2, 48–79 cm). **B.** The lower part of décollement zone, showing comminution of sediments (interval 190-1174B-73R-1, 96–118 cm) (see **"Site 1174 Core Descriptions,"** p. 80, for a photograph of Core 190-1174B-73R).

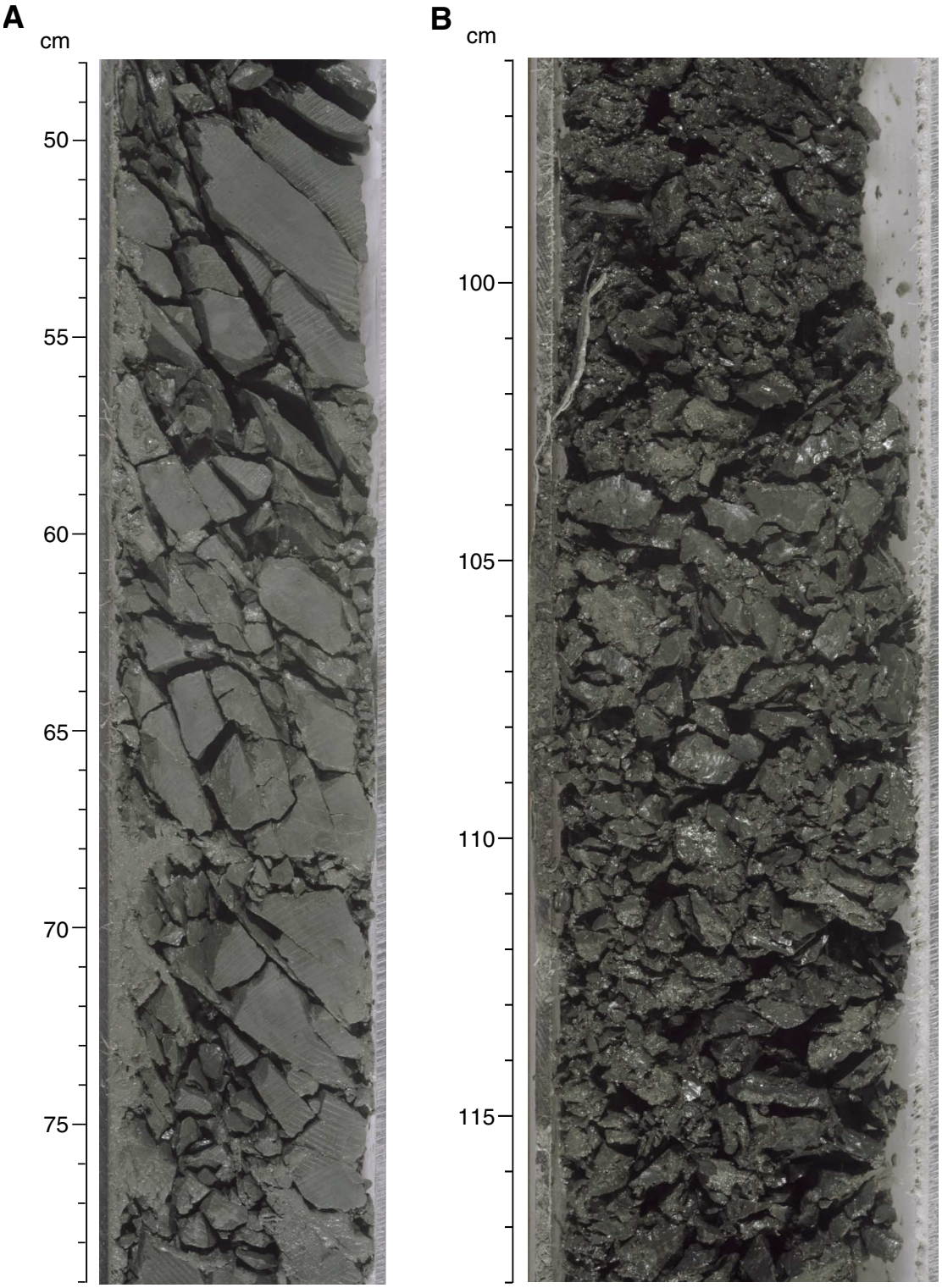

Figure F20. Details of fracturing across the décollement zone. The density of fracturing is expressed by the nature and size of the brecciated fragments. Most of the fracture surfaces are slickensided and slickenlined. Note the trend of increasing fracturing downward through the zone, peaking a few meters above a sharply defined base.

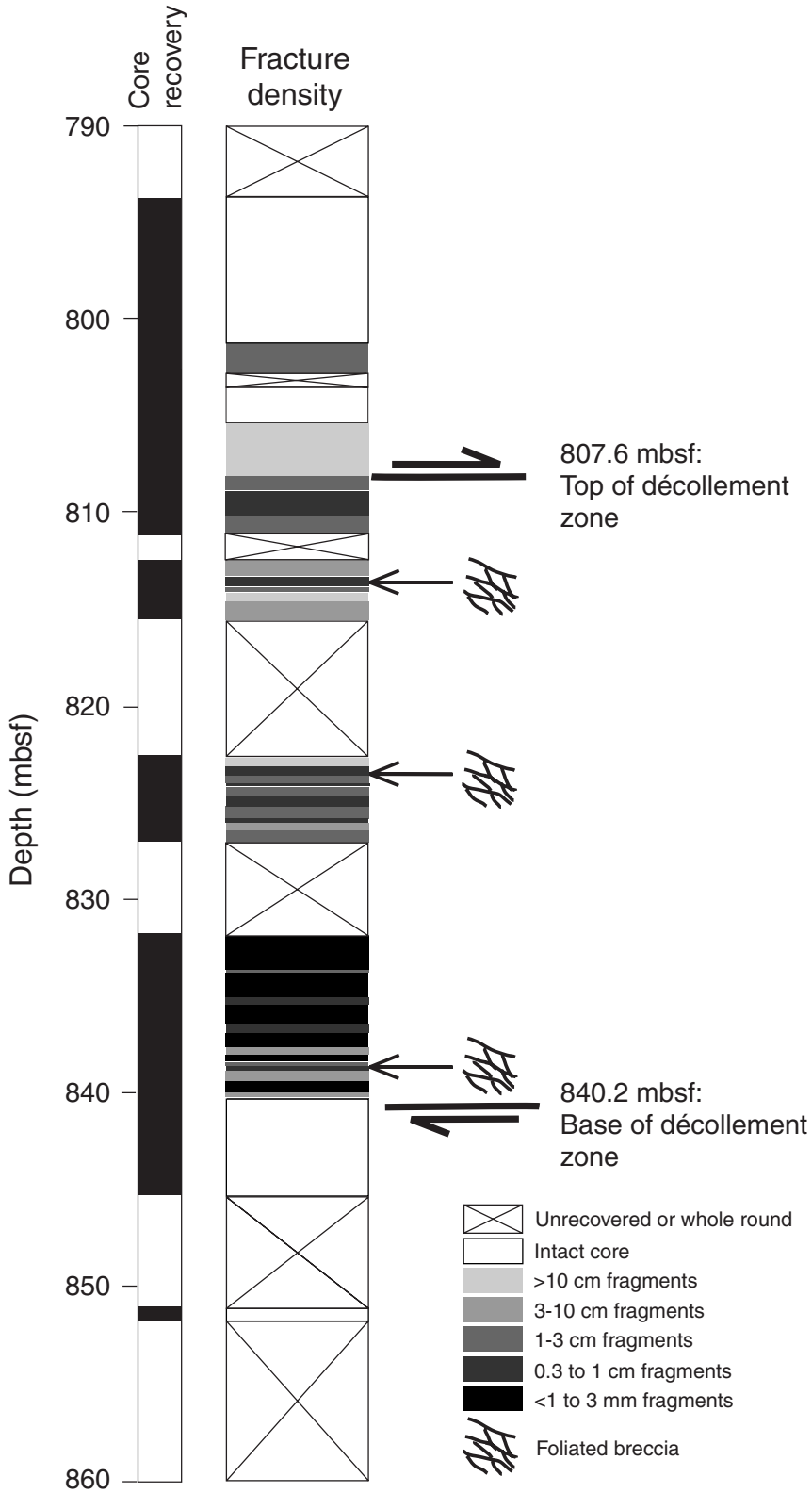

Figure F21. Summary of results at Site 1175.

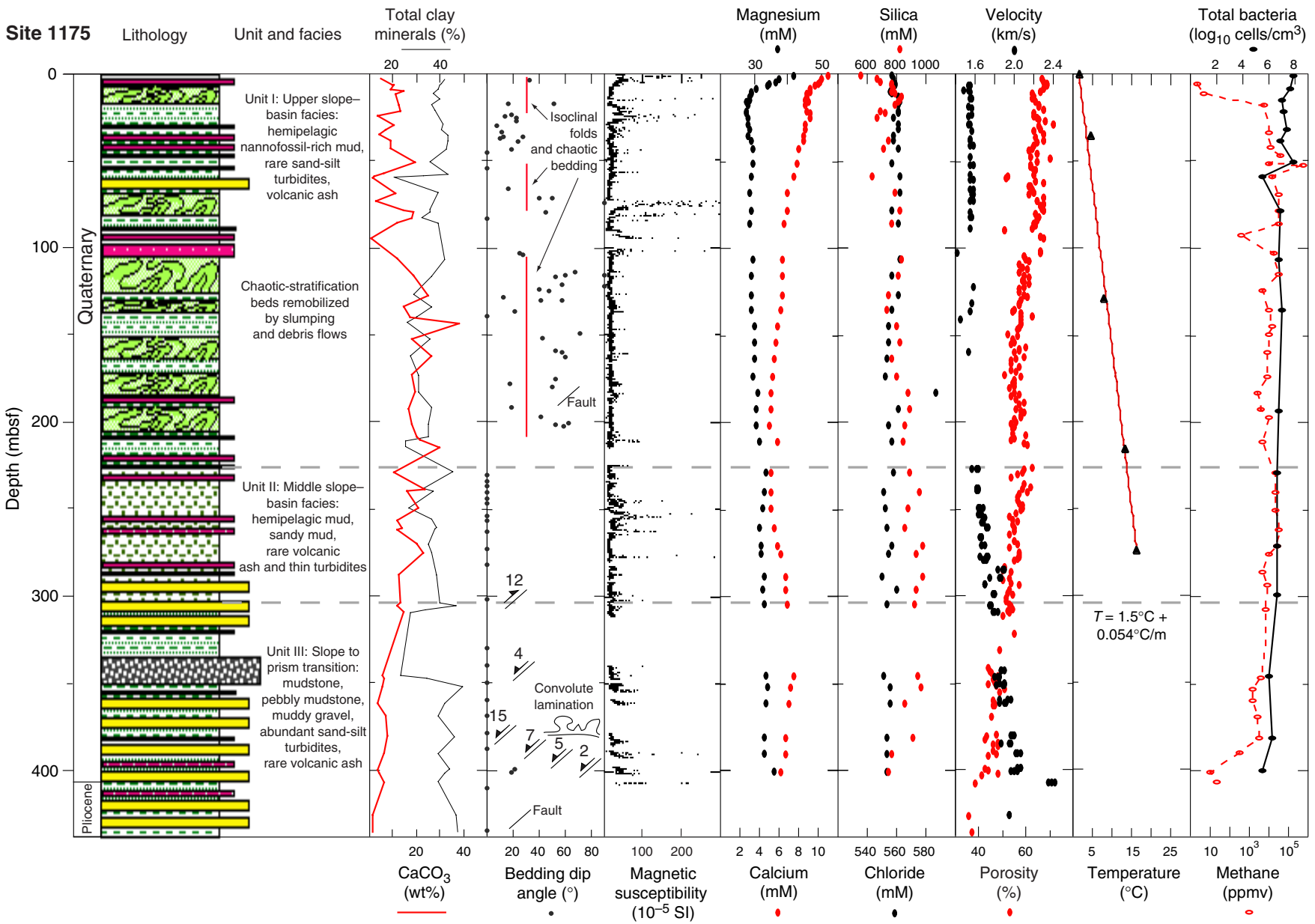

Figure F22. Chaotic bedding of Unit I (interval 190-1175A-9H-1, 65–110 cm).

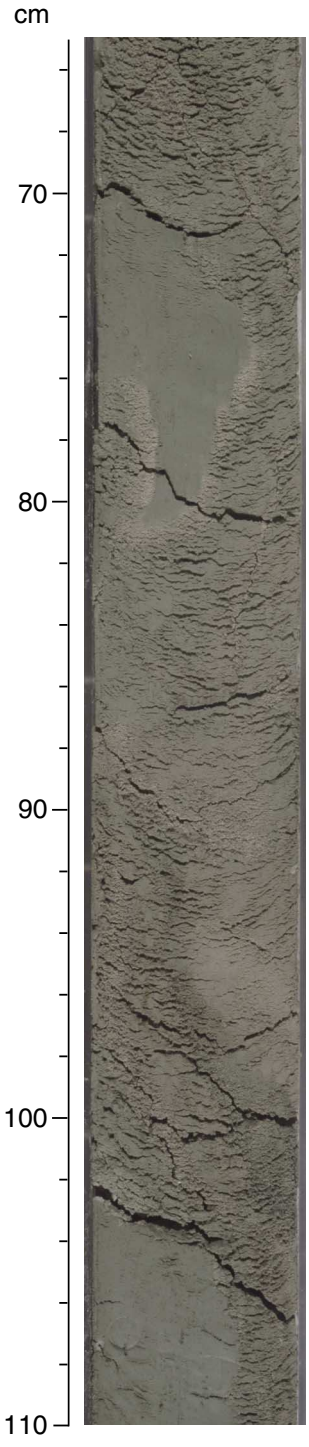

Figure F23. Pebbly mudstone of Unit III (interval 190-1175A-37X-4, 70–110 cm).

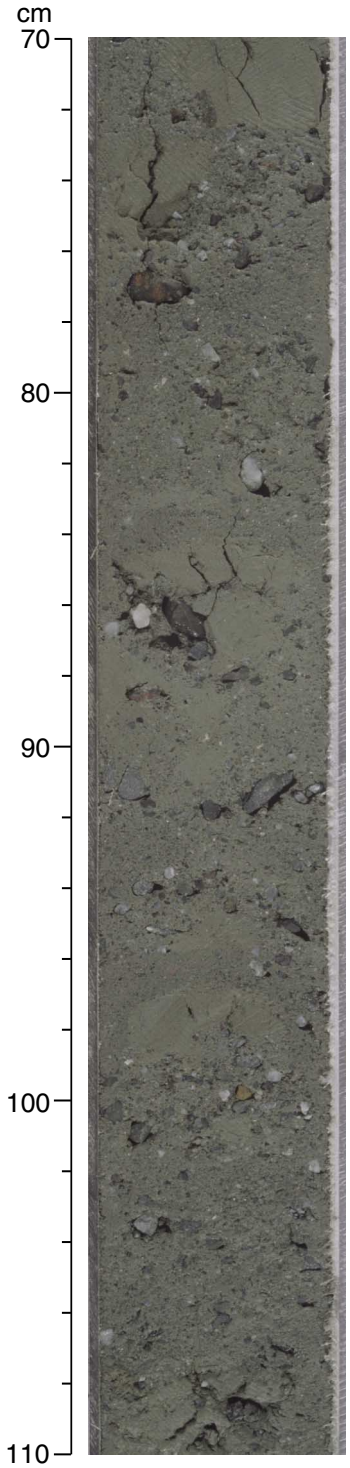

Figure F24. Summary of results at Site 1176.

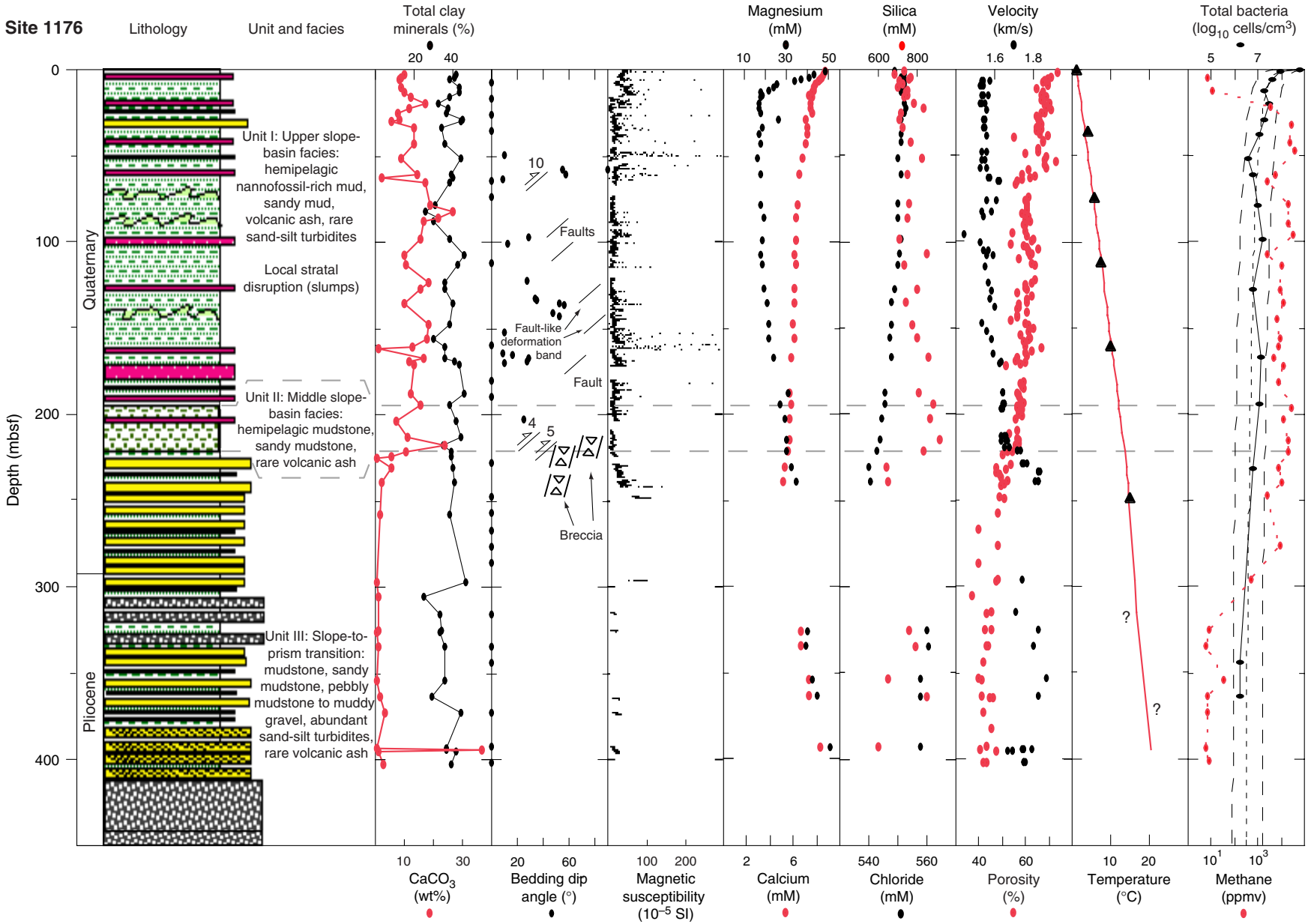

Figure F25. Pebbles and gravel of quartz and lithic clasts in muddy matrix from Unit III (interval 190-1176A-47X-CC, 0–28 cm).

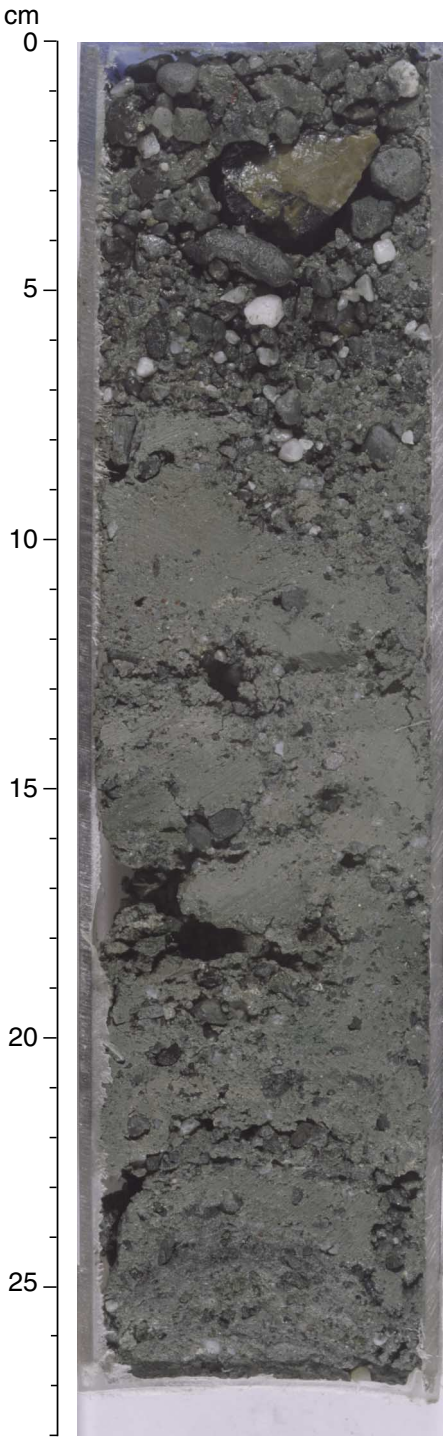

Figure F26. Summary of results at Site 1177.

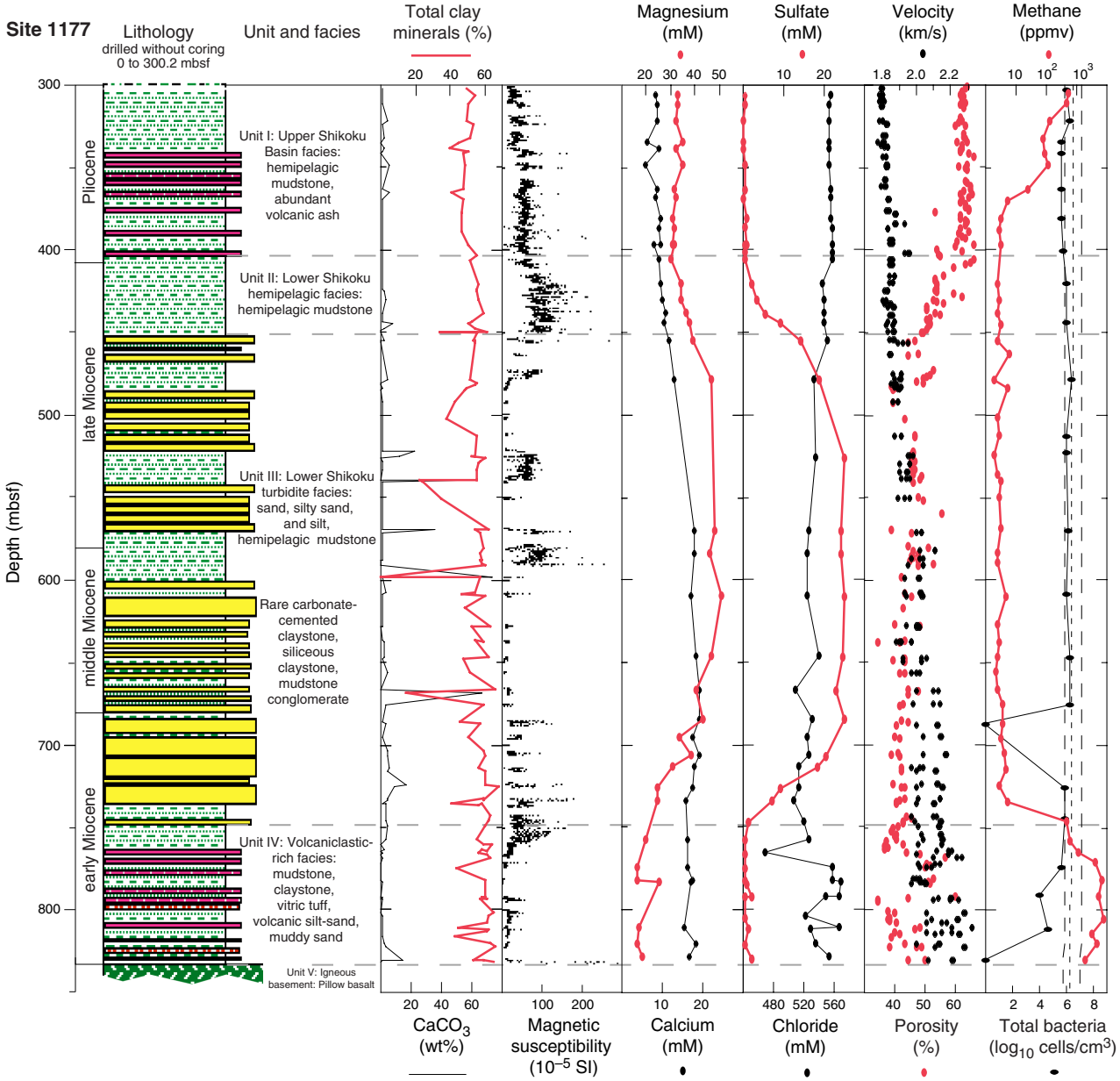

Figure F27. Wood-rich sandy turbidite interbedded with silty claystone from Unit III (interval 190-1177A-43R-3, 0–25 cm).

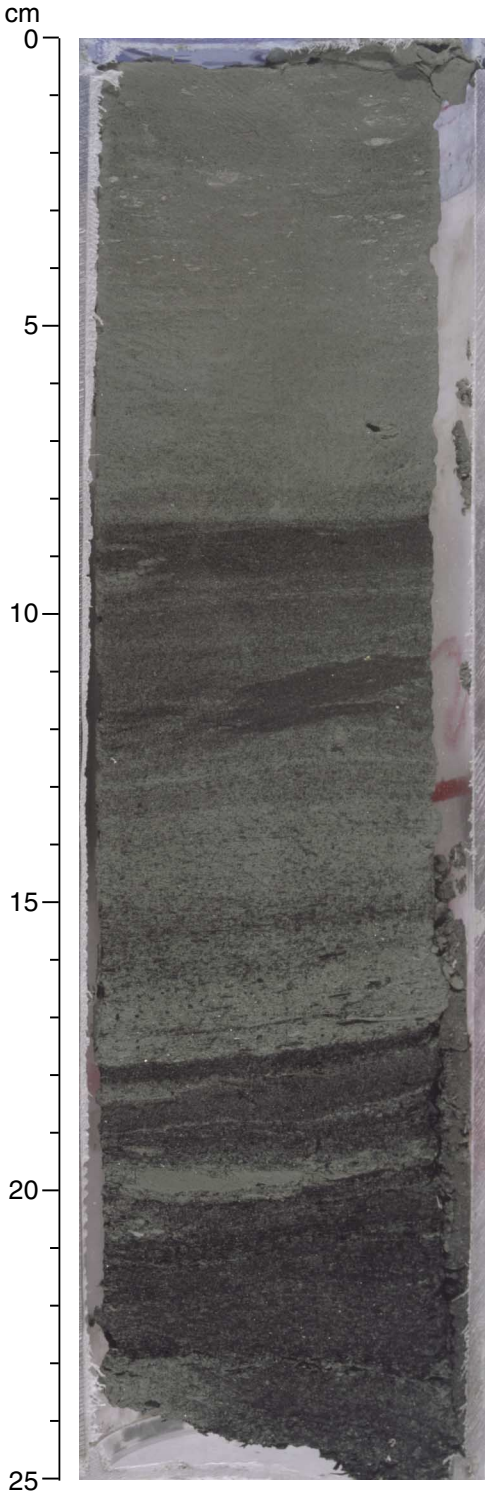

Figure F28. Laminated and bioturbated volcanic ash of Unit IV (interval 190-1177A-49R-4, 77–101 cm).

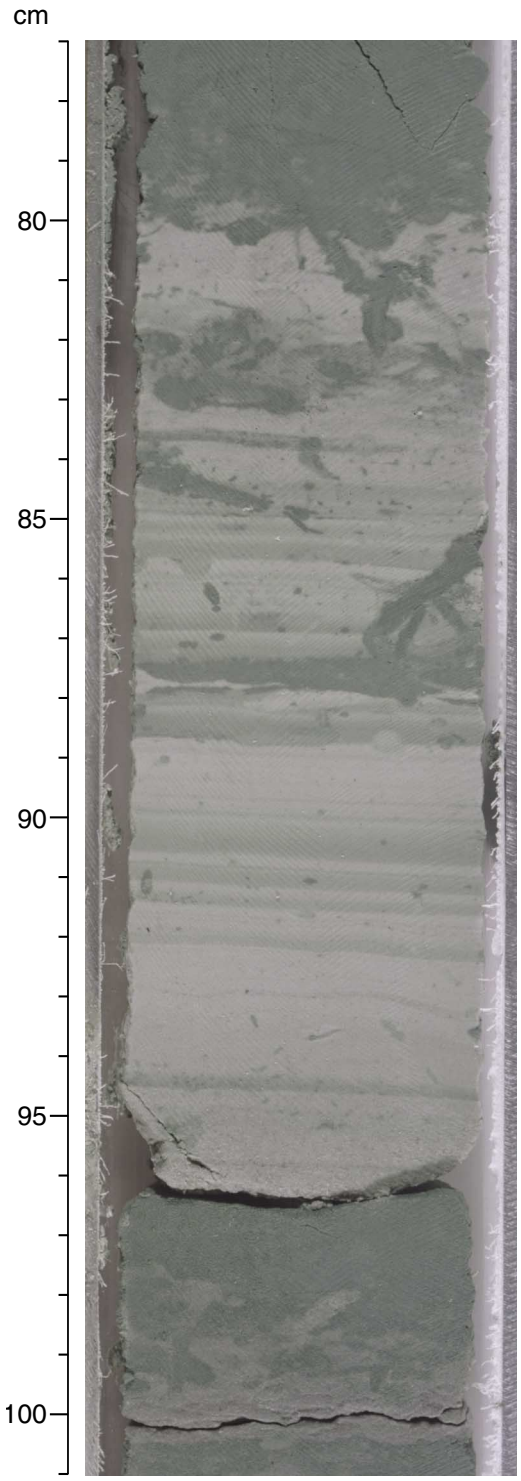

Figure F29. Contact between green basal mudstone (Unit IV) and basalt (Unit V) (interval 190-1177A-56R-3, 0–12 cm).

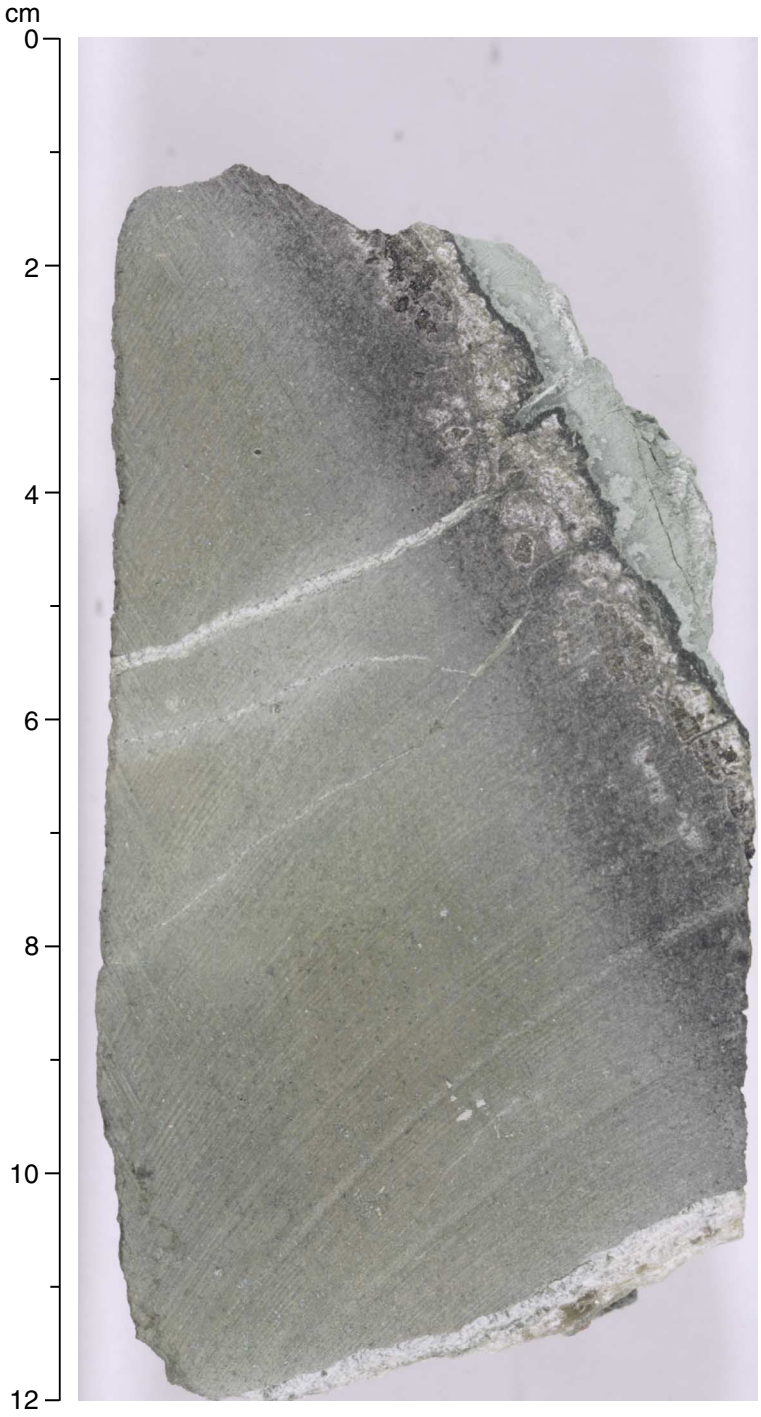

Figure F30. Summary of results at Site 1178.

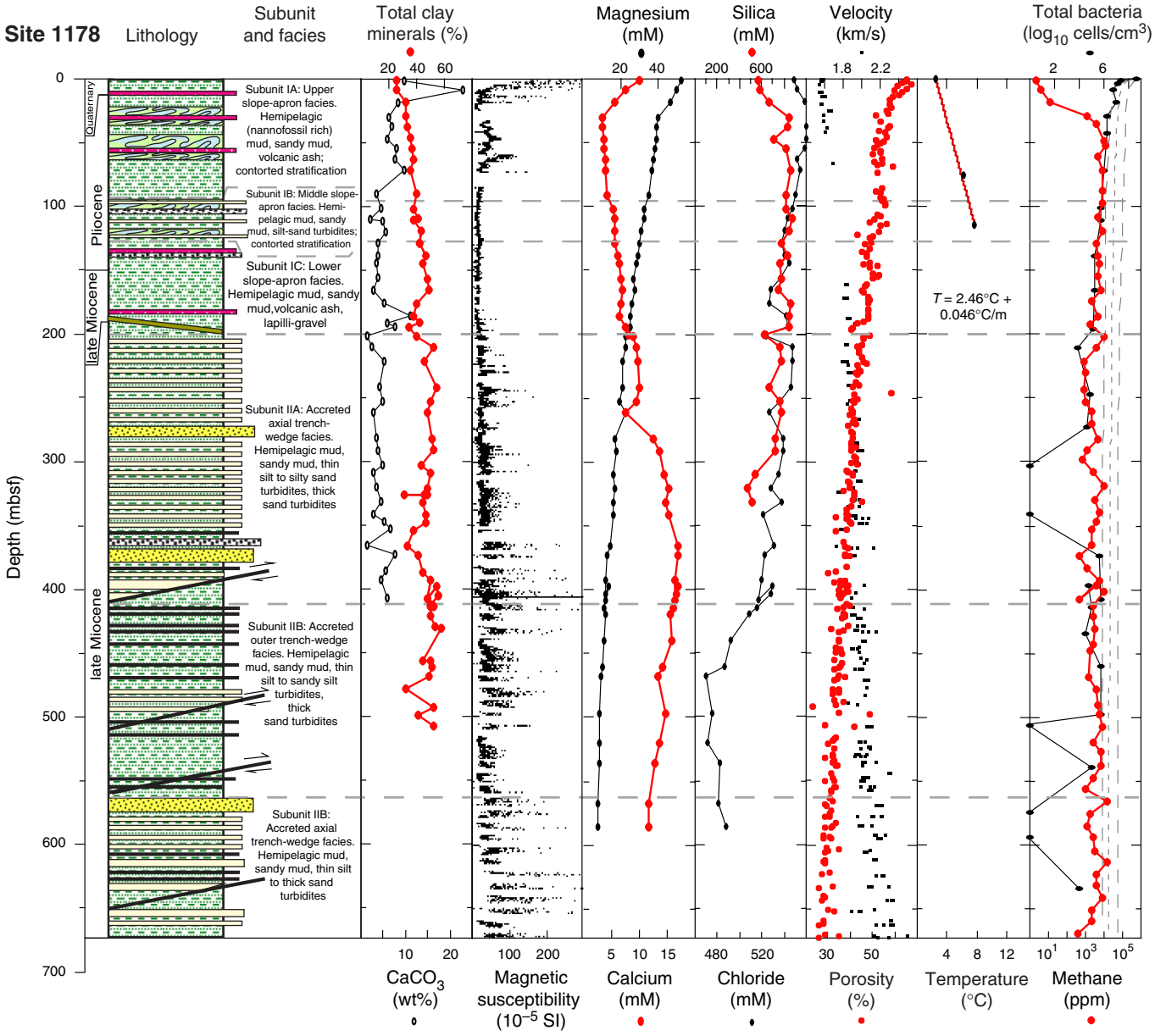

Figure F31. Bedding-oblique foliation typical of Domain III (interval 190-1178B-9R-5, 5–27 cm). Steeply dipping bedding was observed over the intervals 5–10 and 22–27 cm, bounding an interval with lower angle foliation.

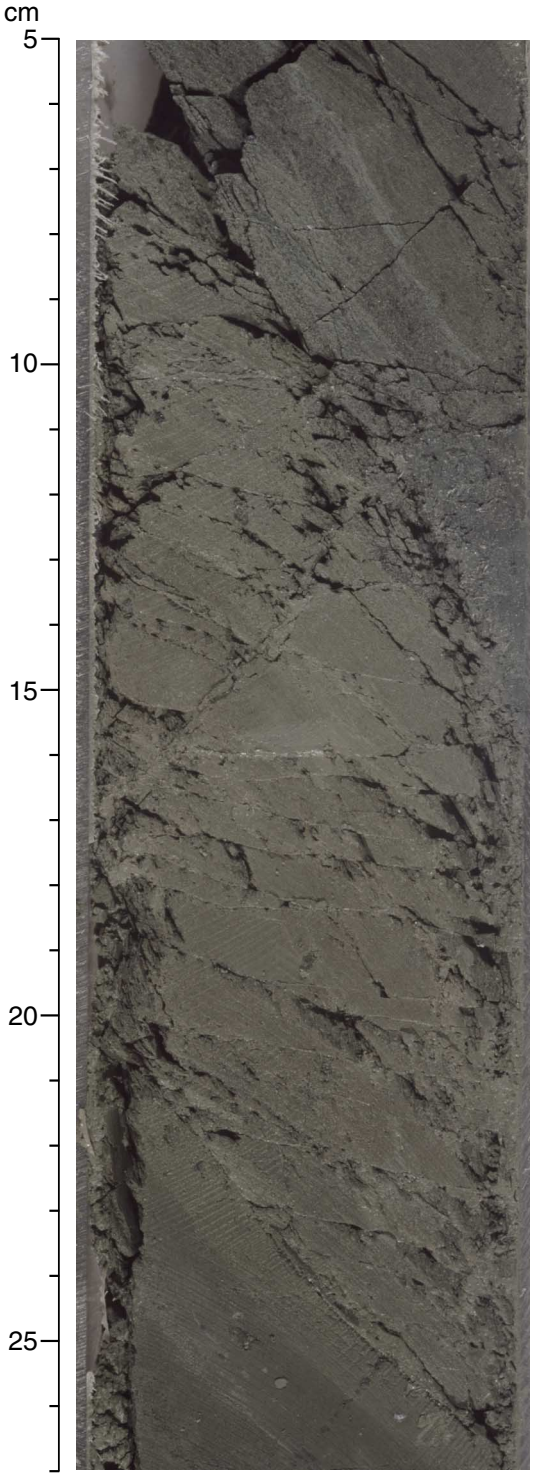

Figure F32. Incipient weblike structure in fine sand (interval 190-1178B-29R-3, 35–53 cm).

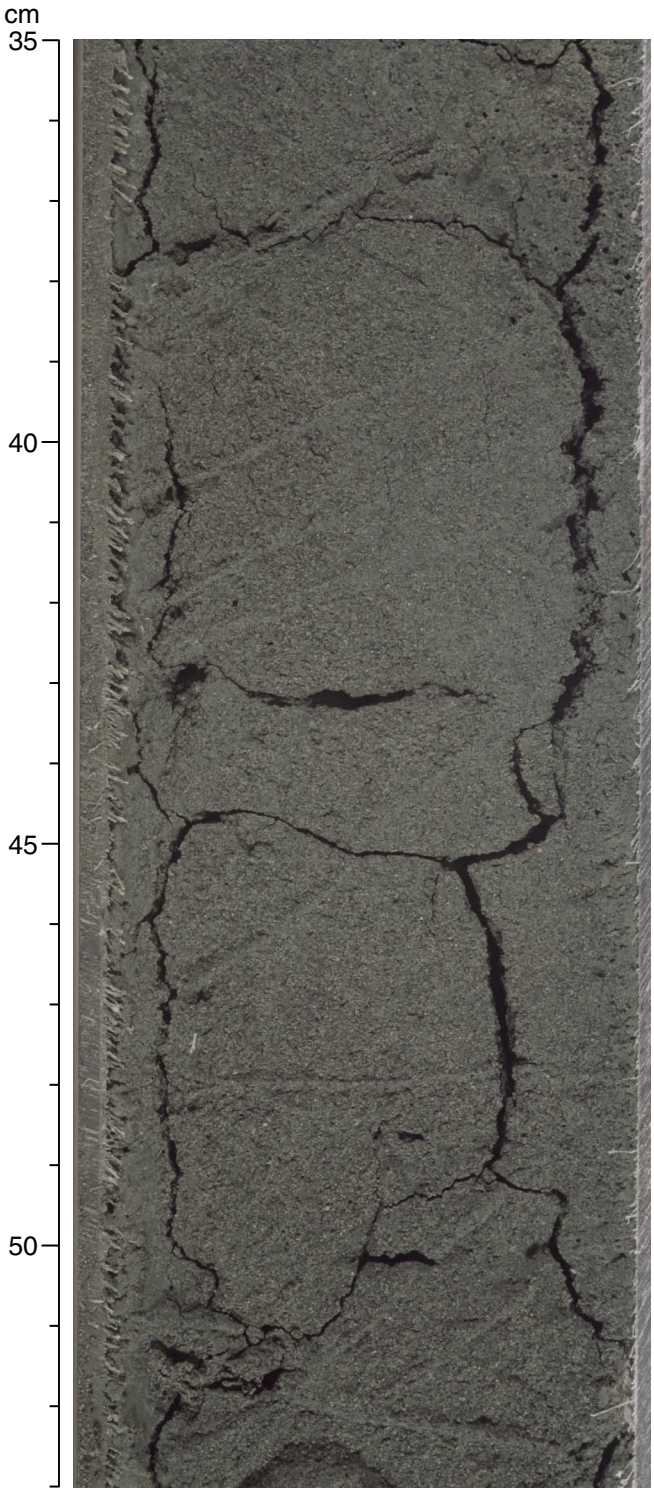

Figure F33. Incipient scaly and foliated clays with fine black seams crosscutting the fracture fabric (interval 190-1178B-27R-3, 27–41 cm).

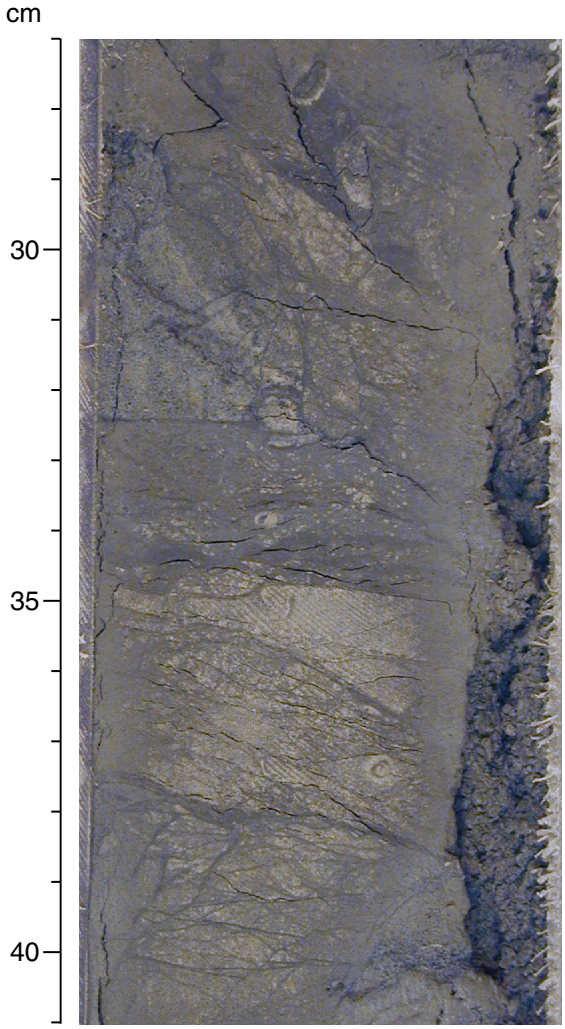

Figure F34. Biostratigraphic and magnetostratigraphic correlation between Leg 190 reference and prism toe sites of the Ashizuri and Muroto Transects.

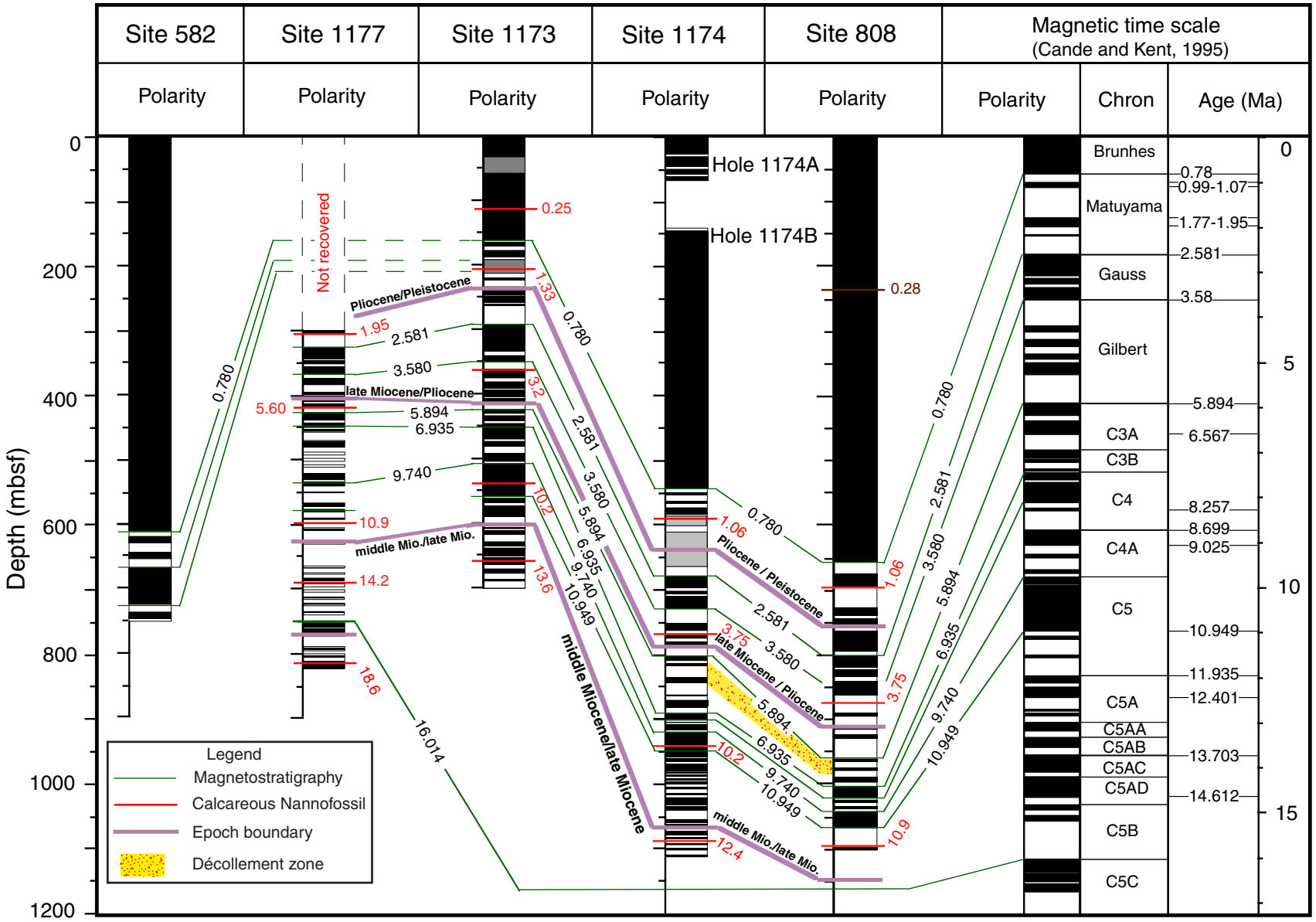

Figure F35. Age-depth plots based on biostratigraphic (solid squares) and paleomagnetic (open squares) data for prism toe sites of the Ashizuri and Muroto Transects.

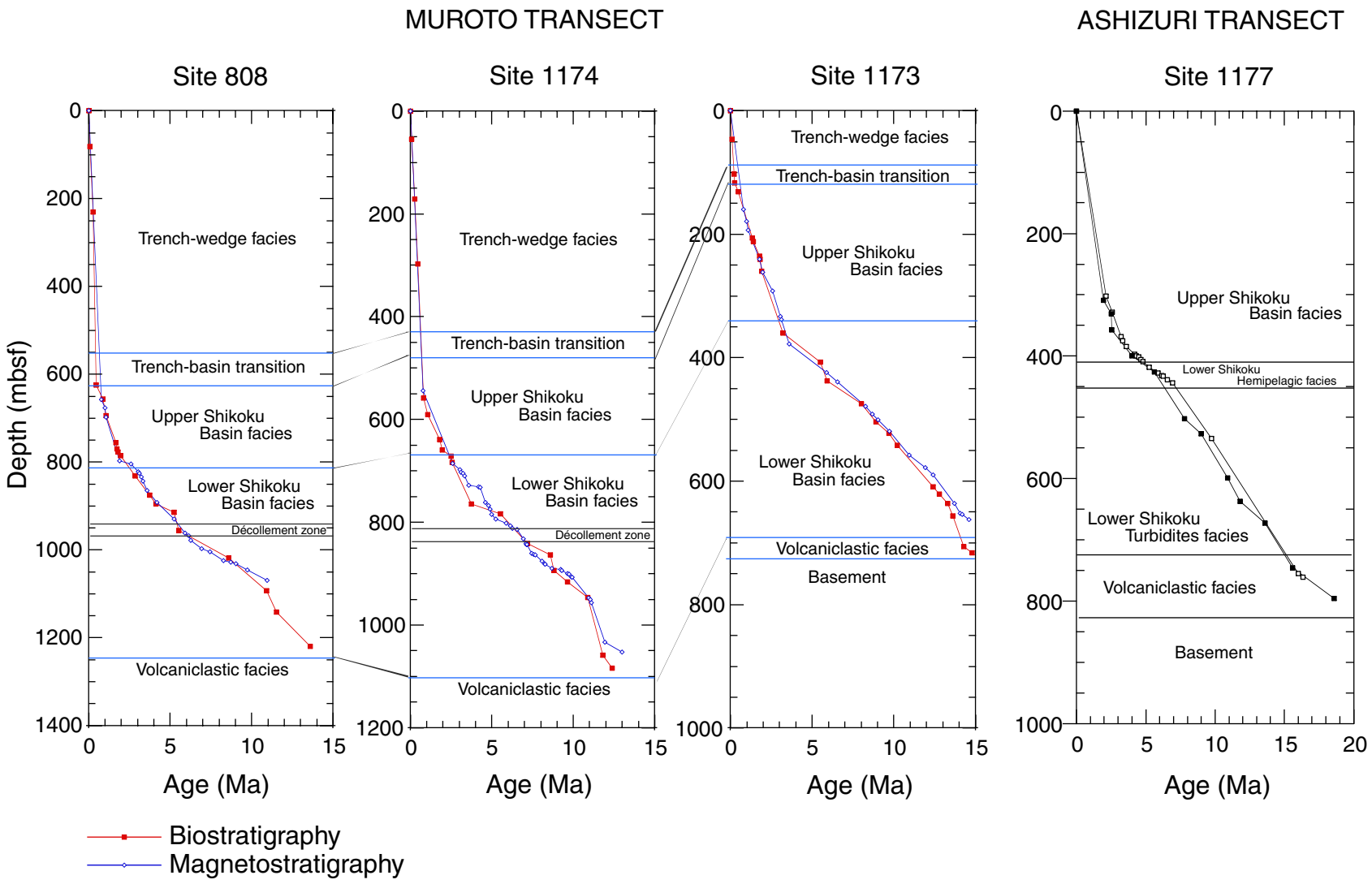

Figure F36. Comparison of the structurally identified décollement interval and its physical properties and pore-water geochemistry across the Leg 131/190 transect. The décollement interval at Site 1174 has been projected to the reference Site 1173 based on correlation of patterns in magnetic susceptibility data (see Fig. F8A, p. 49.).

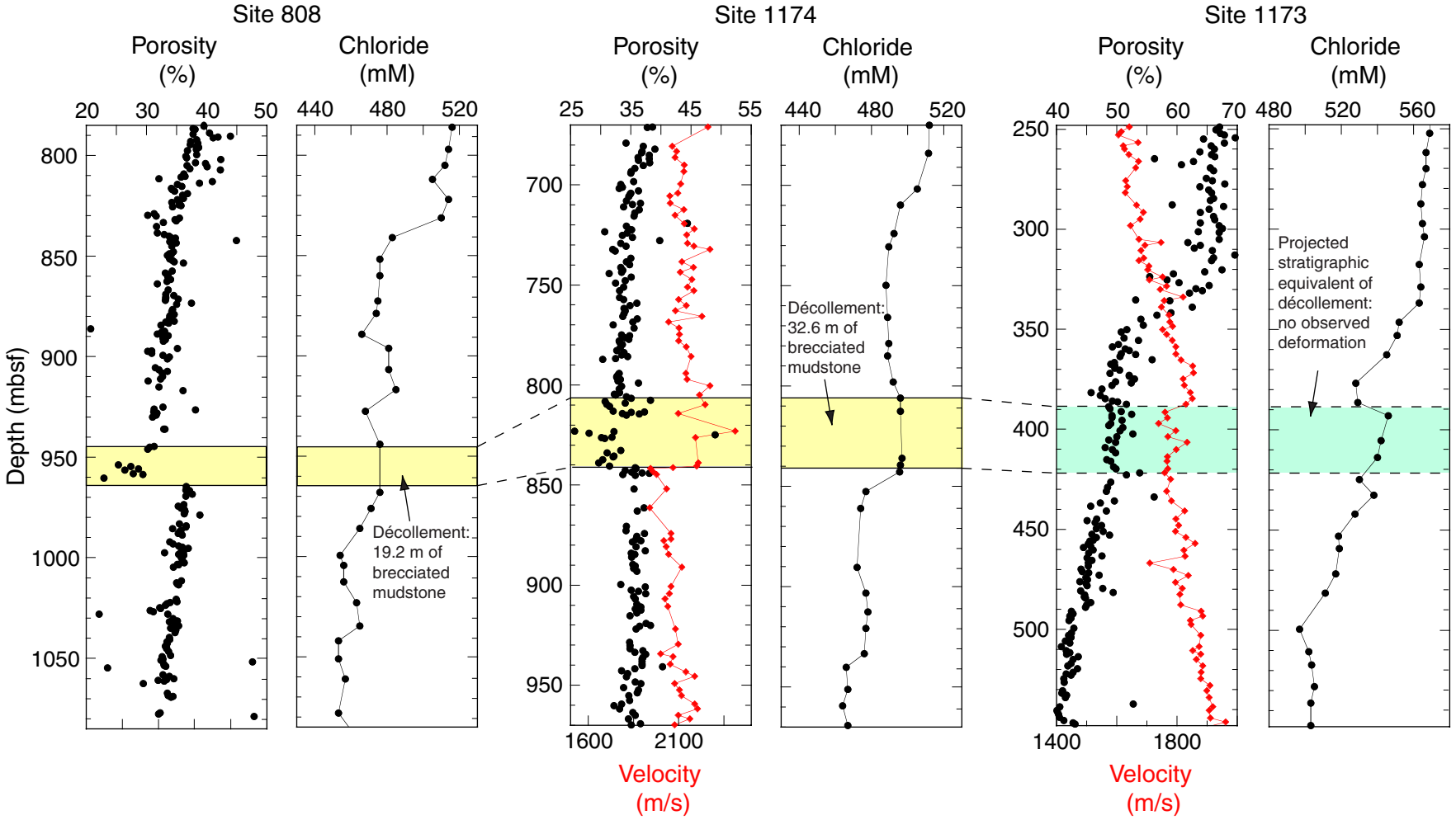

Figure F37. Structural and stratigraphic interpretation of seismic profile across the Ashizuri Transect based on drilling sites. BSR = bottom-simulating reflector.

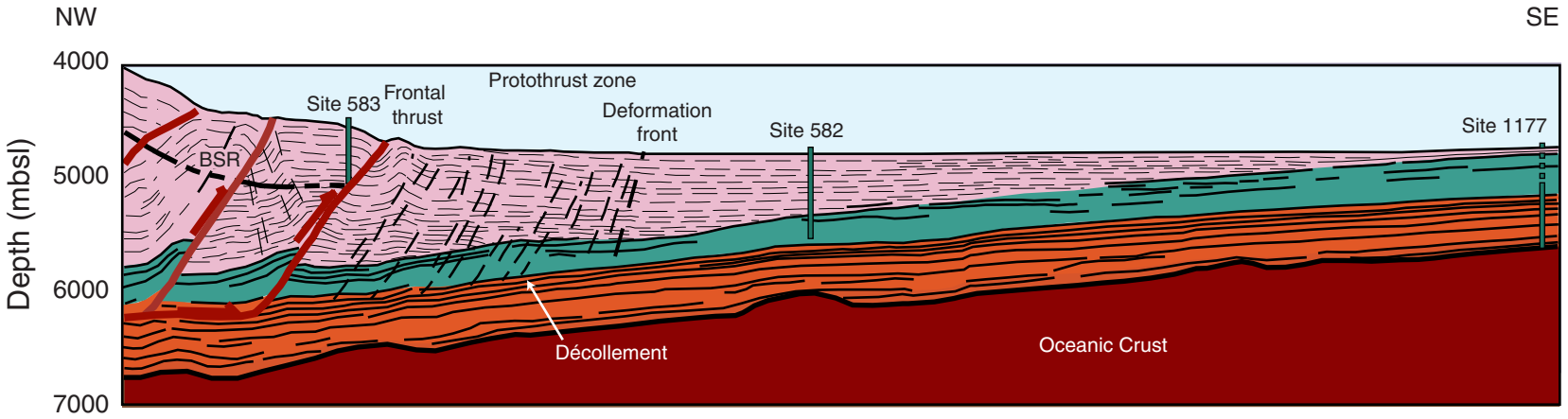

Figure F38. Chloride concentrations in interstitial water samples from the Muroto Transect reference (Site 1173) and prism toe sites (Sites 1174 and 808).

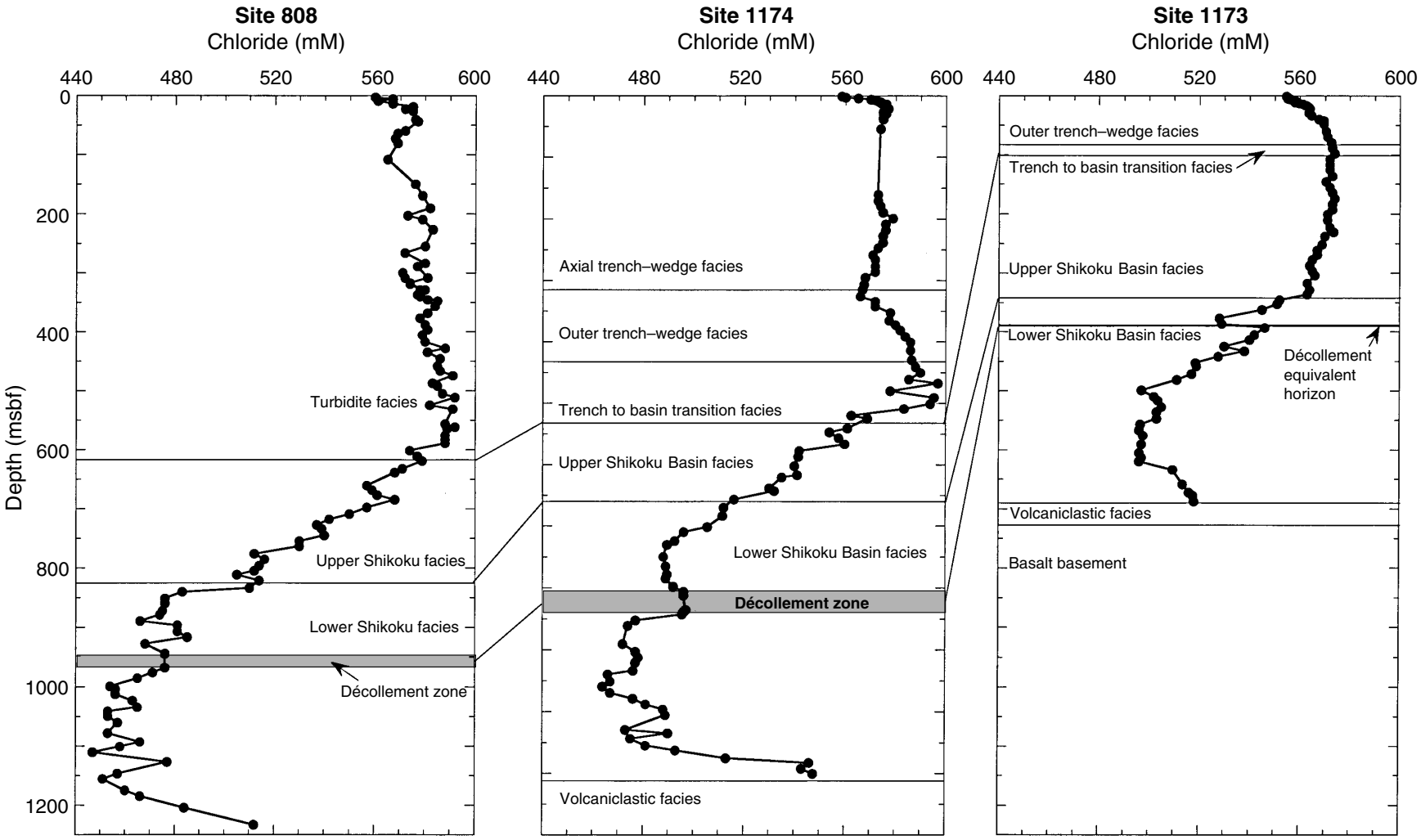

Figure F39. Porosities and velocities across the Muroto Transect (Sites 1173, 1174, and 808) and Ashizuri reference site (Site 1177). Lithologic units and major structural features are shown. The décollement location is shown by gray shading where it was observed and by a dashed line at the stratigraphically equivalent depth at the reference sites. (**Figure shown on next page.**)

Figure F39 (continued). (Caption shown on previous page.)

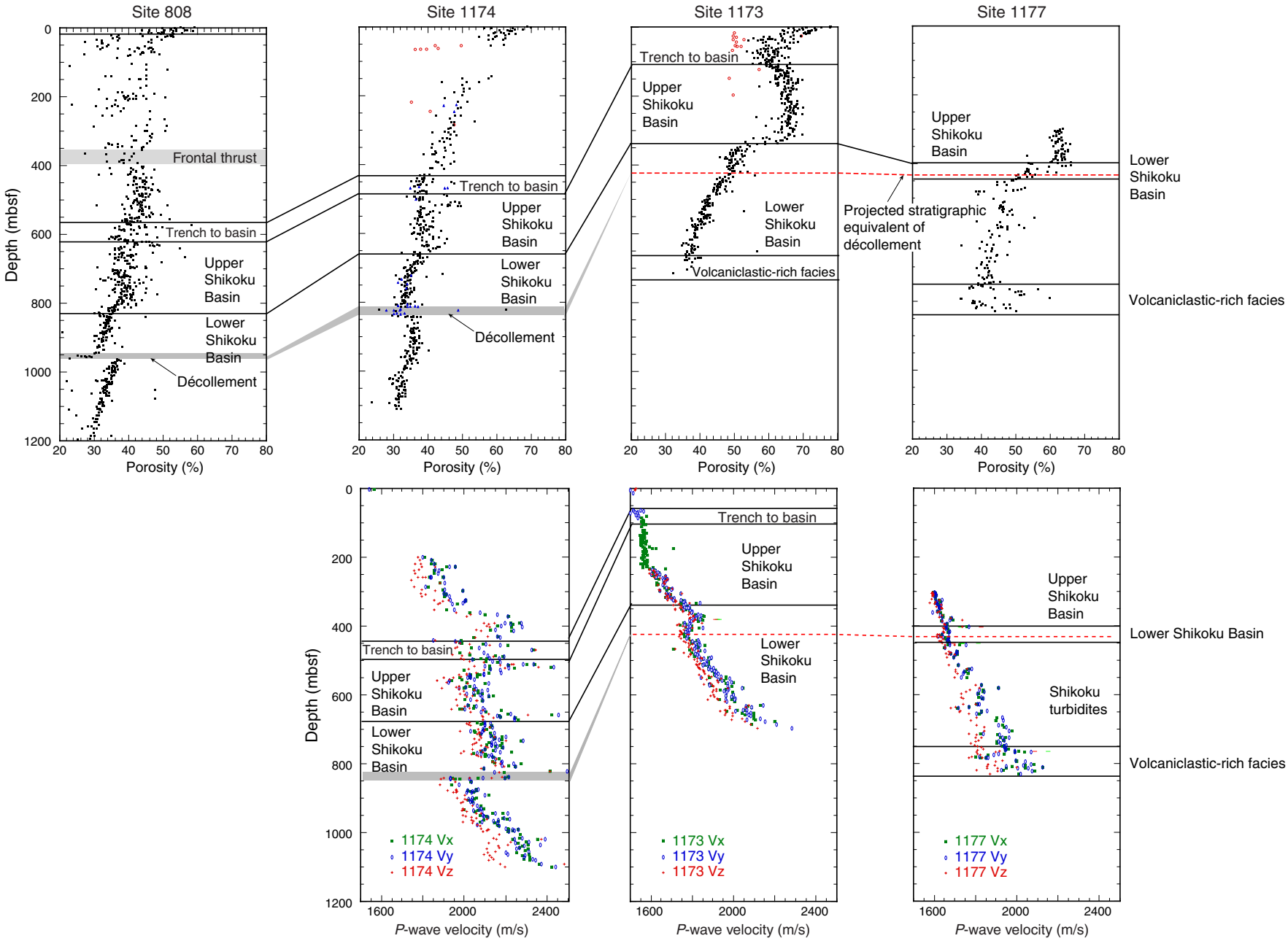

Figure F40. Biostratigraphic and paleomagnetic ages as a function of solid thickness (thickness of the sediment after vertical compaction to 0% porosity) for Sites 808, 1174, 1173, and 1177. Lithostratigraphic units and their correlation between holes are indicated in blue (solid and dashed). The décollement interval is indicated at Sites 808 and 1174 (green/shaded). The red lines (patterned) mark the 4- to 7-Ma age interval. This interval appears thicker at the décollement Sites 808 and 1174 than at the reference Sites 1173 and 1177.

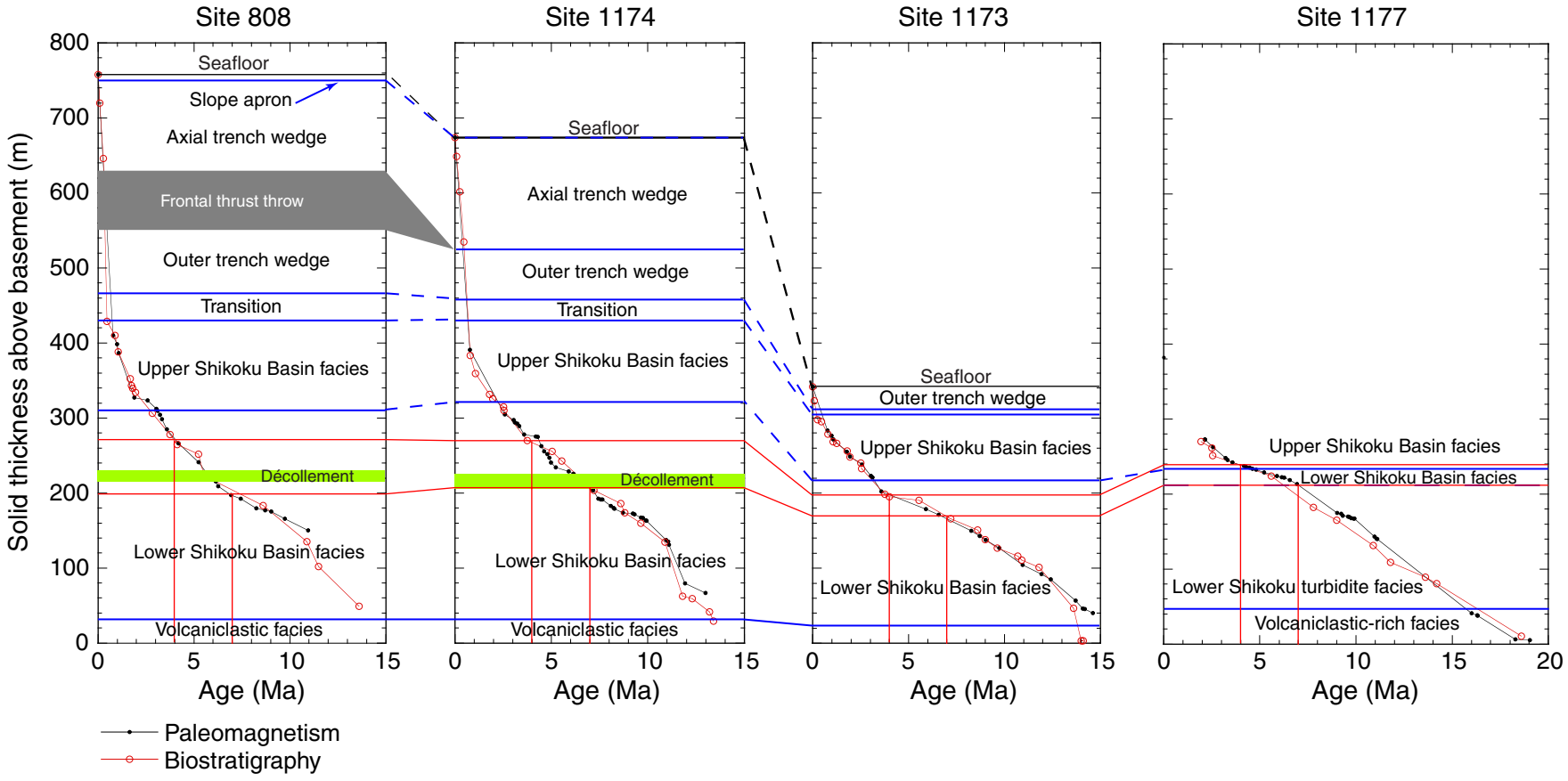

Figure F41. Interpretation of hydrocarbon sources encountered during Leg 190. Note that depth scale is different for each plot. Vertical lines represent zones for thermogenic, mixed, and bacterial regions for the hydrocarbon profiles.

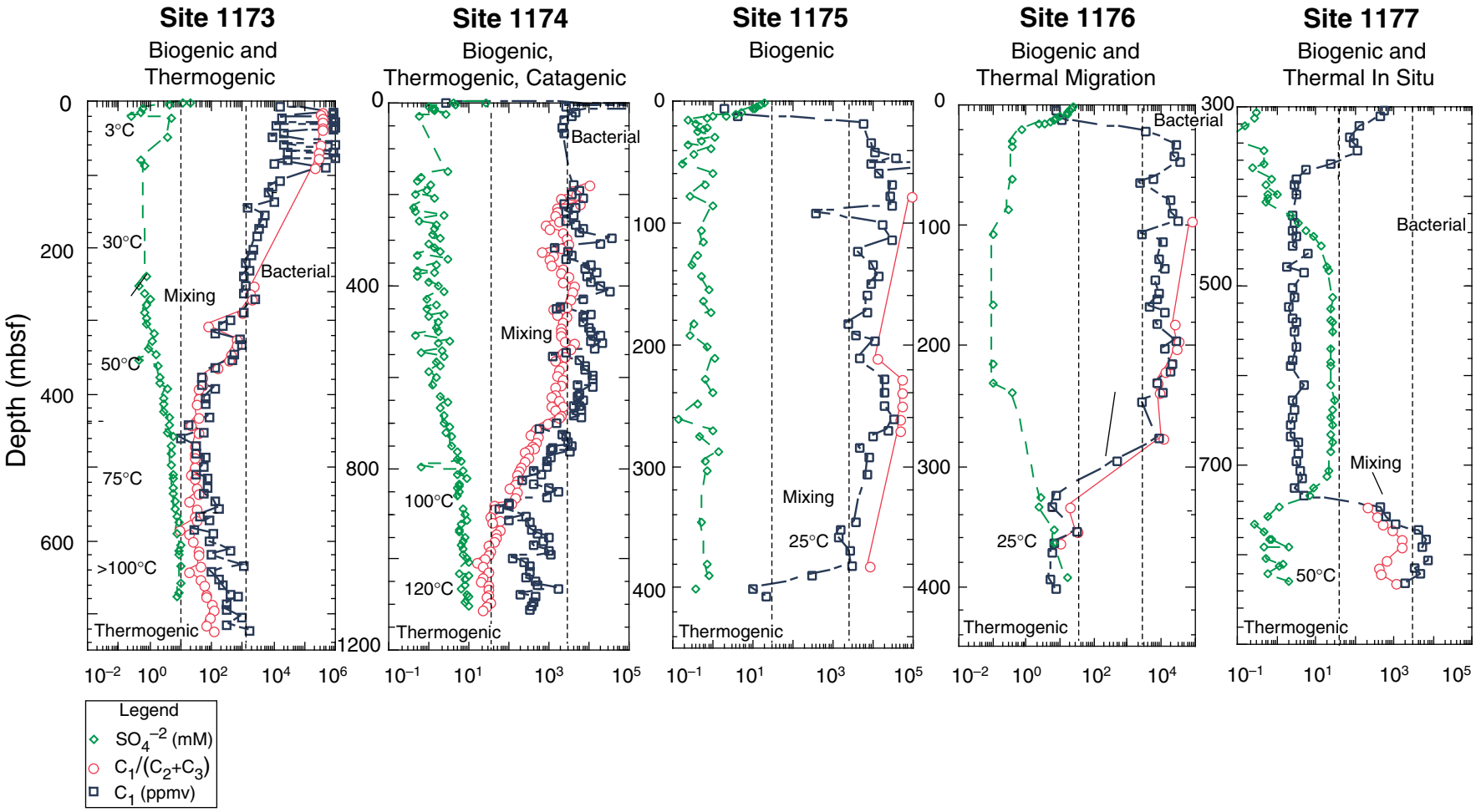

Figure F42. Biogeochemical profiles in sediments from Nankai Trough sites (Leg 190). **A.** Total bacterial populations at Sites 1173, 1174, and 1177. The dashed curve represents a general regression line of bacterial numbers vs. depth in deep-sea sediments (Parkes et al., 1994), with 95% upper and lower prediction limits shown by large dashed curves. **B–D.** Sulfate, methane, and total organic carbon depth profiles for Sites 1173, 1174, and 1177, respectively. **E.** C_1/C_2 ratios for Sites 1173, 1174, and 1177.

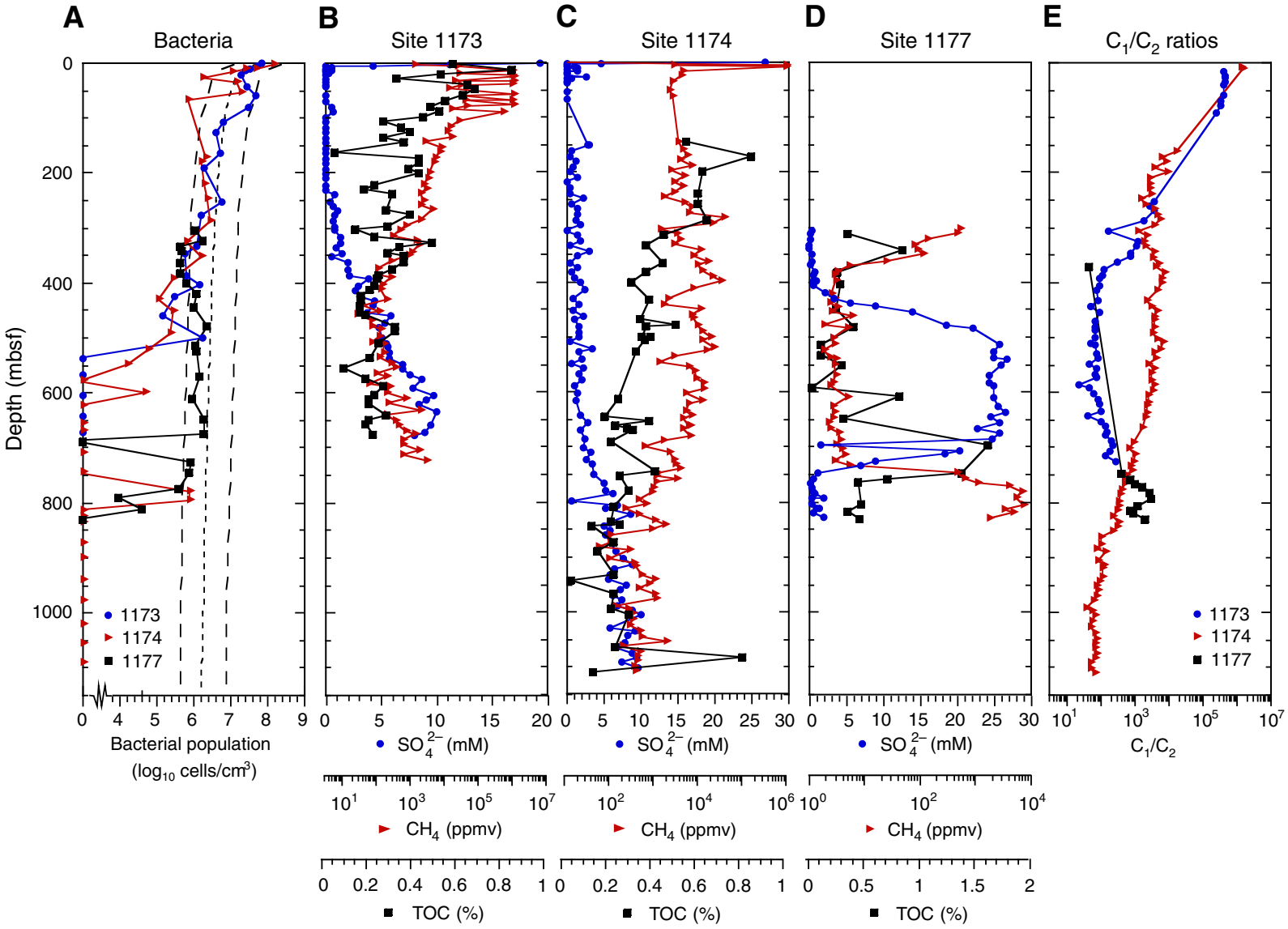

Table T1. Leg 190 operational summary.

Hole	Latitude	Longitude	Water depth (m)	Number of cores	Interval Cored (m)	Core Recovered (m)	Recovery (%)	Drilled (m)	Maximum penetration (m)	Time on hole (hr)	Time on hole (days)
1173A	32°14.6634′N	135°01.5085′E	4790.7	77	734.3	658.10	89.6	0.0	734.3	232.72	9.70
Site 1173 totals:				77	734.3	658.10	89.6	0.0	734.3	232.72	9.70
1174A	32°20.5377′N	134°57.3876′E	4751.2	9	74.1	47.04	63.5	0.0	74.1	42.50	1.77
1174B	32°20.5404′N	134°57.3866′E	4751.2	102	976.1	577.57	59.2	143.7	1119.8	333.00	13.88
Site 1174 totals:				111	1050.2	624.61	59.5	143.7	1193.9	375.50	15.65
1175A	32°35.8855′N	134°38.6745′E	2997.6	47	439.2	327.01	74.5	5.8	445.0	79.75	3.32
Site 1175 totals:				47	439.2	327.01	74.5	5.8	445.0	79.75	3.32
1176A	32°34.6976′N	134°39.9419′E	3020.5	48	443.5	226.25	51.0	6.1	449.6	76.50	3.19
Site 1176 totals:				48	443.5	226.25	51.0	6.1	449.6	76.50	3.19
1177A	31°39.1510′N	134°0.7132′E	4844.3	56	533.7	282.74	53.0	300.2	833.9	135.13	5.63
Site 1177 totals:				56	533.7	282.74	53.0	300.2	833.9	135.13	5.63
1178A	32°43.8608′N	134°28.7684′E	1741.7	44	410.8	340.19	82.8	0.0	410.8	77.75	3.24
1178B	32°43.8600′N	134°28.7809′E	1741.7	30	284.2	165.96	58.4	395.0	679.2	94.33	3.93
Site 1178 totals:				74	695.0	506.15	72.8	395.0	1090.0	172.08	7.17
Leg 190 totals:				413	3895.9	2624.9	67.4	850.8	4746.7	1071.7	44.7